REPORT DOCUMENTATION PAGE

Form Approved
OMB No. 0704-0188

AD-A237 456

DATE	3. REPORT TYPE AND DATES COVERED
	FINAL 14 Aug 87 TO 28 Nov 90

4. TITLE AND SUBTITLE

Development of Model Based Magnetic LP-LEC Growth Large Diameter GaAs

5. FUNDING NUMBERS

DARPA

6. AUTHOR(S)

Dr August F. Witt

7. PERFORMING ORGANIZATION NAME(S) AND ADDRESS(ES)

Massachusetts Inst of Tech
77 Massachusetts Avneue
Cambridge, MA 02139-4307

8. PERFORMING ORGANIZATION REPORT NUMBER

AFOSR-TR- 91 0580

9. SPONSORING/MONITORING AGENCY NAME(S) AND ADDRESS(ES)

AFOSR/NE
Bldg 410
Bolling AFB Washington DC 20332-6448
Dr. Gerald Witt

10. SPONSORING/MONITORING AGENCY REPORT NUMBER

F49620-87-C-0106

11. SUPPLEMENTARY NOTES

12a. DISTRIBUTION/AVAILABILITY STATEMENT

APPROVED FOR PUBLIC RELEASE: DISTRIBUTION IS UNLIMITED

12b. DISTRIBUTION CODE

13. ABSTRACT (Maximum 200 words)

SEE ATTACH PAGE FOR ABSTRACT

14. SUBJECT TERMS

15. NUMBER OF PAGES

16. PRICE CODE

17. SECURITY CLASSIFICATION OF REPORT	18. SECURITY CLASSIFICATION OF THIS PAGE	19. SECURITY CLASSIFICATION OF ABSTRACT	20. LIMITATION OF ABSTRACT
UNCLASSIFIED	UNCLASSIFIED	UNCLASSIFIED	UNLIMITED

The stated objectives of this research effort were directed at:

* The estabishment at MIT of Magnetic LP-LEC growth capability with diameters approaching 4 inches.
* The design of heat and mass transport control systems required for optimization of growth with magnetic melt stabilization.
* Development of a model-based growth control scheme which includes complementary knowledge-based system inputs for seeding, shouldering, and growth termination.

Motivation for the proposed research was in the realization that property specifications established by advanced device technology could not be adequately met by the existing growth of GaAs was considered an essential element for desired technology transfer from academia to industry.

The conduct of research related to this proposal was affected in major way by two factors. A substantial reduction of funding forced a staff reduction to two principal investigators (AFW and SM) with primary focus on (a) crystal growth and (b) heat transport effects and control. Efforts directed at control of growth related defect formation were severly impeded by the non-existence of quantitative characterization techniques operating with microscale resolution at device dimensions. This deficiency rendered the viability of established property requirements, the informal control objectives, as fundamentally questionable. It motivated a major research undertaking in non-invasive GaAs characterization.

DEVELOPMENT OF MODEL BASED MAGNETIC LP-LEC GROWTH: LARGE DIAMETER GaAs

Final Technical Report

Period: 08/14/87 - 11/30/90
Amount: $1,702,802

Sponsored by:

Defense Advanced Research Projects Agency
Dr. Jane Alexander
703-614-1305

Monitored by AFOSR under Contract No. F49620-87-C-0106

Submitted by:

August F. Witt — Department of Materials Science & Engineering
617/253-5303

and

Shahryar Motakef — Department of Mechanical Engineering
617/253-5362

Massachusetts Institute of Technology
77 Massachusetts Avenue
Cambridge, MA 02139-4307

ACKNOWLEDGMENTS

The principal investigators and support staff associated with this research effort express their gratitude to Dr. R. Reynolds (DARPA, now Hughes Microelectronics Center) for his support and to Drs. S. Roosild, A. Prabhakar, and J. Alexander for their belief in the project and their assistance as needed. Acknoweldged also is the continuing encouragement and help provided by Dr. G. Witt (AFOSR) who monitored with insight, care, and wisdom.

CONTENTS

INTRODUCTION

The stated objectives of this research effort were directed at:

* The establishment at MIT of magnetic LP-LEC growth capability with diameters approaching 4 inches.
* The design of heat and mass transport control systems required for optimization of growth with magnetic melt stabilization.
* Development of a model-based growth control scheme which includes complementary knowledge-based system inputs for seeding, shouldering, and growth termination.

Motivation for the proposed research was in the realization that property specifications established by advanced device technology could not be adequately met by the existing growth technology which is largely based on empiricism. Broadening of the science base for growth of GaAs was considered an essential element for desired technology transfer from academia to industry.

The conduct of research related to this proposal was affected in a major way by two factors. A substantial reduction of funding forced a staff reduction to two principal investigators (AFW and SM) with primary focus on (a) crystal growth and (b) heat transport effects and control. Efforts directed at control of growth related defect formation were severely impeded by the non-existence of quantitative characterization techniques operating with microscale resolution at device dimensions. This deficiency rendered the viability of established property requirements, the informal control objectives, as fundamentally questionable. It motivated a major research undertaking in non-invasive GaAs characterization.

EXECUTIVE SUMMARY

This DARPA sponsored effort led to the establishment of an academic semiconductor growth research center with unique capabilities. It encompasses computer controlled growth of Si at diameters of up to 6-inches from magnetically stabilized melts, growth of GaAs at diameters of up to 3-inches by magnetic LP-LEC pulling, crystal processing, and characterization. Recently a non-invasive wafer inspection system has been developed. It is based on NIR transmission microscopy with bright and dark field illumination. Supported by computational image analysis, it provides for rapid quantitative characterization of doped and non-doped SI GaAs on both a macro- and selected microscale making it compatible with fab-line operation.

Model-based control of thermal stresses in LEC growth of GaAs has been implemented. In this approach a mathematical model of the growth process and a Heat Exchange System designed and constructed with the framework of the research project are used to control the temperature field in the crystal during growth and cooldown. Crystals grown in this configuration exhibit dislocation densities in the range of 10^3 cm^{-2}. Also developed was a micro-mechanical constitutive law for high temperature creep and dislocation multiplication in GaAs. According to this model, currently attainable dislocation densities of the order of 10^3 cm^{-2} are related to stress-induced dislocation multiplication in the matri .. Fundamental considerations related to the attainable degree of radial temperature uniformity in LEC-grown crystals suggest that attempts at further reduction of dislocation density should focus not only on thermal field control, but also on identification of the genesis, as well as physico-chemical approaches to elimination, of dislocation nucleation in GaAs matrices.

NOTE

For the convenience of the reader, abstracts of publications in the open literuature, generated by this research effort, are presented in the Research Digest. The most recent work published and that accepted for publication and in press is submitted in the Research Report.

RESEARCH DIGEST

Real Time Thermal Imaging For Analysis And Control of Crystal Growth By The Czochralski Technique: A real time thermal imaging system with temperature resolution better than $\pm 0.5°C$ (1000°C to 1500°C) and spatial resolution of better than 0.5 mm has been developed. It has been applied to the analysis of melt surface thermal field distributions in both Czochralski and liquid encapsulated Czochralski (LEC) growth configurations. The sensor can provide single/multiple point thermal information; a multi-pixel averaging algorithm has been developed which permits localized, low noise sensing and display of optical intensity variations at any location in the hot zone as a function of time. Temperature distributions (gradients) are measured by extraction of data along a user selectable linear pixel array and are simultaneously displayed, as a graphic overlay, on the thermal image. (*submitted to J. Crystal Growth*)

Determination of Free Charge Carrier Distribution and Micro-Segregation of Dopants in n-Type GaAs: An experimental approach to the rapid determination of the micro-distribution of free charge carriers in n-type GaAs is reported. Computer based video processing techniques are used to determine the IR absorption characteristics of wafers with a spatial resolution of less than 10 mm and to convert this data after calibration into charge carrier density. The application of this technique to a microsegregation analysis of Te-doped GaAs is demonstrated. (*J. Crystal Growth 91, 1988, 239-243*)

Quantitative Optical Determination of Segregation in Doped Silicon: A Comparative Analysis with Spreading Resistance Measurements: The net free charge carrier distribution in Sb-doped silicon, on a microscale, was quantitatively determined through near infrared transmission measurements. This data is compared with those computed from spreading resistance measurements; the two free charge carrier profiles are found to be in excellent agreement with each other. The data based on optical measurements reflect increased spatial resolution. (*J. Crystal Growth 91, 1988, 652-654*)

Microsegregation in Conventional Si-doped LEC GaAs: The dopant distribution in <100> Si-doped GaAs was quantitatively analyzed using NIR transmittance measurements with a spatial resolution of better than 2 μm. Microsegregation inhomogeneities, in the form of striations, are found to be random and discontinuous; they are identified predominantly as abrupt dopant concentration decreases resulting from temporal, localized back melting associated with turbulent convection in the melt. Variations in free charge carrier density associated with the striations approach in many instances two orders of magnitude and are thus by a factor of ten larger than anticipated and reported in the open literature for Si and Ge. Periodic striations normally associated with rotational crystal pulling are absent. (*J. Crystal. Growth 108, 1991, 508-518*)

Quantitative Analysis Of The Effects Of Vertical Magnetic Fields On Microsegregation In Te-Doped LEC GaAs: Using NIR transmission microscopy with computational absorption analysis, the effects of axial magnetic fields on micro- and macrosegregation during LP-LEC growth were quantitatively investigated with a spatial resolution of about 2 μm. Segregation inhomogeneities exceeding one order of magnitude are found to be related to fluid dynamics of the melt. The applicability of the BPS theory as well as the non-applicability of the Cochran analysis are established. (*submitted to J. Crystal Growth*)

Decorated Dislocations in SI-GaAs as Revealed by Dark Field NIR Transmission Microscopy: Using NIR transmission microscopy with dark field illumination and computational image processing it was possible to reveal decorated dislocations in doped n-type and doped as well as undoped SI GaAs. All observed dislocations in SI material are decroated with a high linear density of precipitates ranging in diameter from below the resolution limit (~200Å) to in excess of 2 μm. The NIR analysis is characterized by simplicity and speed; it is non-invasive and amenable to fab-line operation. (*J. Crystal Growth, in press*)

A High Temperature Creep Model for GaAs: The micro-yield model of Haasen and the existing data-base are used to generate a high temperature creep model for undoped GaAs. The proposed model is consistent with the high- and low-temperature data on

critical resolved shear stress (CRSS) and the low-temperature data on dislocation velocities in the matrix. (*J. Crystal Growth 108, 1991, 33-36*)

Fundamental Considerations in Creep-Based Determination of Dislocation Density in Semiconductors Grown from the Melt: The suitability of the Alexander and Haasen (AH) creep model for calculation of dislocation multiplication rates in melt grown GaAs and InP is analyzed. To this end a model consisting of two deformation stages is identified: (a) stage-I corresponding to the period immediately following solidification of the material, and (b) stage-II corresponding to the subsequent evolution of the thermal strain field in the crystal. Comparison of calculated and observed density of dislocations and fundamental consideraitons suggests that dislocation multiplication occurs, primarily away from the growth interface and not immediately upon solidification. CRSS-based thermo-elastic calculations as well as quantitative approaches for reduction of dislocation identifed by this formulation are shown to be consistent with the AH model. (*J. Crystal Growth, in press*)

Model-Based Control of Thermal Stresses During LEC Growth of GaAs: Validation of Thermal Model: A numerical model and a Heat Flux Control System (HFCS) are used to control thermal stresses during LEC growth of GaAs. This model-based control strategy has resulted in growth of low dislocation density crystals. In this first part of the study the growth configuration, design details of the HFCS, and the numerical model of the process are described, and experiments aimed at validation of the thermal aspects of the model are discussed. Results indicate good agreement between the experimental and modeling results. In the early stages of grwoth the difference between the predicted and measured temperature fields is found to be within the overall accuracy of model assumptions. The model accuracy in predicting the stresses in the crystal beyond the initial stages of growth is found to be $\pm$ 0.2 x CRSS of the matrix evaluated at its melting point temperature. The process is, therefore, sufficiently accurate to provide for unambiguous and accurate control of stresses in the growing crystal at levels lower than the CRSS of the matrix. (*J. Crystal Growth, in press*)

Model-Based Control of Thermal Stresses During LEC Growth of GaAs: Crystal Growth Experiments: A Heat Flux Control System (HFCS) developed to provide for active control of the thermal environment of LEC growth process, and a numerical model capable of accurate prediction of the thermal field in the growth system are used to control stresses during growth and cool-down of GaAs crystals. Three crystal growth experiments using this combination of hardware and modeling capability are reported. Results indicate that by maintaining thermal stresses in the crystal at below the critical resolved shear stress (CRSS) of the matrix, low dislocation density (EPD approx. 3000 cm^{-2}) material can be obtained. The EPD in crystals experiencing stresses larger than this value are one order of magnitude higher. Issues related to crystal-melt separation and diameter control as well as various approaches to integration of the model with the growth process are discussed. (*J. Crystal Growth, in press*)

Comparison of Calculated and Measured Dislocation Density in LEC-Grown GaAs Crystals: Dislocation densities in melt-grown GaAs crystals, ranging from 3×10^3 to 7×10^4 cm^{-2}, are compared to values pridicted by a micro-mechanical creep model based on the Alexander-Haasen formulation of slip in diamond crystals. The temperature and thermal strain histories of the crystals are obtained from the numerical simulation of the growth and cool-down processes. These histories are used in the creep model, and the associated time-variation of dislocation densities are calculated. The measured and calculated dislocation densities show a remarkably good agreement in the central region of the crystal. Toward the crystal periphery, however, the measured dislocation densities are appreciably larger than the rpedicted values. The possible reasons for this anomaly are discussed. The reported agreement between model and experimental results indicates that dislocation densities as low as 10^3 cm^{-2} are related to thermal-stress-induced slip in the matrix. The implications of this finding on various approaches for reduction of the dislocation density in melt-grown crystals to below currently attainable levels or high-10^2 to low-10^3 cm^{-2} are discussed. (*J. Crystal Growth, in press*)

RESEARCH REPORT

REAL TIME THERMAL IMAGING FOR ANALYSIS AND CONTROL OF CRYSTAL GROWTH BY THE CZOCHRALSKI TECHNIQUE

Introduction and Background

The growth of semiconductor single crystals by the Czochralski pulling technique and, in particular, the growth of compound semiconductors from liquid encapsulated melts, requires knowledge and precise control of the thermal field in the melt and the growing crystal [1,2]. The spatial temperature distribution in the melt is a complex function of the hot zone characteristics, the crystal and the environmental thermal boundary conditions. In conventional growth systems, a single-input-single-output (SISO) closed loop proportional, integral and derivative (PID) controller is used to maintain and/or change a single temperature to accomplish the task of controlling the temperature distribution in the melt. The sensors widely used for this purpose are thermocouples or single color pyrometers. The single point sensor's location, by tradition determined empirically, is well removed from the area of measurement interest: the melt and melt/crystal interface (figure 1).

Shortcomings of the practiced single point temperature measurement and control relate to its inability of providing critical information on prevailing stability, symmetry and gradients of the thermal fields in the melt about the rotational crystal pulling axis. Thus, conventional temperature sensing can be used for crystal diameter control but fail to support efforts directed at the minimization of radial and micro- segregation as well as the suppression of stress related defect formation.

Theoretical Basis for Image Interpretation, Hardware Configuration and System Architecture

The relationship between changes in optical intensity (I), temperature (T) and wavelength (λ) is established by Wien's approximation [eq. 1] to Planck's radiation law.

$$I(\lambda, T) = C_1 \frac{\epsilon(\lambda, T)}{\lambda^5} e^{\frac{-C_2}{\lambda T}} \qquad [1]$$

C_1 and C_2 are constants, 3.7403×10^{-4} watt μm^2 and 1.438×10^4 $\mu m \cdot K$ respectively and ϵ is the emissivity of the melt. The operation of the thermal imager is based on the theoretical principles of single color optical pyrometry. The high temperature scene (the silicon or encapsulated GaAs melt) is viewed in near normal incidence (see fig. 2) by a high resolution (512 x 512 pixels) low noise (-60 dB) charge coupled device (CCD) camera (RCA,

TC2855). A narrow bandpass filter (3 nm FWHM, centered at 633 nm) is placed between the scene and the camera. In this way, an array of 1/4 million discrete optical pyrometers are available to characterize the scene with a spatial resolution of better than 0.5 mm. The transmission wavelength of the filter was chosen to approach the peak in the spectral sensitivity of the CCD element while maintaining a steep slope on the I vs T (gray body) curve of the emitting (melt) surface.

A schematic of the thermal imaging architecture and a preliminary control structure is shown in figure 2. The major components include the GaAs growth system (modified Hamco CG-800) with axial superconducting magnet (5 kgauss, American Magnetics), the CCD camera and narrow bandpass filter, the image processing subsystems (Recognition Technology, Inc.) with high resolution analog RGB monitor and the host computer with integral high speed data acquisition and control capability (Masscomp MC-5510).

The camera generates information at 30 frames/second using a standard RS-170 (B/W) configuration. The analog video information is archived on 3/4-inch video tape (Sony BVU-800) and sent to the analog to digital subsystem where gain and dc offset are adjusted to permit operation at high gain for maximum sensitivity (temperature resolution). The signal can be pre-processed with user definable look up tables (LUT) to correct for inherent nonlinearities within the camera and is finally digitized to 8 bits (256 gray levels). Image processing functions are carried out in the pipelined pixel processor. These include calculation of two dimensional convolutions and temporal averaging with gain adjustment. Digital storage units (image memory) are used to hold starting, intermediate and final images during these procedures. Image transfer to and from the storage locations is provided by the pipelined pixel processor under software control. A unique capability of the imaging system is the dual ported nature of the digital storage units. The image memory thus appears as extended system memory to the host computer. As a result, image data can be accessed simultaneously by the pipelined pixel processor and the host CPU. In this way, parallel processing of the information can be accomplished with no performance penalty; the data extracted from the images can be processed while image processing functions continue. Real time graphics overlays of extracted and filtered image data and linear convolutions are produced in this manner. Two of the digital storage units are configured as a 16 bit pair to hold high precision intermediate results produced during certain image processing calculations (e.g. 2-d convolutions and temporal averaging). A third 1024 x 1024 x 8 image memory unit is configured as four contiguous 512 x 512 x 8 digital storage units which act as entrance and exit points for image processing calculations. Provision is also made for storage of select individual digital images on magnetic disk.

The processed images are sent back (in real time) through the A/D subsystem where a second LUT is used to false color the outgoing monochrome signal; the human eye is more sensitive to small changes in color than equivalent changes in brightness (gray

level). The LUT is defined to map low intensities to blue and high intensities to red with a linear interpolation of the complete 8 bit dynamic range. In this way, a complete spectrum between blue and red corresponds to intensities from 0 to 255 gray levels. The output is displayed (with the graphics overlays) on a high resolution RGB monitor.

Optical intensity information is selectively extracted from the thermal image, processed by the host CPU, displayed as a graphic overlay on the real time imaging signal and then passed, via the host, to the Data Acquisition and Control Processor (DACP). For temperature control purposes, this data is scaled and offset to conform to the output characteristics of a platinum/platinum-10% rhodium thermocouple and sent from a digital to analog (D/A) converter to the analog temperature control system on the console. Figure 2 also indicates alternate strategies for growth control based on signals from the thermal imager. For example, development is in progress to adjust, by computer, the magnitude of the axial magnetic field for closed loop control of the radial temperature gradient in the melt based on a line scan of the surface temperature field obtained from the thermal imager. In like manner, the thermal field within the growing crystal can be controlled through a heat exchange system (HES) mounted coaxially about the growing crystal.

Thermal Imaging of High Temperature Semiconductor Melts

The thermal imaging geometry in Czochralski configuration is illustrated in figure 3. By necessity, the CCD camera is mounted off-axis and non-normal to the melt surface. As a result, the contribution of low level internal reflections from the melt surface to the image is minor. The high temperature scene comprises the melt,crucible/susceptor, heater elements and crystal. The portion of the scene containing optical information convertible to temperature is provided by the flat surface of the melt.

A raw (unprocessed single frame) thermal image of a conventional liquid encapsulated (B_2O_3) GaAs melt at low pressure (30 psig) prior to seeding is shown in figure 4. Gray scale representation of the high temperature scene depicts high melt temperatures as bright and lower temperatures as progressively darker. The horizontal line crossing the encapsulated melt represents the linear array of picture elements (pixels) from which temperature data can be extracted, processed and displayed in real time as a radial temperature profile. Such data is shown as the curved line superimposed on the displayed horizontal pixel array. It has been processed by a linear convolution to remove unavoidable high spatial frequency components. The data processing is off loaded from the pipelined pixel processor to the main CPU so as to maintain real time image processing performance. The gray level scale on the ordinate corresponds directly to temperature. (Calibration of the gray scale is discussed below.) Thus, the slope at any point on the graph indicates the magnitude of the radial temperature gradient. The image reveals a series of trapped bubbles near the periphery of the melt. These bubbles, inevitably present subsequent to melting of the charge, mask temperature information. Continuous temporal averaging of consecutive images (with exponential deemphasis of

previous frames) is used to 'eliminate' the effect of these spatial perturbations (figure 5). It is understood that the effectiveness of this type of averaging for the reduction of temporal noise requires rotation of the melt. This image processing procedure operates in real time and the number of frames averaged is user selectable.

Figure 6 is a thermal image taken during the initial stages of GaAs growth. The bright disk just below the seed shaft is the growing crystal. It appears bright (red, in false color) due to the higher emissivity of the solid compared to the melt as well as its reflecting the high temperature information coming from the crucible wall. The intensity does not, in this case, unambiguously reflect the temperature of the crystal. With more quantitative information about the emissive nature of the crucible and crystal this temperature distribution could also be determined. Even so, the abrupt discontinuity of the optical intensity observed on crossing the melt/crystal boundary provides useful information concerning the diameter of the growing crystal and can, in principle, be used as a feedback signal for diameter control. This measurement has significant advantages when compared to the measurement of differential weight which is used in conventional LEC growth systems for ADC (automatic diameter control) [3].

Figure 7 shows the same growth configuration with the application of a 2000 gauss axial magnetic field. Comparison of the displayed data with that in figure 6 (no field) indicates an increase in radial temperature gradient in the presence of the magnetic field. The magnetic field reduces the convective component of heat transfer in the melt. Based on the measured correspondence between gray level and temperature (0.5°C/gray level, see section on systems calibration), the radial temperature gradient in the absence of the field was measured at less than 5°C/cm whereas the temperature gradient with melt stabilization of 2000 gauss was measured to be in excess of 10°C/cm.

Isotherms, corresponding to constant intensity contours, are revealed by highlighting selected gray levels. Note the diffuse nature of the isotherm representation in figure 8, a single frame thermal image. This diffuse appearance is primarily attributable to high spatial frequency noise which can be eliminated on a full frame basis. For this purpose, a two dimensional convolution is performed in n frame times where n is the the number of non-zero elements in the convolution kernel (typically 8 of 9 in a 3 x 3 matrix). Thus, a complete convolution is accomplished in 8 frame times or 8/30 second. The convolved image (figure 9) illustrates a reduction in high spatial frequency noise; isotherms appear correspondingly in a more coherent form.

The foregoing thermal imaging capabilities are characterized by a view of the scene and display of the data at a particular point in time. Another approach, found to be useful for systems control purposes, is to extract and display intensity (temperature) data from an nxm array of pixels as a continuous function of time. Figure 10 shows the result of a pixel averaging algorithm which takes intensity data from a 3x3 array of pixels, arithmetically averages it and displays the results in real time overlayed on the thermal

image. The data indicate a high degree of surface temperature stability over an extended (> 30s) period of time.

System Calibration

Two techniques were employed to calibrate the thermal imager. Both permit the relative determination of temperature; i.e. temperature changes/differences are measurable quantitatively. In the first approach, a magnetically stabilized melt was held at constant temperature using a conventional temperature control scheme where the sensing thermocouple was in close proximity to the heater. Three gray levels (isotherms) were highlighted at 20 gray level intervals. The choice of these absolute intensities was made so as to indicate the optical emission at three positions on the melt surface: one near the melt periphery, one at approximately the half radius position and one near the center of the melt. The temperature was subsequently increased, forcing these highlighted gray levels to move toward the center until, at temperature T+10°C, the innermost (coldest) isotherm has all but disappeared and its previous position (at T) had been taken by the second (middle) isotherm. This superposition of isotherms was repeated once more as the temperature was again ramped. At T+20°C the third isotherm (originally near the crucible wall) was located in the same position as that of the first isotherm at temperature, T. Accordingly, over this temperature range, 20 gray levels correspond to a difference of 10°C; i.e., the sensitivity of the thermal imager is given as 0.5°C per gray level. The second calibration was conducted by imageing the bottom of the graphite crucible susceptor with a thermocouple to measure the imposed temperature changes at the half radius position. Using the algorithm described above for measuring the optical intensity at a point, the gray level output of the thermal imager (averaged 9x9 pixel array) was amplified, scaled, processed by a digital to analog converter and directly compared to the response of the thermocouple. Figure 12 shows the relationship between the outputs of the thermocouple in °C and the thermal imager in volts. These data reflect the same value for calibration as the first method: 20 gray levels for every 10°C.

Temperature Control by Thermal Imaging

Conventional temperature control schemes in Czochralski growth configuration (figure 1) are based on sensor locations well removed from the critical area of interest. Using the thermal imager as a single point sensor the temperature of the growth system was controlled from within the crucible and, thus, from a more process sensitive position. The intensity (temperature) information from the imager was re-scaled (gain and dc offset) so that the output of the D/A converter, after processing by a 1000:1 voltage divider, corresponded directly to that of a Pt/Pt-10%Rh thermocouple. In this way, the signal could be fed to the conventional, analog PID controller which had previously been used to control a thermocouple placed near a heater element. Figure 13 shows the results of 5°C control changes made with the analog controller. The output of the thermocouple located within the crucible and the old control thermocouple (at the heater) were recorded. In both cases, the change in output corresponds to the temperature changes

made at the controller indicating that the signal from the thermal imager successfully tracked and measured the temperature response of the system. The decaying oscillatory component of the temperature response reflects non-optimized PID parameters of the analog controller which were left unchanged from those previously used for conventional temperature control sensed at the heater.

Discussion

One of the outstanding features of themal imaging for high temperature crystal growth is in the great facility with which time dependent changes in temperature can be recorded and, in various ways, used as input for systems control. The approach is non-invasive and applicable to point, line and area measurements through software selection.

The interpretation of the output of the thermal imager as temperature information is more complicated. It is based on three fundamental assumptions. First, the high temperature scene is viewed in normal incidence to eliminate effects of internal reflections. Second, the emissivity of the melt does not change over the temperature range of interest. And, third, the characteristics of the optical path are time independent. In this context, it is of interest to analyze the degree to which these assumptions are met in the present experimental configuration and what effect any deviation from these assumptions have on image interpretation.

In the reported configuration (figure 2), the camera views the melt at an inclination of about 5° to the normal. The effect of this non-normal incidence is evident during observation of metallic (specular) melts where isotherms appear shifted from a centro-symmetric position (figure 8). No such effect is observed, however, when imaging the empty graphite crucible (non-specular); isotherms appear concentric about the center of the crucible. This finding suggests that, when imaging the melt surface, high temperature information from the crucible wall is being reflected by the specular melt to the thermal imager. Work is in progress to negate this effect by subtraction of a reference image containing information characteristic of the reflection.

There is no indication that the emissivity of the melt changes measurably over the temperature range encountered during a typical growth experiment. However, a change of the 'effective' emissivity of the melt does occur as a result of changing optical effects associated with gas bubbles in the encapsulating layer (figure 4). Compensation of this effect, for example during crystal diameter and/or temperature sensing, is being approached by modifing the temporal averaging algorithms for inclusion in the systems control software.

The characteristics of the optical path are subject to a significant aberration from assumed behavior over the course of a growth experiment. During this time: 1. Transmission through the window used to view the melt is subject to time dependent change due to deposition of volatile constituents in the system. 2. The optical transparency of the encapsulant changes as its chemistry is modified by the interaction of

the melt with its environment. These effects can be corrected for by image subtraction if the changes to the characteristics of the optical path are reproducible and well characterized. It is preferable, however, to approach this problem through elimination of the causes rather than the effects.

Summary

A high resolution thermal imaging system which operates in real time has been developed. It has been used to characterize the radial temperature distributions in high temperature semiconductor melts. This system also operates as an advanced non-contact temperature sensor and has been used to actively control the temperature of a low pressure LEC GaAs crystal puller. High performance spatial and temporal filtering algorithms have been applied to reduce high spatial frequency noise inherent in both the process and the measurement. This technique is potentially well suited to thermal characterization and control of other materials processing technologies. The non-contact aspect of the design makes it attractive to those applications where non-intrusive measurement of temperature is required.

References

1. K. Morizane, A.F. Witt and H.C. Gatos, J. Electrochem. Soc. **114** (7) 738 (1967).
2. A.F. Witt and H.C. Gatos, J. Electrochem. Soc. **115** (1) 70 (1968).
3. M.A. Gevelber, M.J. Wargo and G. Stephanopoulos, J. Crystal Growth **91** 199 (1988).

Figure Captions

Fig. 1 Locations of temperature sensors for control in conventional Czochralski and Liquid Encapsulated Czochralski (LEC) growth configurations. Typical sensors include thermocouples and optical pyrometers.

Fig. 2 Thermal imaging architecture and preliminary control structure for LEC growth of GaAs. The use of closed loop feedback and feedforward trajectories are discussed in detail in reference 4. Non-traditional control elements include the heat exchange system (HES) around the growing crystal and the superconducting magnet around the furnace.

Fig. 3 Geometry of thermal imaging system. Alternative temperature sensing locations and geometries are indicated. At present the line scan across the melt and crystal and the single point (cross-hair at heater element) have been implemented. Only the single point approach is currently used for control.

Fig. 4 Thermal image of an encapsulated GaAs melt. No processing has been done on the image. However, the data plotted in the graphic overlay has

been subjected to a linear convolution to remove high spatial frequency noise.

Fig. 5 Thermal image of an encapsulated GaAs melt. Temporal averaging has been used to 'eliminate' the effect of the bubbles.

Fig. 6 Thermal image of an encapsulated GaAs melt taken during the seeding process. No magnetic field is applied. Note the low radial temperature gradient indicated by the limited gray scale range of the intensity distribution across the melt.

Fig. 7 Thermal image of an encapsulated GaAs melt with an applied magnetic field of 2000 gauss. All growth conditions are the same as figure 6 except for the presence of the field. The radial temperature gradient is substantially increased.

Fig. 8 Isotherm representation on an encapsulated GaAs melt: 3000 gauss. No image processing has been applied to reduce high frequency spatial noise. Note the spatially diffuse nature of the isotherms.

Fig. 9 Isotherm representation after application of a two dimensional low pass filtering convolution utilizing a 3 x 3 convolution kernal. Note the reduction in high spatial frequency noise resulting in a more coherent representation of the isotherms.

Fig. 10 Thermal image of an encapsulated GaAs melt with graphic display of the output of a multi-pixel averaging algorithm. The optical intensity (temperature) data is taken from a single point (defined by the cross-hair) and displayed in real time.

Fig. 11 Calibration of the thermal imager. Three thermal images are depicted where the temperature increases in 10°C increments between them. The isotherms shown in each image are at the same gray levels. See text.

Fig. 12 Calibration of the thermal imager. The plot on the left is the output of a thermocouple located in the crucible. The plot on the right depicts the output of the thermal imager scaled to permit plotting on the same instrument. Results are the same as for the technique illustrated in figure 11. See text.

Fig. 13 Temperature control of an LEC GaAs puller using the thermal imager as an advanced sensor. Temperature changes are 5°C. The plot on the left is the output of a thermocouple located in the crucible. The plot on the right is the output of the thermocouple used for conventional control located at the heater (Note change in scale). The ringing in the control response is due to

non–optimized PID parameters used with the conventional controller which was driven by the imager. See text.

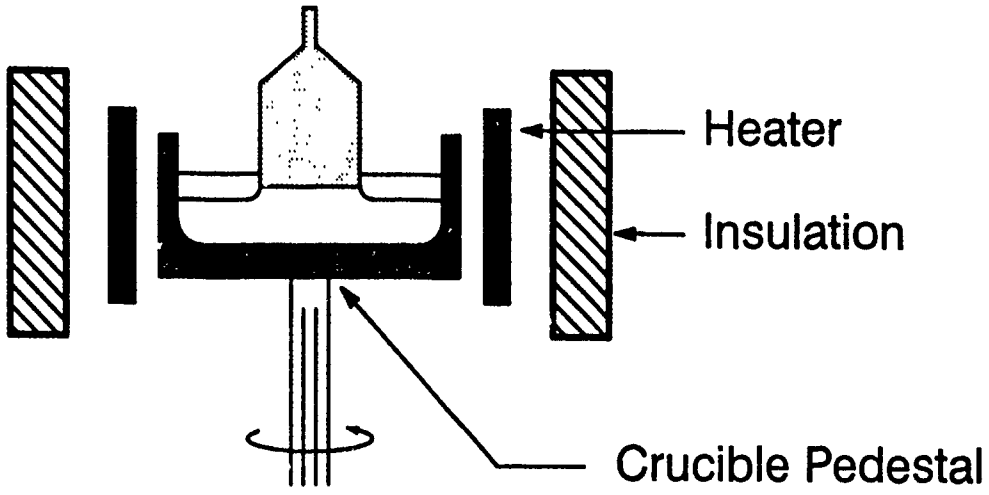

Figure 1

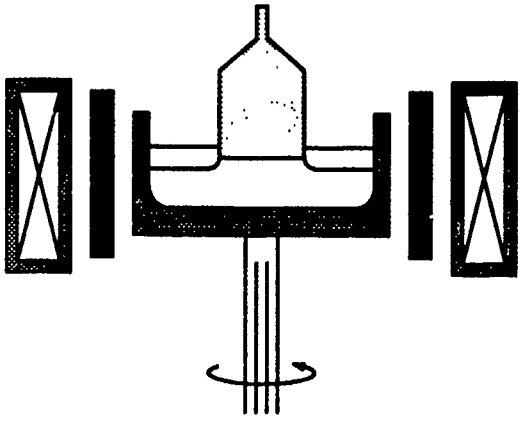

Pipelined Pixel Processor

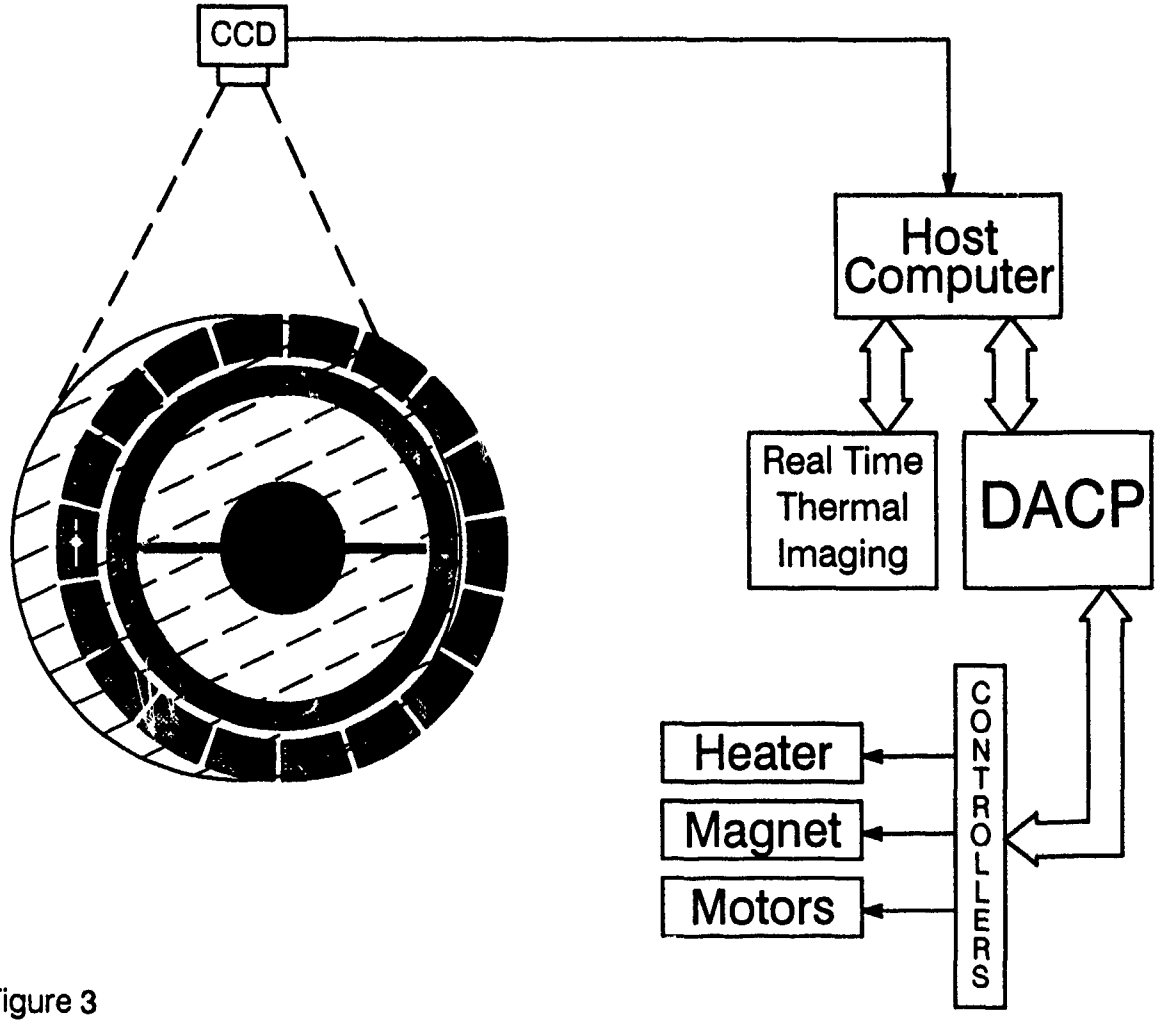
CCD
Host Computer
Real Time Thermal Imaging
DACP
Heater
Magnet
Motors
CONTROLLERS

Figure 3

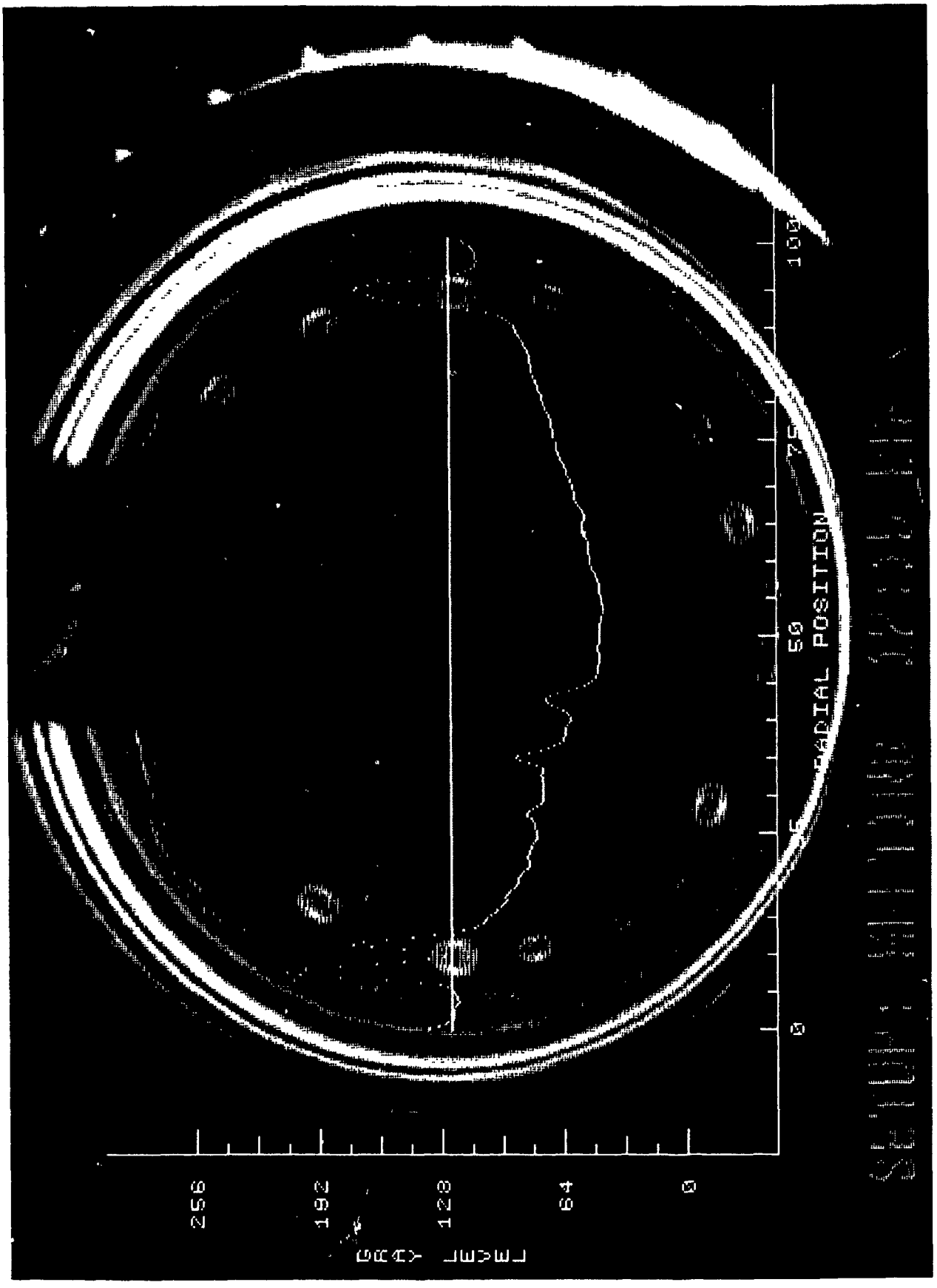

Fig. 4

RADIAL POSITION
0
25
50
75
100
256
192
128
64
0

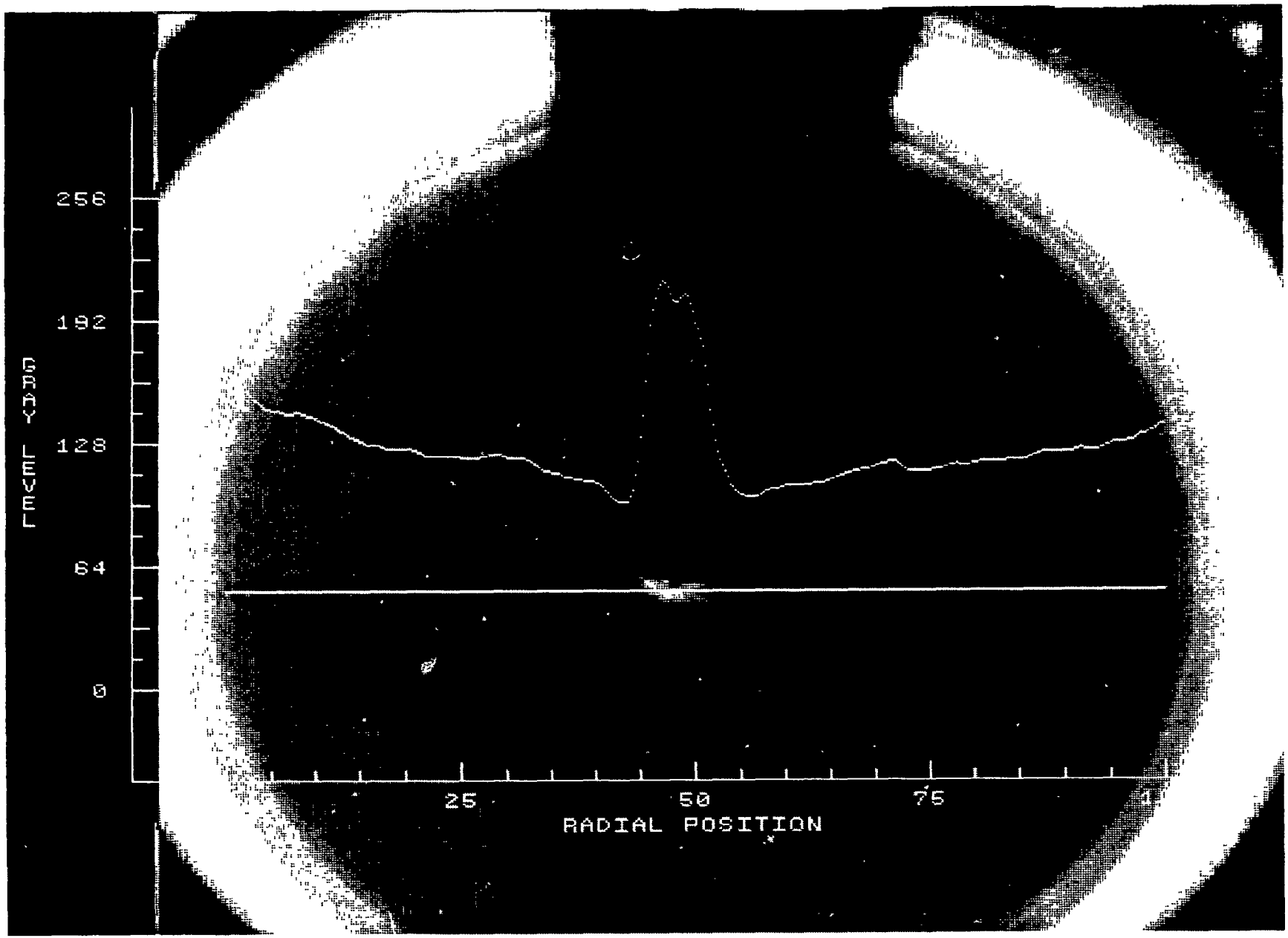

Fig. 6

RADIAL POSITION
0
25
50
75
100
256
192
128
64
0

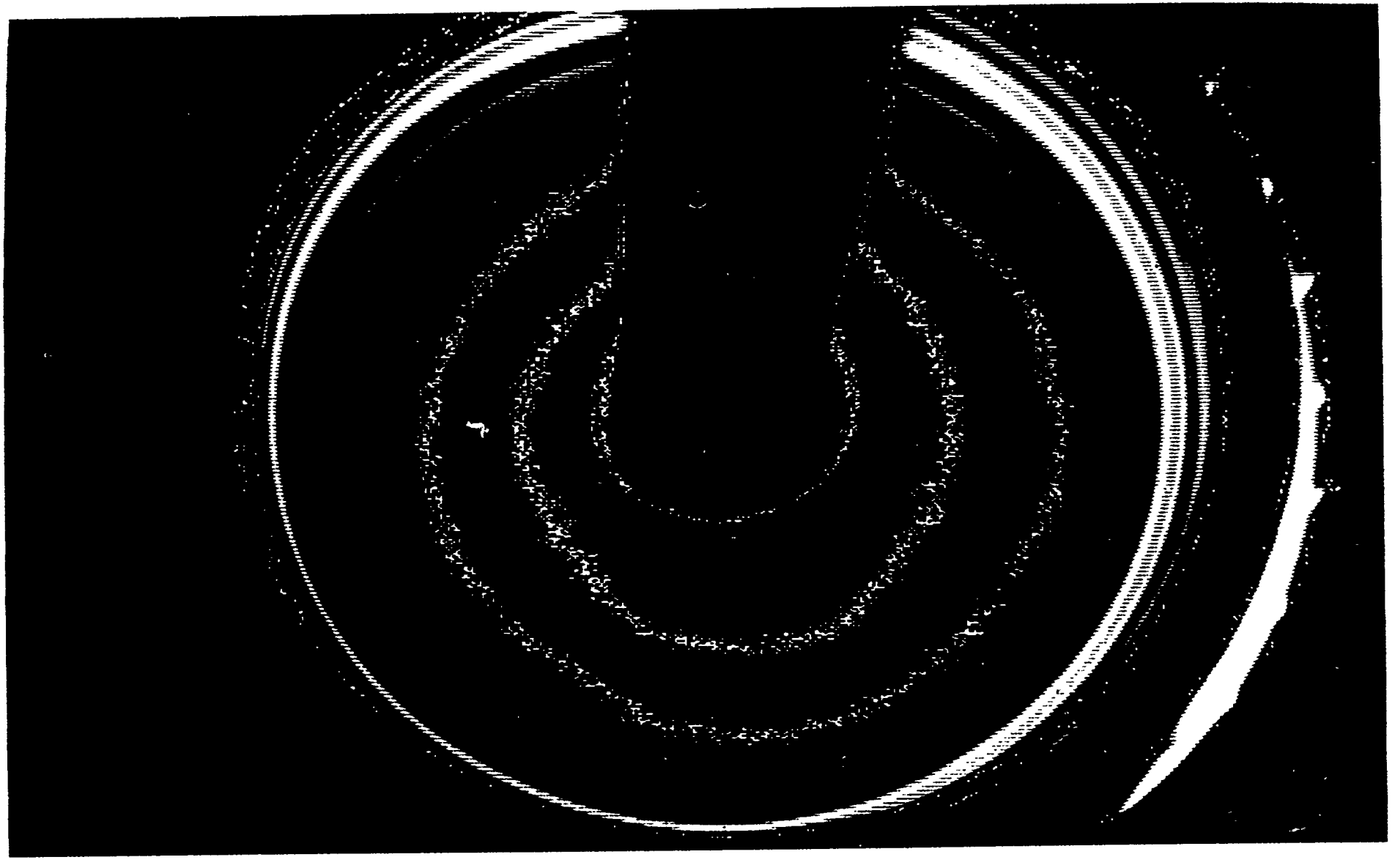

Fig. 8

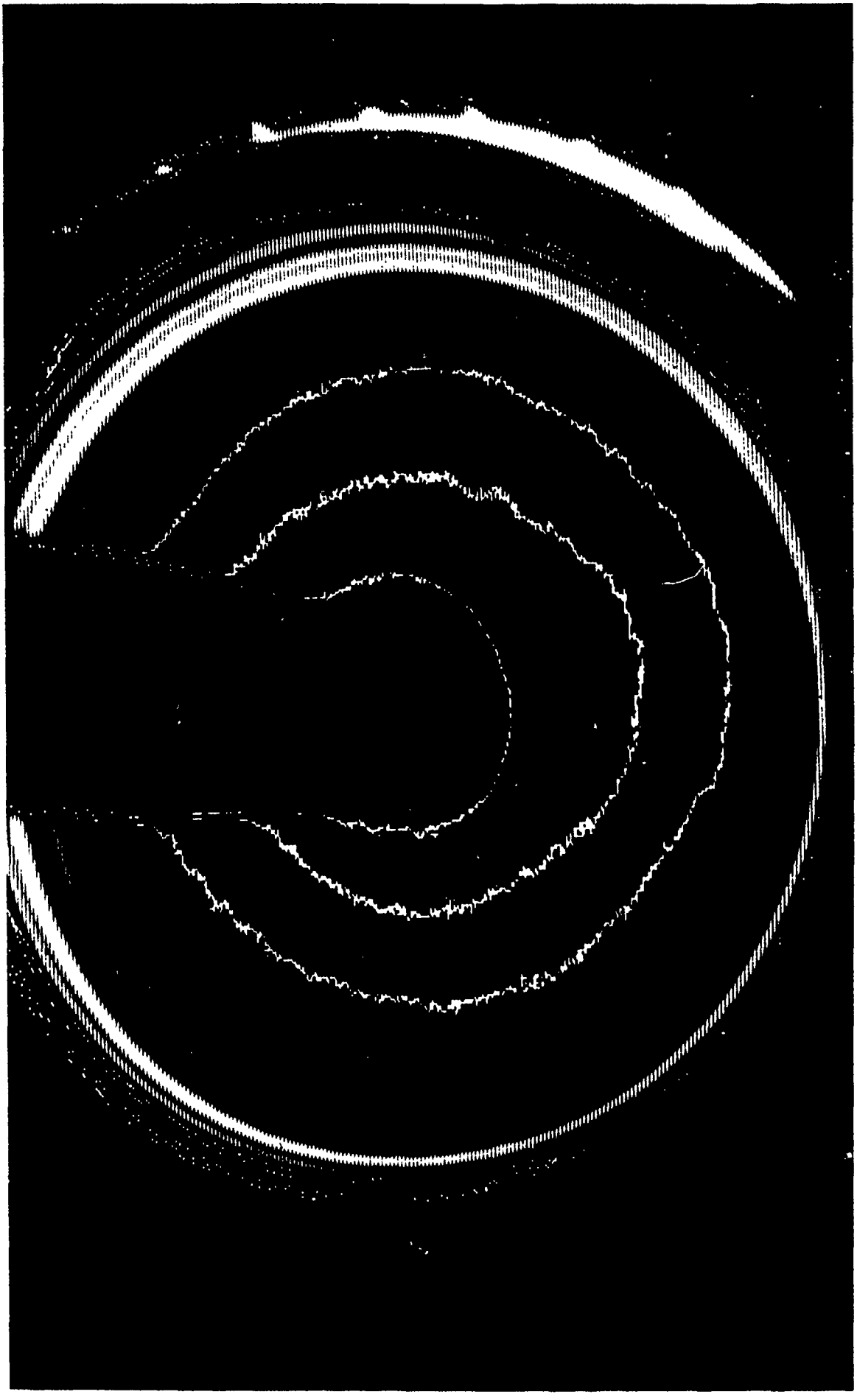

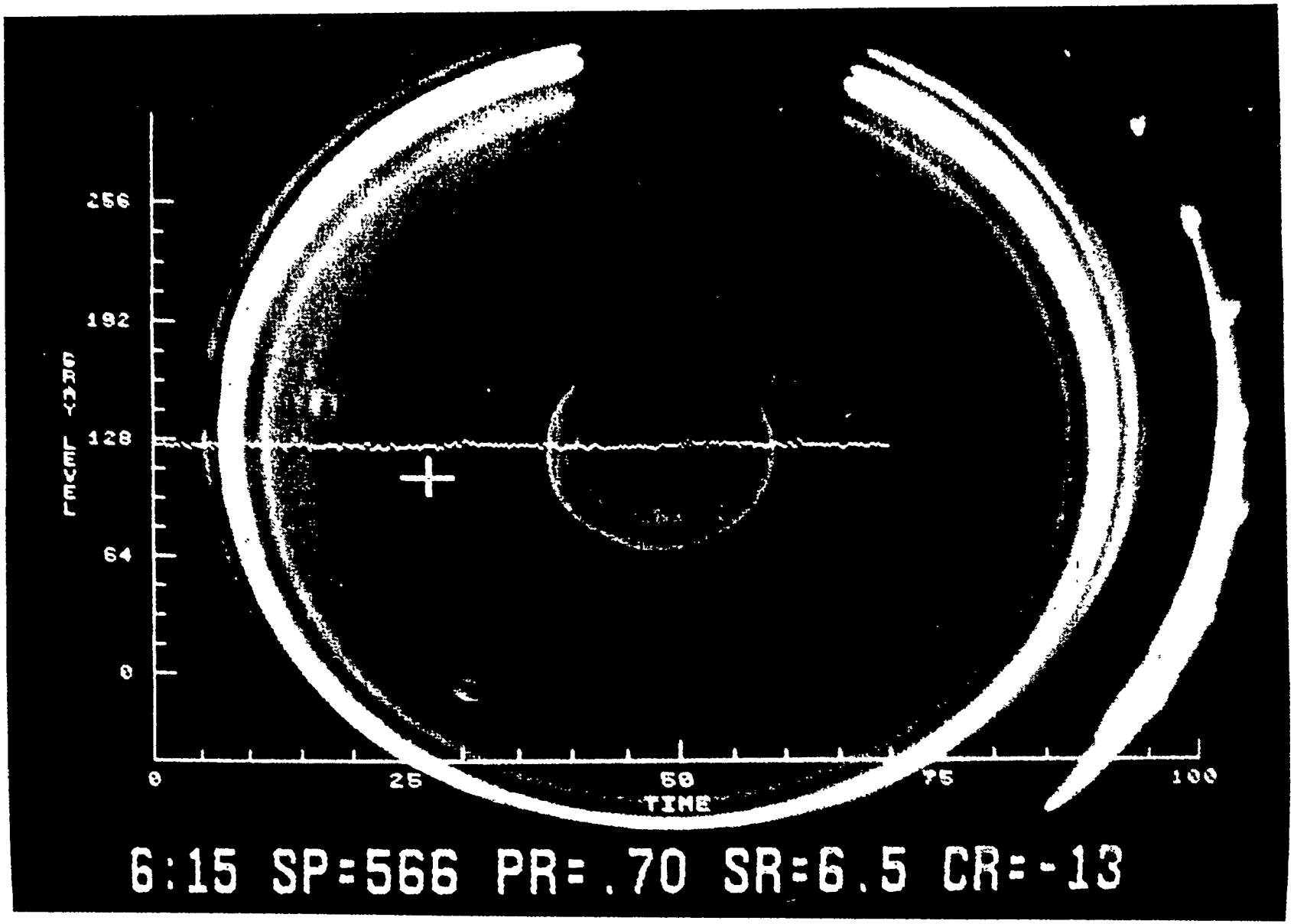
256
192
128
64
0
RECEIVER GAIN
0
25
50
75
100
TIME
6:15 SP=566 PR=.70 SR=6.5 CR=-13

#2
#1
#3
1000 Gauss
1
2
3
+10
+20

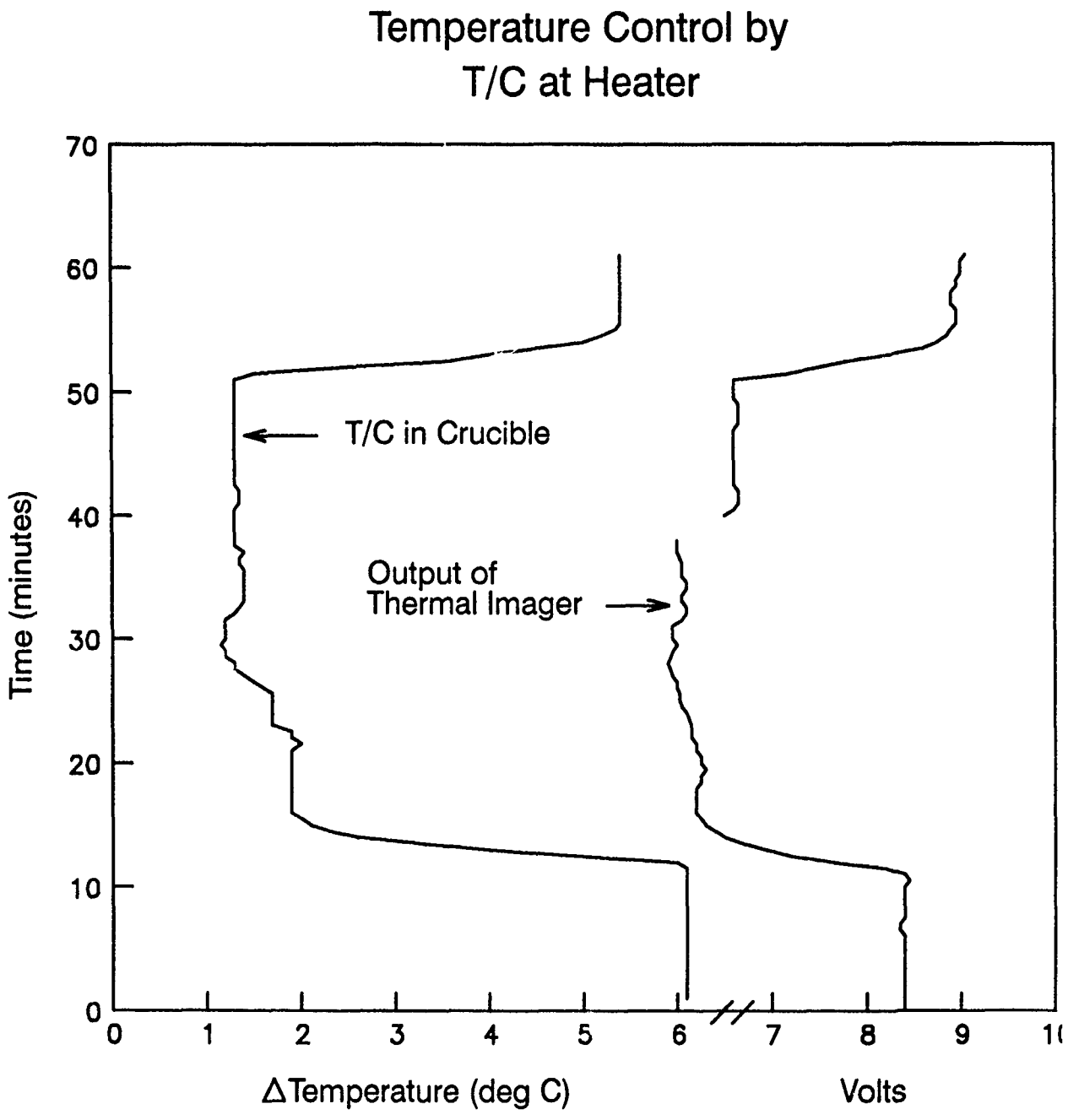
Temperature Control by
T/C at Heater
70
60
50
40
30
20
10
0
Time (minutes)
T/C in Crucible
Output of
Thermal Imager
0
1
2
3
4
5
6
7
8
9
ΔTemperature (deg C)
Volts

Figure 12

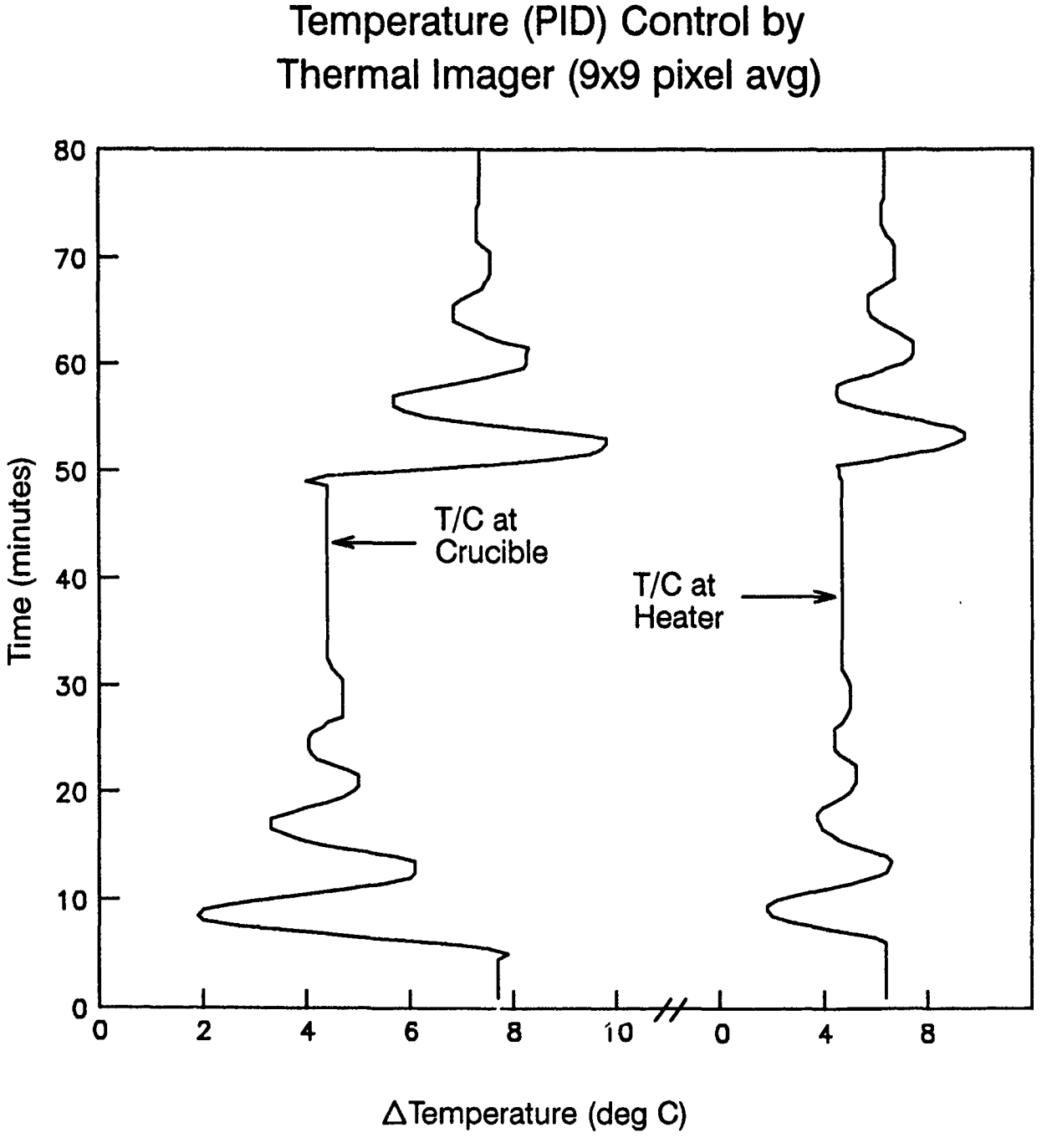
Temperature (PID) Control by
Thermal Imager (9x9 pixel avg)
Time (minutes)
80
70
60
50
40
30
20
10
0
T/C at
Crucible
T/C at
Heater
0
2
4
6
8
10
0
4
8
ΔTemperature (deg C)

Figure 13

MICROSEGREGATION IN CONVENTIONAL Si-DOPED LEC GaAs

Introduction

GaAs growth by Czochralski pulling from liquid encapsulated melts leads to structural and chemical defects which affect adversely its critical electronic and opto-electronic properties [1]. Efforts to ascertain the nature and origin of these defects, a prerequisite for their control and possible elimination through modified growth procedures, have so far met with limited success only. While some growth related structural defects such as dislocations, stacking faults, etc., can be quantitatively characterized on a device scale, chemical defects such as compositional fluctuations can not as yet.

For doped GaAs and pseudo-binary III-V compounds, the determination of composition on a microscale has so far been severely impeded by the limited sensitivity and spatial resolution of available analytical techniques. Studies of microsegregation have therefore been largely restricted to etching analyses [2] and, on a limited scale, to interpretation of mid-IR absorption [3,4].

The presently reported quantitative microsegregation analyses were carried out in conjunction with efforts to establish an experimental data base for the search of correlations between quantifiable growth parameters and the defect structure of GaAs single crystals grown at diameters up to 100 mm. The thrust of this work is directed at the clarification of microsegregation in commercial HP-LEC material through transmittance measurements with radiation in the 1 μm range. Net free charge carrier concentrations thus obtained in the n^+ type material studied are interpreted as dopant concentrations. The data are also used to elucidate the nature of the solidification process in LEC configuration.

Experimental Approach

The crystal sections examined in this study were cut parallel to the <100> growth axis from commercial 3 inch diameter Si-doped GaAs crystals grown by conventional HP-LEC Czochralski pulling from 4 kg charges at a pull rate of 9 mm/hr with seed and crucible rotation at rates of 8 and -20 rpm respectively. The 0.5 to 2 mm thick samples were lapped and polished on their front and back surfaces to permit microscopic near-infrared transmission analysis. The analysis and interpretation of NIR transmittance was carried out as described earlier [5].

The optical characterization uses NIR transmission microscopy (λ = 0.86 to 1.2 μm) in conjunction with computer based video image processing for transmittance measurements with optimized spatial resolution (fig. 1). A TV camera with an extended red Si-Vidicon is used to sense the light transmitted through the GaAs samples; the registered NIR transmission image is in real time transferred to an image processing

system and is digitized into a 512 x 480 pixel image with an 8-bit (256 gray levels) dynamic range. The image is thus effectively converted into a matrix of 2.5x105 detectors for transmitted radiation with diffraction limited spatial resolution.

To obtain transmittance ($T = I/I_o$) for each pixel position, the microscope, video and image processing systems are calibrated, accounting explicitly for camera gain and offset, light source intensity, and the numerical aperature of the optics. Calibration of the system was accomplished by equating the macroscopic transmittance (obtained from standard optical absorption measurements) of a series of GaAs wafers to the average measured gray level value across the field of view. This calibration, relating gray levels directly to transmittance (T), allows for the optimization of sensitivity in the determination of transmittance by the elimination of the need for independent measurements of I and I_o; transmittance was calculated directly from the measured gray level values.

With knowledge of the sample thickness (d) and transmittance (T), the absorption coefficient (α) at any point (pixel) on the image was obtained according to:

$$\exp(\alpha d) = \frac{(1-R)^2}{2T}\left\{1 + \left[1 + \frac{4R^2T^2}{(1-R)^4}\right]^{1/2}\right\} \qquad [1]$$

The reflectivity (R), 0.3098 [6], was found to be independent of the net free charge carrier concentration over the NIR wavelength regime used in this investigation.

For extrinsic, n-type GaAs it was found that the absorption coefficient (α) is proportional to the net free charge carrier concentration in both the near- and mid-infrared wavelength regimes [5,6]. This dependence can be expressed as:

$$\log n = \frac{1}{a}(\log \alpha + b) \qquad [2]$$

where the constants a and b are a function of wavelength in the near-infrared. Values for a and b were derived for this study (Table 1) from the correlation between the measured absorption coefficients (α) and the net free charge carrier concentration (n) determined from room temperature Hall effect measurements. This correlation indicates that greater sensitivity to changes in the free charge carrier concentration can be obtained at longer wavelengths for which, however, the spatial resolution is decreased. Measurements were performed at $\lambda = 1.0$ μm, thus realizing a compromise between spatial resolution and sensitivity. In conjunction with the present segregation studies, the net free charge carrier concentrations as determined optically are taken to reflect the dopant concentrations in the crystals. The effects of carrier compensation, amphoteric nature of the dopant element, and stoichiometry on the computed charge carrier profiles are presently taken to be second order effects and are not considered in this treatment. Justification for this

approximation is provided by segregation analyses of Te- and Si-doped GaAs at lower dopant concentrations which indicate analogue behavior.

Experimental Results

The NIR transmission micrograph of a double sided polished GaAs segment, 0.7 mm thick, cut parallel to the growth axis, is presented in fig. 2. The image, taken at a half radius position (to the right of the rotational axis), reveals a striated segregation pattern whose directionality reflects a concave growth interface morphology. The pattern of the striations, temporal fluctuations in dopant incorporation during growth, is similar at all longitudinal and radial positions in the crystal: it is aperiodic, of varying intensity, and discontinuous across the crystal diameter. The striations, of lenticular shape in the plane of observation, exhibit an average length of striation of about 10 mm and widths ranges up to about 20 μm. There is no evidence of rotation-related, periodic segregation effects, common in silicon [7], germanium [8] and other III-V compounds grown by conventional Czochralski pulling [9].

The observed microsegregation pattern reflects interference by turbulent melt convection with dopant incorporation during growth and is consistent with results of etching analyses reported in the literature [10].

Applying computational image analysis to the transmission micrographs, it is possible to determine quantitatively for each pixel position the corresponding free charge carrier concentration. Such an analysis for the area outlined in fig. 2 is presented in fig. 3. It identifies striations as localized decreases in dopant concentration from average values of about 2×10^{18} cm^{-3} to less than 2×10^{17} cm^{-3}. This type of striation, exhibiting widths ranging from 2 to about 20 μm and lateral dimensions between 5 to 15 mm, is observed at all axial and radial positions in the crystal. The spacing of successive striations is in all instances random; it provides only approximate information on the frequency of the perturbations responsible for their creation since the microscopic rate of growth associated with their formation is not predictably related to the pulling rate.

The radial macrosegregation effect in the GaAs was determined from free charge carrier measurements at 2 mm spacing across an arbitrary radius of the crystal. The corresponding dopant concentration profile shown in fig. 4 was obtained by averaging at each measurement location the free charge carrier profiles of longitudinal scans over a distance of 500 μm. The data thus obtained at the given radial positions are equivalent to those obtained by wafer profiling. Accordingly, a dopant concentration maximum exists at the crystal center which yields a radial segregation effect $[(c_{max} - c_{min})/c_{avg}]$ of about 10%. This macroscopic radial gradient is found to remain virtually constant over the investigated crystal length of about 7 cm (in which microscopic carrier fluctuations measuring more than one order of magnitude were observed). The average of the

optically determined free charge carrier concentration for the region analyzed in fig. 4 (2.4×10^{18} cm^{-3}) compares well with that obtained from room temperature Hall measurements (2.2×10^{18} cm^{-3}).

Discussion

Dopant segregation associated with LEC growth of GaAs, as revealed through quantitative NIR absorption, differs fundamentally from that observed in Si or Ge and is much more complex than projected from published electrical and etching studies. On a macroscale, GaAs is characterized by relatively high radial compositional uniformity, the appearance of random, discontinuous striations and the absence of rotational segregation effects. On a microscale, the magnitude of fluctuations in dopant concentration, as reflected in the free charge carrier density, exceeds that encountered in Si, for example, by close to two orders of magnitude. The significance of these microsegregation characteristics becomes apparent when considering the grown crystal in conventional wafer geometry. Within the surface plane of a wafer the dopant concentration (Si) varies by as much as one order of magnitude and more over distances of about one cm. In the direction normal to the wafer surface, charge carrier concentrations can change by up to two orders of magnitude over distances of about one micron (fig. 9).

The present findings, obtained on conventional, commercial material, can not be attributed to unusual growth conditions, but rather are taken to reflect the increased spatial resolution and sensitivity of the optical analytical approach used.

The effect of measurement resolution on the determination of microsegregation is examined in fig. 5. The free charge carrier profile, based on data determined optically with a resolution of 2.5 μm (A), is compared with profiles of 12.5 and 25 μm (B,C) resolution. (The data of lower resolution was obtained by averaging successively the values of 5 and 10 pixels along the linear array of 2.5 μm resolution.) The comparison shows that neither the period nor the amplitude of the compositional fluctuations, registered at high resolution, is preserved in measurements of low resolution. Moreover, it is found that the segregation characteristics, according to the measurements at lower resolution, are a function of the location of the starting point of the analysis. It is apparent from the present data that the magnitude of compositional fluctuations in GaAs must in actuality be even larger than measured in this study. However, the error related to limited resolution is expected to be small because of diffusive equilibration in the submicron range during growth and during annealing after growth.

Prerequisite for a quantitative segregation analysis is the availability of compositional data and knowledge of pertinent physical constants, primarily the distribution coefficients (k_o) and the diffusion constants (D_l) for the dopants in the melt. A literature search reveals for the given system "estimates" of D_l in the range from 5×10^{-3} to 1×10^{-5} cm^2/sec^{-1} [11] and effective distribution coefficients (k_o) ranging

from 0.02 to 2.0 with the majority of the reported values centering about 0.1 [12]. A quantitative approach is further complicated by the apparent dependence of k_o on the stoichiometry of the melt [13] and by the unavailability of stoichiometric information for the reported growth experiments. In view of this deficient available data base, the present segregation study is by necessity restricted to a phenomenological analysis of dopant redistribution during growth.

Viewed on a macroscale, the pattern of segregation (fig. 2) remains essentially the same at all parts of the crystal segment; the system experiences neither significant axial nor radial position dependence of segregation. On a microscale (fig. 3) all impurity striations appear on the plane of observation as lenticular in shape, extending laterally from 5 to 15 mm and exhibiting heights ranging up to about 20 μm (fig. 9). Fourier analyses of the striations reveal random patterns which exhibit no relationship to either seed or crucible rotation. Details of the compositional characteristics of individual striations, as depicted in fig. 3, are more evident in three-dimensional presentation (fig. 6). They are identified as irregularly spaced, abrupt dopant concentration decreases succeeded by more gradual recoveries of the dopant concentration to the average level. The magnitude of the concentration changes from maximum to adjacent minimum is found to vary, ranging from the sensitivity limit to in excess of a factor of fifty.

A phenomenological account of microsegregation emerges from an analysis of dopant distribution on both a macro- and microscale. It indicates on a macroscale the absence of significant radial segregation under conditions of varying curvature of the growth interface as well as the absence of any rotational segregation effects; on a microscale is recognized the existence of localized segregation transients which have all attributes of pronounced temporary melt-back and recovery phenomena. This experimental evidence suggests that dopant incorporation is controlled by turbulent convective melt flows which are accompanied by random temperature fluctuations and lead to the establishment of a shallow, spatially and temporally varying momentum boundary layer (δ) at the growth interface. It is noted that this set of the boundary conditions for growth and segregation of GaAs appears largely the same as that encountered during growth of silicon, for example, where both the macro- and microsegregation behaviors are substantially different [7] (radial segregation is more pronounced, rotational effects are noticeable, and the dopant concentration changes associated with microsegregation are decreased by about one order of magnitude). The differences in segregation are attributed (a) to the relatively lower themal diffusivity of solid GaAs, (b) to minimized temperature gradients in the growing GaAs crystal, and (c) to the crystal pulling rate which is less by about one order of magnitude in GaAs. Under these conditions, accumulation of dopants at the phase boundary will be small and any fluctuations in the melt flow velocity as well as variations in the positive rate of growth at frequencies in the range from 0.1 to about 10 Hz can only have a minor effect on segregation. Both phenomena can lead to the formation of conventional

non-rotational striations (fig. 7a) [14]; neither can account for the striations with massive dopant concentration depressions observed in fig. 3 which approach two orders of magnitude.

Dopant striations which on chemical etching yield "pronounced contrast" in interference microscopy are common in crystals grown by the Czochralski and Bridgman techniques. They have been studied in silicon and germanium and were identifed as remelt striations. Their formation could be attributed to local melt-back associated with rotational pulling in a thermally asymmetric environment as well as to pronounced temporal thermal perturbations at the growth interface [7,8]. The composition profiles of such remelt striations could as yet not be determined in detail, primarily because of the limited resolution provided by the available analytical techniques such as spreading resistance measurements. Existing data for germanium suggest that they reflect abrupt, local dopant concentration decreases of up to about 50% followed by a rapid recovery toward the average concentration level. This particular composition profile is attributed to the fact that regrowth following back melting proceeds with the bulk melt composition, c_L, extending at the onset to the actual growth interface. The resulting dopant concentration minimum, $c_{s(min)}$, can thus be approximated by $c_L k_o$.

During LEC growth of GaAs any thermal perturbations, convectively carried toward the growth interface, will remain virtually unattenuated since the prevailing thermal gradients are small, as is the thermal diffusivity of solid GaAs. Under these sluggish heat transfer conditions, positive temperature excursions are expected to result in substantive melt-back. The melt formed by the receding solid will assume a composition c_L^*, given by c_s (the concentration of the melting solid) corrected for the density change associated with the phase transformation (fig. 7c). Subsequent initial regrowth will lead to a local dopant concentration minimum, $c_{s(min)}$, given at the limit by $c_L^* \cdot k_o$, which can account for the full spectrum of observed concentration fluctuations. Since during continuing regrowth the melt composition at the growth interface is subject to rapid change brought about by segregat diffusive equilibration, and convective melt flows, the dopant incorporation at that stage will be strongly affected by the prevailing thermal boundary conditions. With major growth rate accelerations unlikely to occur under the given conditions, the dopant concentration increase to its average level, i.e. the dopant accumulation at the growth interface, should be gradual. Remelt striations in LEC GaAs are thus expected to be associated with an abrupt dopant concentration decrease and a more gradual recovery to its average level.

Sensitivity of microsegregation to the prevailing thermal boundary conditions, as discussed above, can account for the apparent differences in the composition profile of remelt striations in GaAs and Si. During growth of silicon, prevailing thermal gradients are significantly larger than during growth of GaAs; similarly, the thermal diffusivity of Si is larger. As a result, the thermal response of the growth interface to temperature perturbations is faster in Si. Heat waves carried to the interface in silicon or germanium

must be expected to be attenuated, the associated degree of melt-back smaller, and subsequent regrowth faster. The dopant segregation profiles of remelt striations in Si and Ge will appear narrower with the dopant concentration minima being virtually eliminated by diffusion (fig. 7b). The experimentally determined dopant concentration minima become a function of the resolving power of the analytical approach taken.

The high degree of compositional uniformity of LEC GaAs on a macroscale, the absence of rotational striations, and the insensitivity of the basic characteristics of dopant striations to radial position reflect the nature of prevailing convective melt flows and their interference with segregation. The melt flows in the growth interface region are temporally and spatially varying and associated with temperature excursions which are responsible for localized backmelting/regrowth and, thus, for the formation of randomly space, discontinuous striations. The geometric pattern of melt flows is such that it provides for boundary conditions at the growth interface which lead to independence of microsegregation from radial position as well as from the rate of seed and crucible rotation.

Conclusions

NIR transmission microscopy combined with computational image analysis provides a means for quantitative microsegregation analysis with high sensitivity and spatial resolution. Using this approach it is found that conventional, doped LEC GaAs grown in the <100> direction, while exhibiting only a small radial segregation effect (fig. 4) on a macroscale, experiences unexpectedly large compositional non-uniformity on a microscale which is about one order of magnitude larger than anticipated and reported to exist in Si and Ge (fig. 8). The radial and axial composition profiles of a 75 mm crystal indicate that when the material is used in wafer form for device fabrication (fig. 9) the free charge carrier concentration within and normal to the (100) surface of the wafer will vary by factors of up to about 50 over distances of 1 cm and 10 μm respectively. The formation of these inhomogeneities in carrier distribution, striations of the remelt type, is attributed to interference by turbulent melt convection with dopant incorporation during growth. Carrier fluctuations of the observed magnitude, considered to be inherent to commercial, doped LEC GaAs, do affect its physical properties. They are expected to be of concern in device processing, in particular when substrates are used as active device matrices. In this context, it is of interest to re-examine the rationale behind customary property specifications which establish, for example, the limits of acceptable radial segregation as ranging from 10 to 15%.

References

1. R.L. Roedel, A.R. Von Neida, D. Caruso, and L.R. Dawson, J. Electrochem. Soc. **126** (1979) 637; T. Honda, Y. Ishii, S. Miyazawa, H. Yamazaki, and Y. Nanishi, Jpn. J. Appl. Phys. **22** (1983) L270 .

2. See for example: E.S. Meieran, J. Appl. Phys. **36** (1965) 2544; R.N. Thomas, H.M. Hobgood, G.W. Eldridge, D.L. Barrett, T.T. Braggins, L.B. Ta, and S.K. Wang, in: Semiconductors and Semimetals, Vol. 20 (Academic Press, NY, 1984) p. 1.

3. W. Walukiewicz, J. Lagowski, L. Jastrzebski, M. Lichtensteiger, and H.C. Gatos, J. Appl. Phys. **50** (1979) 899.

4. L. Jastrzebski, J. Lagowski, W. Walukiewicz, and H.C. Gatos, J. Appl. Phys. **51** (1980) 2301.

5. D.J. Carlson and A.F. Witt, J. Crystal Growth **91** (1988) 239.

6. W.G. Spitzer and J.M. Whelan, Phys. Rev. **114** (1959) 59 .

7. See for example: A. Murgai, H.C. Gatos, and A.F. Witt, in: Semiconductor Silicon 1977, Eds. H.R. Huff and E. Sirtl (Electrochemical Society, 1977) p. 72; K.H. Yao and A.F. Witt, J. Crystal Growth **80** (1987) 453 ; J.R. Carruthers, A.F. Witt, and R.E. Reusser, "Czochralski Growth of Large Diameter Silicon Crystals – Convection and Segregation" in: Semiconductor Silicon 1977, Eds. H.R. Huff and E. Sirtl (Electrochem. Soc., Princeton, NJ, 1977) p. 61; K.S. Choe and T.H. Strudwick, J. Crystal Growth **74** (1986) 338.

8. See for example: E.P. Martin, A.F. Witt, and J.R. Carruthers, J. Electrochem. Soc. **126** (1979) 284; A.F. Witt, M. Lichtensteiger, and H.C. Gatos, J. Electrochem. Soc. **121** (1974) 787; A.F. Witt, M. Lichtensteiger, and H.C. Gatos, J. Electrochem. Soc. **120** (1973) 1119.

9. See for example: K. Morizane, A.F. Witt, and H.C. Gatos, J. Electrochem. Soc. **113** (1966) 51; A.F. Witt and H.C. Gatos, J. Electrochem. Soc. **113** (1966) 808; A.F. Witt and H.C. Gatos, J. Electrochem. Soc. **115** (1968) 70.

10. See for example: R.N. Thomas, H.M. Hobgood, G.W. Eldridge, D.L. Barrett, T.T. Braggins, L.B. Ta, and S.K. Wang, in: Semiconductors and Semimetals, Vol. 20 (Academic Press, NY, 1984) p. 1.

11. H.A. Walls and W.R. Upthegrove, Acta, Metall. **12** (1964) 461.

12. See: J.M. Whelan, J.D. Struthers, and J.A. Ditzenberger, in: Properties of Elemental and Compound Semiconductors, Vol. 5 (Interscience, 1960) p. 275; L.R. Weisber, F.D. Rosi, and D.G. Horkort, Properties of Elemental and Compound Semiconductors, Vol. 5 (Interscience, 1960) p. 25; L.J. Vieland, J. Appl. Phys. **33** (1962) 2007; P.D. Green, J. Crystal Growth **50** (1980) 612; and J.C. Brice, Growth of Crystals from Liquids (North Holland, Amsterdam, 1972) Chapter 2.

13. J.C. Brice in: Atomic Diffusion in Semiconductors, Ed. D. Shaw (Plenum, NY, 1973) 112.

14. J.R. Carruthers and A.F. Witt, "Transient Segregation Effects in Czochralski Growth" in: Crystal Growth and Characterization, Eds. R. Ueda and J.B. Mullin (North-Holland Publishing Co., 1975) p. 107.

Figure Captions

Fig. 1 Near Infrared transmission imaging and analysis system

Fig. 2 NIR transmission micrograph of Si-doped GaAs (double-sided, polished segment of 0.7 mm thickness cut parallel to the growth axis) grown by conventional HP-LEC pulling. The free charge carrier distribution of region A is quantitatively analyzed in fig. 3.

Fig. 3 Enlarged presentation of Si microsegregation (outlined in fig. 2) and corresponding quantitative free charge carrier analysis.

Fig. 4 Radial macrosegregation (measurement resolution 2 mm) of Si in GaAs; each data point constitutes the average concentration value over a distance of 500 μm normal to the plane investigated.

Fig. 5 Effect of measurement resolution on the result of a microsegregation analysis; (A) measurements taken at 2.5 μm intervals [left axis], (B) - (C) average values of 5 and 10 measurements spaced at 2.5 μm respectively [right axis].

Fig. 6 Three-dimensional presentation of typical impurity striations in conventional LEC GaAs.

Fig. 7 Schematic of the phenomena leading to the formation of conventional striations (a) and remelt striations in systems with fast (b) and slow (c) heat transfer characteristics (see text).

Fig. 8 Radial microsegregation (measurement resolution 2.5 μm) of Si in GaAs normal to the <100> growth direction. The data of the indicated linear array are the equivalent of a line scan on the surface of a (100) GaAs wafer cut from the crystal presently analyzed.

Fig. 9 Schematic of dopant non-uniformity in wafer geometry (see text).

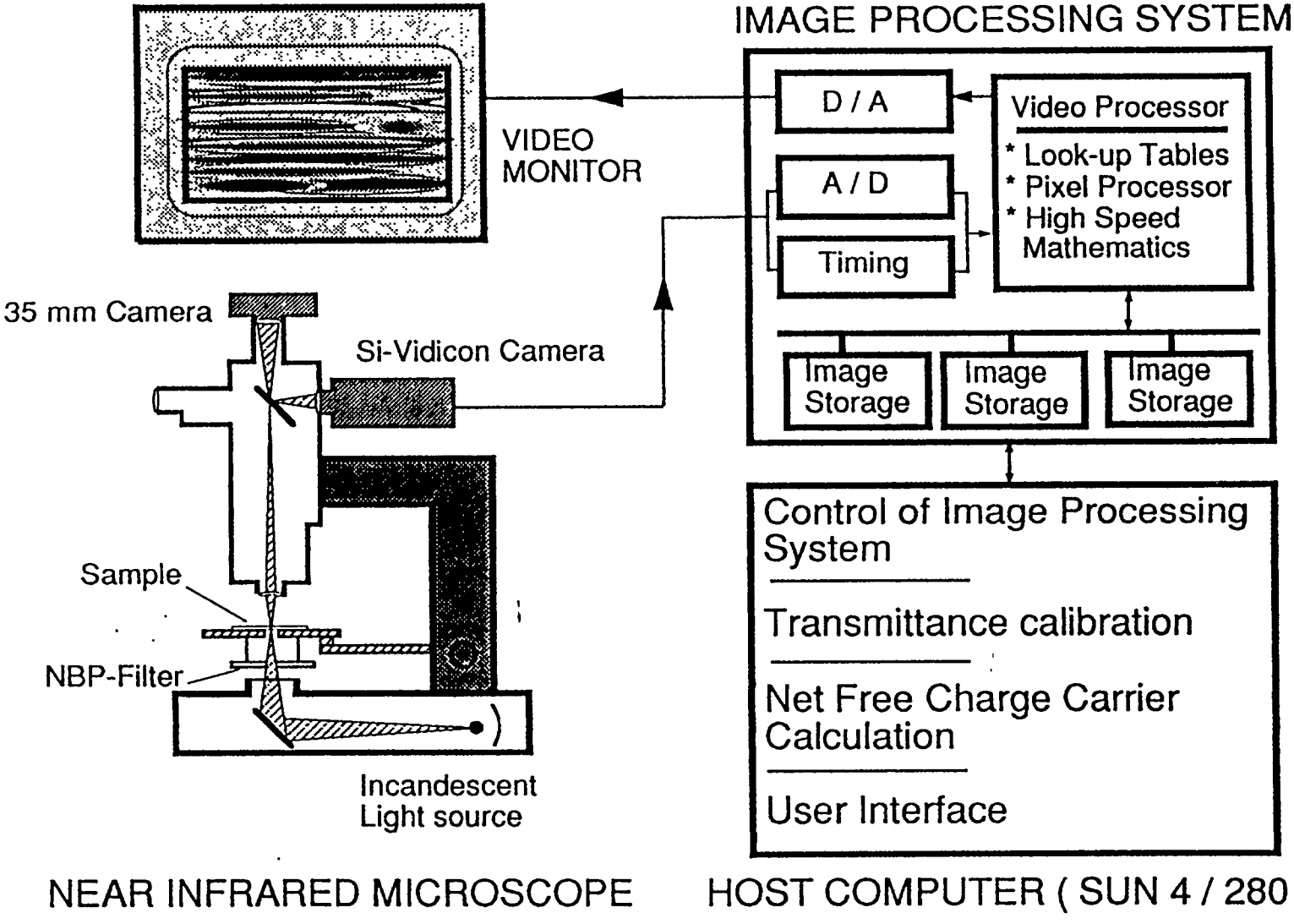
IMAGE PROCESSING SYSTEM
VIDEO MONITOR
D / A
A / D
Timing
Video Processor
* Look-up Tables
* Pixel Processor
* High Speed Mathematics
Image Storage
Image Storage
Image Storage
35 mm Camera
Si-Vidicon Camera
Sample
NBP-Filter
Incandescent Light source
Control of Image Processing System
Transmittance calibration
Net Free Charge Carrier Calculation
User Interface
NEAR INFRARED MICROSCOPE
HOST COMPUTER (SUN 4 / 280)

Fig. 1

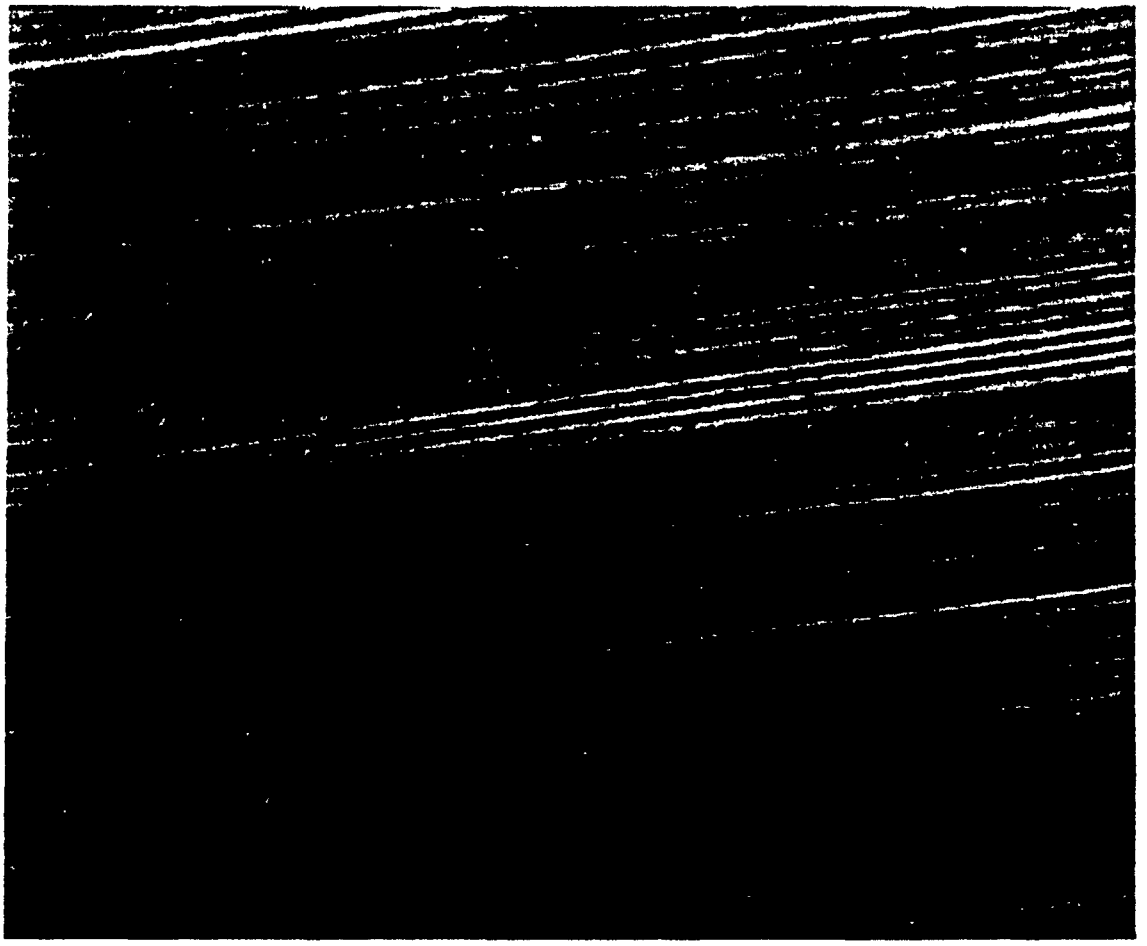

Fig. 2

1E18
n (cm⁻³)
1E17
R_S R_C
50 μm

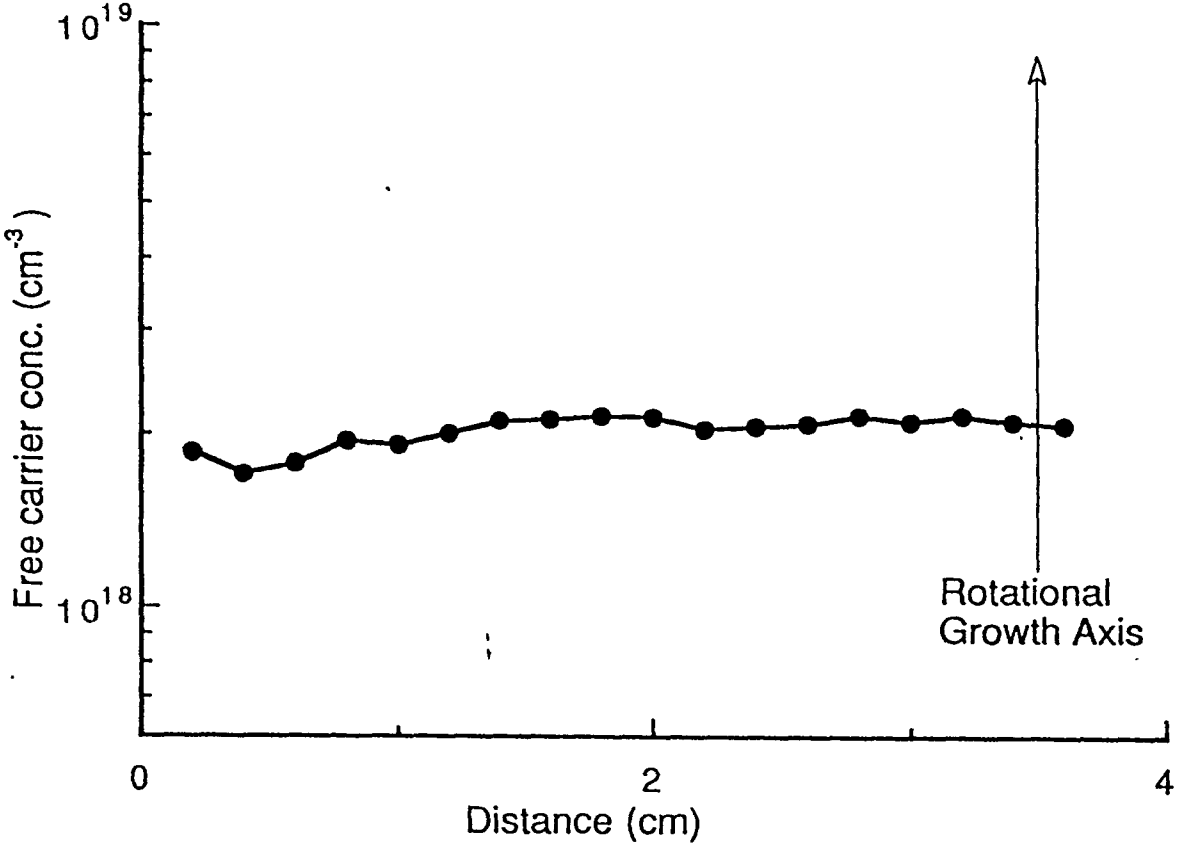
10^{19}
10^{18}
Free carrier conc. (cm^{-3})
Rotational
Growth Axis
0
2
4
Distance (cm)

Fig. 4

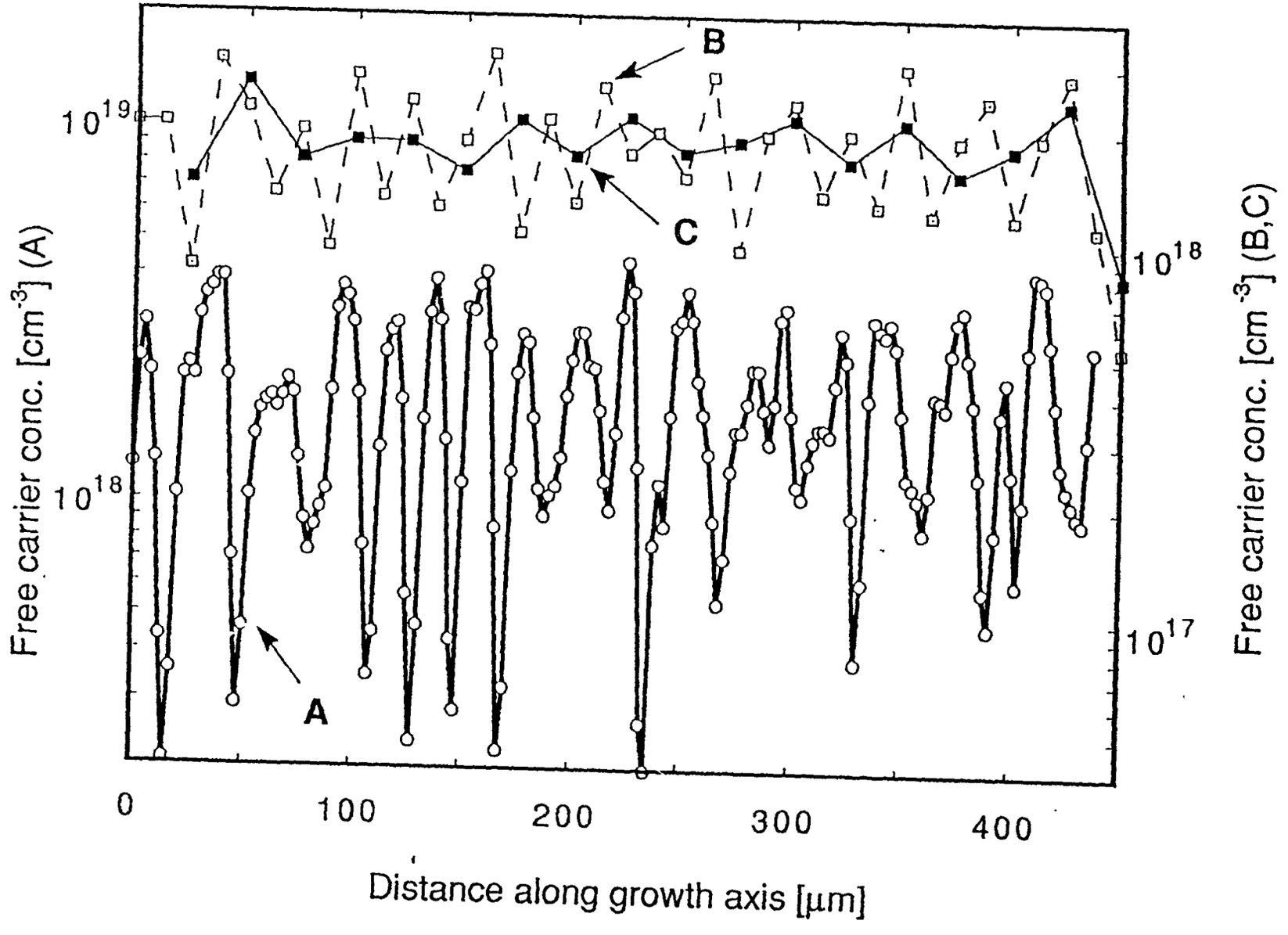
B
C
A
10^{19}
10^{18}
10^{18}
10^{17}
Free carrier conc. [cm^{-3}] (A)
Free carrier conc. [cm^{-3}] (B,C)
0
100
200
300
400
Distance along growth axis [μm]

Fig. 5

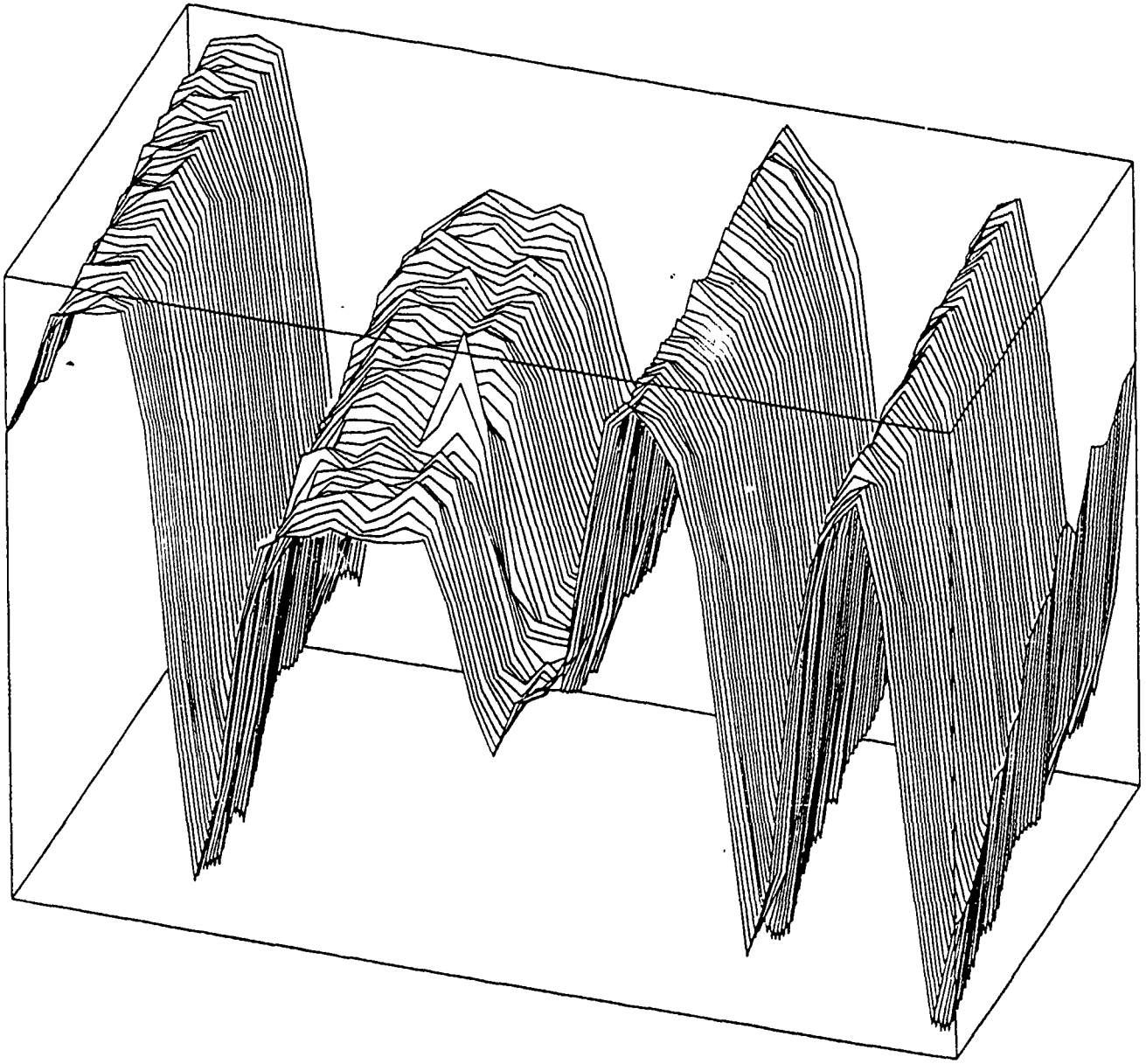

Fig. 6

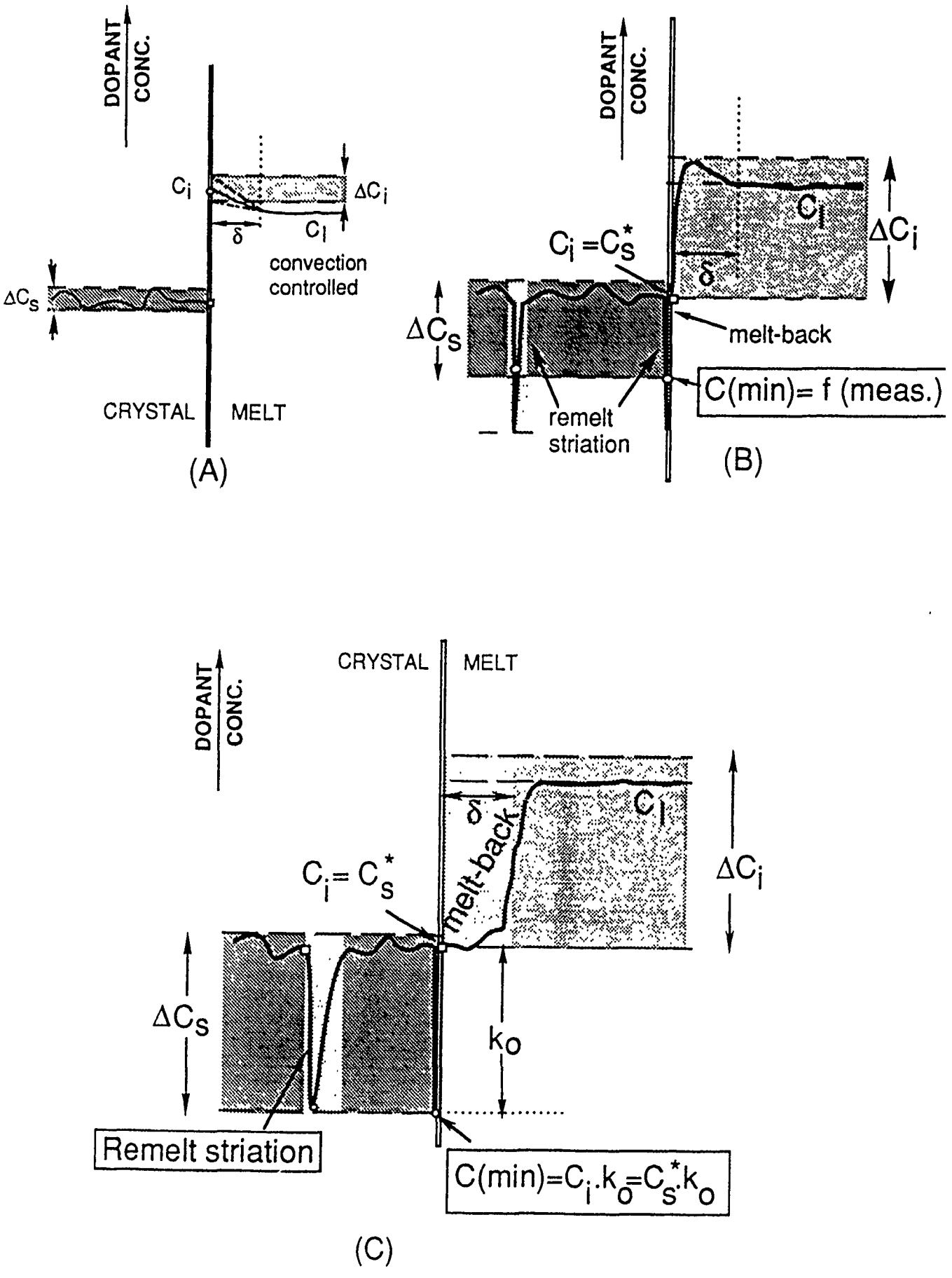
DOPANT CONC.
C_i
ΔC_i
C_l
δ
convection controlled
ΔC_s
CRYSTAL
MELT
(A)
DOPANT CONC.
$C_i = C_s^*$
C_l
ΔC_i
δ
ΔC_s
melt-back
C(min)= f (meas.)
remelt striation
(B)
CRYSTAL
MELT
DOPANT CONC.
δ
melt-back
C_l
ΔC_i
$C_i = C_s^*$
ΔC_s
k_o
Remelt striation
$C(min)=C_i.k_o=C_s^*.k_o$
(C)

Fig. 7

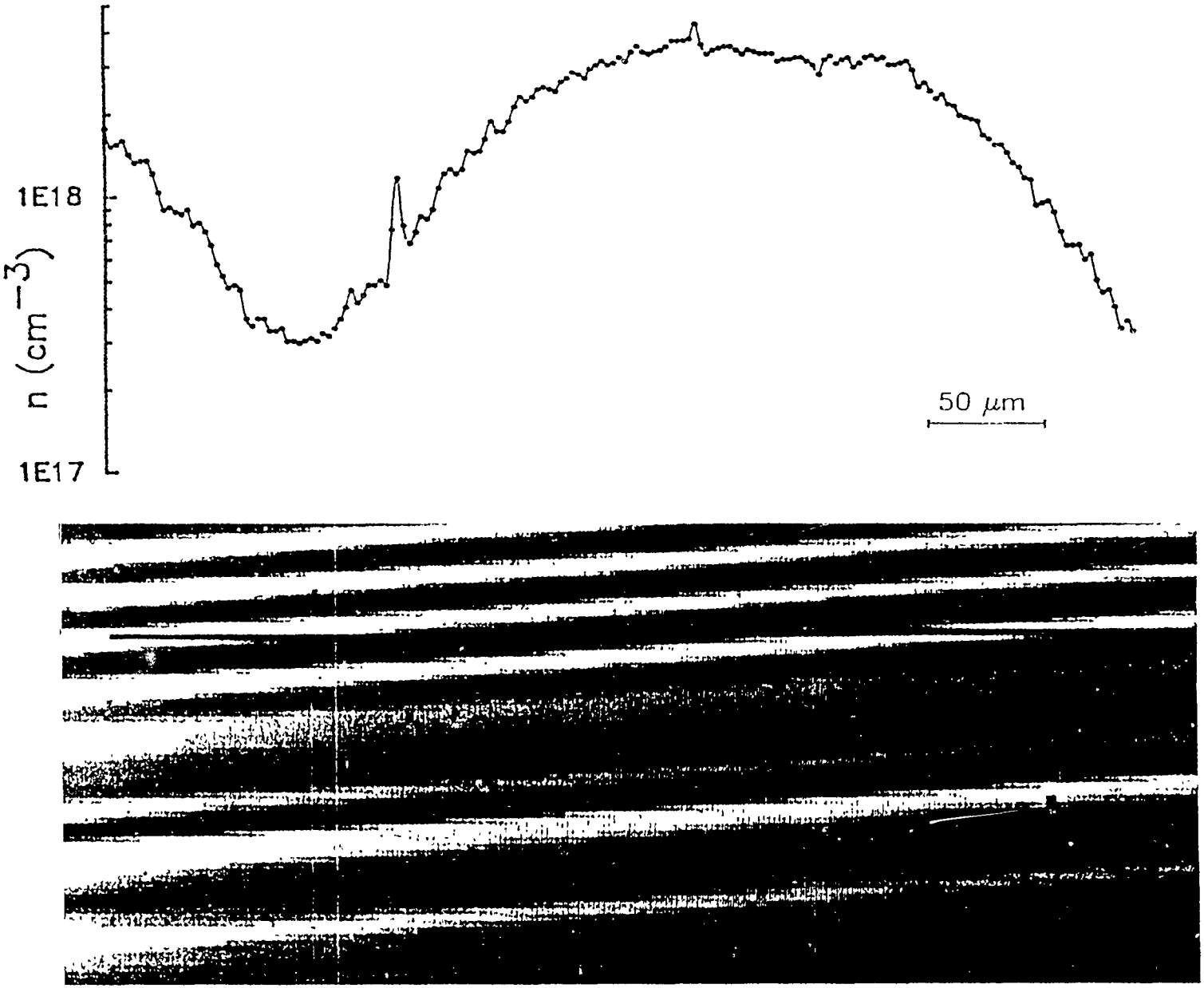
1E18
n (cm^{-3})
1E17
50 μm

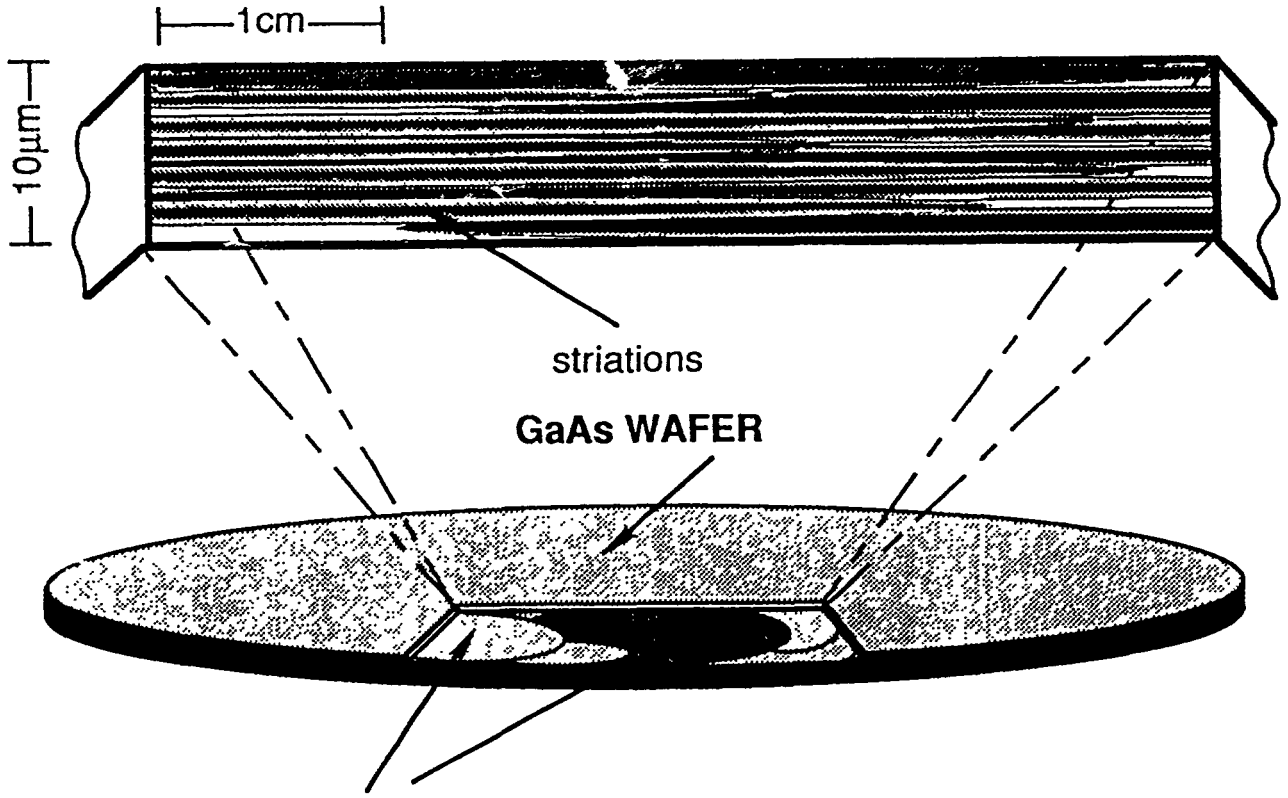

Lenticular remelt/regrowth regions generated by turbulent melt convection; these regions appear as striations of 5 to 20 mm in length and 2 to 20 µm thickness normal to the wafer surface.

Fig. 9

TABLE 1

Experimentally determined constants (a) and (b) in correlation between free carrier concentration (n) and the optical absorption coefficient (α); see [2].

λ (μm)	a	b	Correlation Coefficient
1.00	0.282	4.29	0.99
1.05	0.322	5.04	0.99
1.10	0.395	5.58	0.99
1.50	0.669	10.61	0.98
1.80	0.669	11.40	0.98

QUANTITATIVE ANALYSIS OF THE EFFECTS OF VERTICAL MAGNETIC FIELDS ON MICROSEGREGATION IN Te-DOPED LEC GaAs

Introduction

Uncontrolled thermal convection in the melt is the major cause of microscale composition inhomogeneities in Czochralski grown semiconductor single crystals. It has been shown to affect dopant segregation through temporal and spatial variations of melt flow velocity (resulting in fluctuations of the solute boundary layer thickness) and temperature (resulting in fluctuations of the microscopic growth rate). Most recently convection induced variations of the free charge carrier concentration in conventionally grown, silicon-doped LEC GaAs are found to reach values in excess of one order of magnitude over distances of less than 10 μm. Segregation inhomogeneities of the indicated origin, spanning from microscopic to macroscopic dimensions, lead to significant property degradation and thus affect adversely the yield and performance of a multitude of fabricated devices.

Control of the level of convection in Czochralski systems has traditionally been approached through modification of thermal boundary conditions by heaters and reflectors. Only recently has attention been directed at magnetic melt stabilization. Transverse magnetic fields applied during the growth of InSb were reported to lead to (1) a decrease in the amplitude of temperature fluctuations in the melt; (2) an increase in the complexity of the radial temperature field; and (3) an increase in rotation related microsegregation. These results were interpreted as indicative for a decrease of the level of convection in the system and for a related increase in both the thickness of the momentum and solute boundary layers at the crystal/melt interface. Magnetic field application correspondingly was expected to lead to a reduction of convection induced microsegregation and to an increased sensitivity of dopant incorporation to system related growth rate variations.

The effects of both axial and vertical magnetic fields during LEC growth of GaAs and InP have been investigated and interpreted as indicative for damping of convective melt flows from the turbulent to the laminar regime. Consistent with this interpretation it is reported that on application of axial magnetic fields the effective segregation coefficients of dopants approach the value of one. Because of the non-availability of analytical techniques with adequate sensitivity and resolution, the reported microsegregation studies of magnetically stabilized LEC GaAs have by necessity been only qualitative in nature. They have been based primarily on differential etching of sample surfaces and on interpretations of X-ray topographs. Thus increases in the periodicity of striae as well as greater uniformity of their amplitude has been reported in most studies. It was further reported that, according to etching results, striae decreased in intensity from the crystal periphery to the center. These largely qualitative findings have been interpreted phenomenologically in terms of the Burton, Prim and Slichter

(BPS) theory:

$$k_{eff} = \frac{k_0}{k_0 + (1 - k_0)\exp^{-\left[\frac{\delta R}{D}\right]}}$$

where the solute boundary layer thickness, δ, is given by the Cochran analysis:

$$\delta = 1.6\, D^{1/3}\, \nu^{1/6}\, \omega^{-1/2}$$

Within this theoretical framework, the changes in segregation coefficient observed upon application of vertical magnetic fields appear consistent with the proposed increase in the solute boundary layer thickness due to an increase in the "effective" viscosity of the melt.

The qualitative nature of the existing data base on segregation during growth from magnetically stabilized melts has so far precluded a reliable interpretation of stabilization effects. Microsegregation can in principle be expected to be influenced by magnetic field strength and direction, crystal and crucible rotation, as well as by the thermal geometry of the growth system; in the absence of quantifiable boundary conditions it is impossible, however, to predict a priori whether the growth rate, the solute boundary layer thickness, or another mechanism dominates. The strategy for the elimination of compositional inhomogeneities has therefore remained a largely empirical task.

The ongoing work is directed at advancing our understanding of crystal growth and segregation in the presence and absence of magnetic fields through quantitative segregation analyses with a spatial resolution of better than 2 μm. This is accomplished with computational image processing of NIR transmission micrographs which upon calibration provides for quantitative free charge carrier analyses. Primary focus is placed on the elucidation of segregation phenomena associated with axial magnetic fields applied under conditions of seed and crucible rotation similar to those used in conventional growth.

Experimental Approach

Te-doped GaAs crystals, 2 to 3 inches in diameter, were grown in a Hamco CG-700 system by low pressure LEC pulling (1.3 cm/h) from 3 kg melts in 6-inch diameter fused silica crucibles subjected to axial magnetic fields ranging from 1000 to 3000 gauss (fig. 1). In all growth experiments, the charge was prepared from undoped semi-insulating polycrystalline GaAs by addition of dopant to achieve an initial Te concentration (C_0) of $5.5 \times 10^{19}/cm^3$ in the melt.

For analysis, samples from the grown crystals were cut parallel to the growth direction so as to contain the rotational axis of the crystal on the sample surface. The

samples, 1-2 mm thick, were lapped and polished on their front and back surfaces for near infrared (NIR) transmission analysis.

The microdistribution of tellurium was quantitatively determined from near infrared transmission analyses as described earlier. The approach taken utilizes the dependence of the absorption coefficient of extrinsic, n-type GaAs on the net free carrier concentration to determine the Te concentration in GaAs from transmittance measurements. The measurements involve computational analysis of video images with a spatial resolution exceeding 2.5 μm.

The dopant profile of commercial Te-doped LP-LEC GaAs (peripheral segment cut along the <100> growth axis) was obtained with a resolution of about 2 μm from pixel to pixel transmittance measurements of an NIR transmission micrograph. It indicates aperiodic fluctuations in dopant concentration which in isolated locations approach two orders of magnitude; their characteristics are found to be the same in all regions of the crystal analyzed: they are devoid of rotational periodicity, appear discontinuous, and are of varying width.

Experimental Results

The crystal analyzed in this study, 2.5 inches in diameter, was pulled at a rate of 1.3 cm/h with seed and crucible rotation of 4 and -12 RPM respectively. The 3 kg charge was subjected during growth to an axial magnetic field of 2000 Gauss. In a preliminary investigation it was observed that the segregation behavior did not measurably change along the growth axis, but was subject to marked differences in the radial direction. Microsegregation at an arbitrary location along the growth axis was therefore studied in three critical radial positions: at 3 mm (Region I), 16 mm (Region II), and 22 mm (Region III) from the crystal perimeter.

An NIR transmission micrograph of Region I indicates the existence, at the crystal periphery, of highly periodic striations, delineating a moderately concave crystal-melt interface morphology. The average spacing of the striations is 67 μm, which corresponds within measurement error to the theoretical growth length per seed rotation corrected for melt depletion (66 μm). Characteristics of these peripheral striations are discernable at higher magnification on a defocused micrograph taken with the upper wafer surface positioned incrementally below the focal plane of the objective. This optical configuration, in suppressing details, is convenient for ascertaining the basic characteristics of striations and determining the corresponding compositional profiles. Accordingly, the dopant incorporation within the plane of observation is subject to continuous change during growth with the dopant concentration, at an average value of $4.4 \times 10^{18}/cm^3$, fluctuating from a minimum of $1.7 \times 10^{18}/cm^3$ to a maximum of $9 \times 10^{18}/cm^3$. Application of the axial magnetic field to the melt is thus recognized to result within the analyzed peripheral region in the suppression of aperiodic non-rotational striations and in the formation of periodic rotational striations with

compositional variations which approach one order of magnitude. Noticeable in these striations is the appearance of acute concentration maxima which are absent in all previously reported, conventional rotational striations (which are taken to be the result of growth rate variations).

By focusing the microscope onto the surface of the wafer, the substructure of the magnetically induced rotational striations is revealed. From the point of view of quantitative data interpretation it is important to note that the computed average dopant concentrations for focused and defocused imaging are found to be identical. In focused mode each striation is found to exhibit satellite striations, spaced in average at about 11 μm which is by a factor of two smaller than expected for direct correspondence with crucible rotation; the spacing of successive satellite striations varies slightly, with the maximum spacings coinciding with the concentration minima of the rotational striations. The compositional variations which constitute the satellites appear to be about one order of magnitude smaller than those associated with the rotational striations. In a series of related experiments it has been determined that upon arrest of seed rotation and under continuing growth with crucible rotation, all compositional fluctuations of large amplitude (rotational striations) cease while satellite formation continues. Under these pulling conditions, the spacing of satellite striations is found to increase over a growth length of 150 μm from 11 to 18 μm, thus approaching the value expected for direct correspondence with crucible rotation. The formation of satellite striations is found to cease at the boundary between Regions I and II and no striations related to crucible rotation can be observed in the crystal center, Region III.

The segregation behavior in Region II at about 16 mm from the crystal periphery reveals a lateral termination of the seed rotation related, periodic compositional fluctuations and the appearance of aperiodic striations. The microsegregation behavior is characterized by fluctuations in dopant concentration which are measurably smaller, but appear at average concentration levels which are significantly larger than encountered at the crystal periphery. In the central crystal region, near the transition from Region II to Region III, the average dopant concentration decreases abruptly to levels significantly below that at the crystal periphery. Simultaneously the degree in periodicity and the amplitude of compositional fluctuations increases. The average period of fluctuations at the crystal center corresponds closely to that expected from seed rotation.

The radial variations of axial microsegregation observed in this crystal grown from a magnetically stabilized melt suggest the existence of radial macrosegregation which in magnitude exceeds substantially that encountered in crystals grown by conventional LEC pulling. Radial composition profiles for crystals grown under the same conditions as those used on the material analyzed in the preceding show a steady decrease in dopant concentration from the crystal periphery inwards; at about mid-radius position the dopant concentration increases again over a short distance and subsequently decreases toward

the axis of seed rotation. Analyses at radially different axial planes confirm a high degree of radial symmetry in dopant segregation.

Discussion

The quantitative data base on dopant segregation for growth from magnetically stabilized melts is as yet limited as is our comprehension of the rate controlling processes for dopant incorporation. Established is that axial magnetic fields in excess of about 1 kGauss, when applied to Czochralski crystal growth of semiconductors, will attenuate turbulent convective melt flows and result in their transition to the laminar regime. Supporting evidence to that effect, in the form of temperature recordings, has been presented in the literature, primarily on doped silicon. From etching studies it has also been concluded that dopant incorporation during growth from such stabilized melts will proceed in a classical mode, i.e. in the absence of turbulence, at decreased and stabilized melt flow velocity, the solute boundary thickness is increased which entails enhanced growth rate dependence of the effective dopant distribution coefficient. Growth by rotational pulling from melts with asymmetric thermal environment can accordingly be expected to exhibit pronounced rotational striations which attenuate in the direction of the rotational pulling axis; the average dopant concentration level is likely increased and radial macrosegregation is essentially as encountered in conventional systems.

The quantitative composition analyses obtained in this study fail in many respects to support the contention of a predominantly growth rate controlled micro- and radial macrosegregation behavior.

Particularly the complexity of microsegregation in the peripheral crystal region is irreconcilable with pure growth rate effects. Inconsistent with the proposed interpretation is also the appearance of acute dopant concentration maxima in rotational striations, their termination in Region II as well as the reappearance of periodic rotational striations at the crystal center region. Unexplainable in context is, moreover, the formation of satellite striations, their frequency and spatial distribution. (In an effort to clarify correlations between the characteristics of rotational striations and thermal asymmetry, the carbon susceptor about the quartz crucible containing the melt was intentionally made thermally asymmetric. There was no measurable effect on the characteristics of the rotational striations.)

The preceding analysis reveals micro- and macrosegregation effects which are in apparent conflict with the BPS theory in its conventional form and cast doubt on the applicability of the Cochran analysis. It appears nevertheless of interest to analyze the compositional profile of a rotational striation on the basis of the BPS theory. For the purpose of this analysis, it is assumed that the average composition across the striations corresponds to the averaged macroscopic growth rate of 4.4×10^{-4} cm/s (pulling rate corrected for melt depletion). Taking the k_o value for Te in GaAs to be 0.06 and the diffusion constant (D) at 10^{-4} cm^2/s, then the solute boundary layer thickness (δ) is

computed as 0.184 cm. Using this value for δ in an iterative approach, the growth rate diagram corresponding to the formation of the concentration profile was determined. In this calculation the value of k_o was adjusted so as to force the time integrated growth to be consistent with that of one rotational period. In an analog manner the boundary layer thickness variations required to produce the observed composition profile were computed. The analysis shows that at the increased boundary layer thickness established with magnetic melt stabilization, compositional variations of the magnitude encountered in rotational striations can be readily generated by both growth rate and boundary layer thickness variations considered reasonable in growth systems. This conclusion appears valid even if, more realistically, transient segregation behavior is taken into account.

In the absence of quantitative growth rate data (obtainable through growth interface demarcation), the origin of the observed microscopic and radial macroscopic composition profiles cannot be unambiguously identified. However, the evidence, particularly radial segregation, points strongly toward fluid dynamics as the primary segregation controlling effect. This conclusion is reinforced by an analysis of the NIR transmission macrograph of a GaAs wafer from one of the crystals grown in this study. The intensity distribution provides a two-dimensional presentation of radial dopant segregation. The observed pattern appears indicative for the coexistence of two axially symmetric toroidal melt flow regimes prevailing at the central (Region III) and peripheral (Region I) parts of the crystal. The boundary between the two flow regimes at the growth interface (Region II) is thus characterized by a pronounced increase in the boundary layer thickness. Figure 2 is a schematic of the proposed flow regimes that is consistent with the observed radial segregation effects. Accordingly, melt flow in the peripheral region (I) is subject to oscillatory flow instabilities which are linked to both seed and crucible rotation; the instabilities affect dopant segregation through temporal modulations of the boundary layer thickness. Melt flow in the central region (III) is expected to be of higher velocity and existing instabilities appear linked to seed rotation, but not to crucible rotation. Correspondingly, the average dopant concentration level is lower than in the peripheral region and rotational striations, devoid of helical geometry, are continuous across this region and exhibit a periodicity which is related to seed rotation. Segregation in the region of stagnation (II) between the flow regimes is expected to reflect flow instability as well as an increased and varying solute boundary layer thickness.

In light of analytical data provided in this study, it is concluded that micro- and macrosegregation during growth from melts stabilized by axial magnetic fields is quantifiable on the basis of the BPS theory; however, the applicability of the Cochran analysis is not given. The fundamental difference in dopant incorporation during conventional and magnetically stabilized growth relates to the nature of the controlling parameter. In conventional growth, characterized by turbulent convective melt flows, the solute boundary layer is shallow and microsegregation appears largely controlled by melt back phenomena and growth rate fluctuations. During magnetically stabilized growth,

segregation appears controlled by bulk melt flows and the related characteristics of the solute boundary layer. The strategy for the reduction of radial segregation and the elimination of microsegregation must on the basis of the present findings be sought through manipulation of the fluid dynamics of growth systems.

Conclusions

Near infrared transmission analysis has provided a means for the analysis of micro- and macro- segregation in magnetically stabilized LEC GaAs. It is found that under conditions of counter rotation of the seed and crucible a symmetric radial macrosegregation pattern is obtained which suggest that the segregation phenomena is dominated by configuration of the solute boundary layer and bulk fluid motion. Axial microsegregation, while found to be highly periodic and of uniform amplitude at the crystal periphery is not the result of rotation in a thermally asymmetric thermal field. The radial variation of the axial microsegregation supports the interpretation of that the the segregation process is dominated by effects of forced convection in the presence of the axial magnetic field.

Figure Captions

Fig. 1 Experimental set-up for low pressure LEC growth of GaAs with applied axial magnetic field.

Fig. 2 Proposed melt flow pattern in magnetically stabilized melt. The indicated boundary layer characteristics are consistent with the observed segregation behavior.

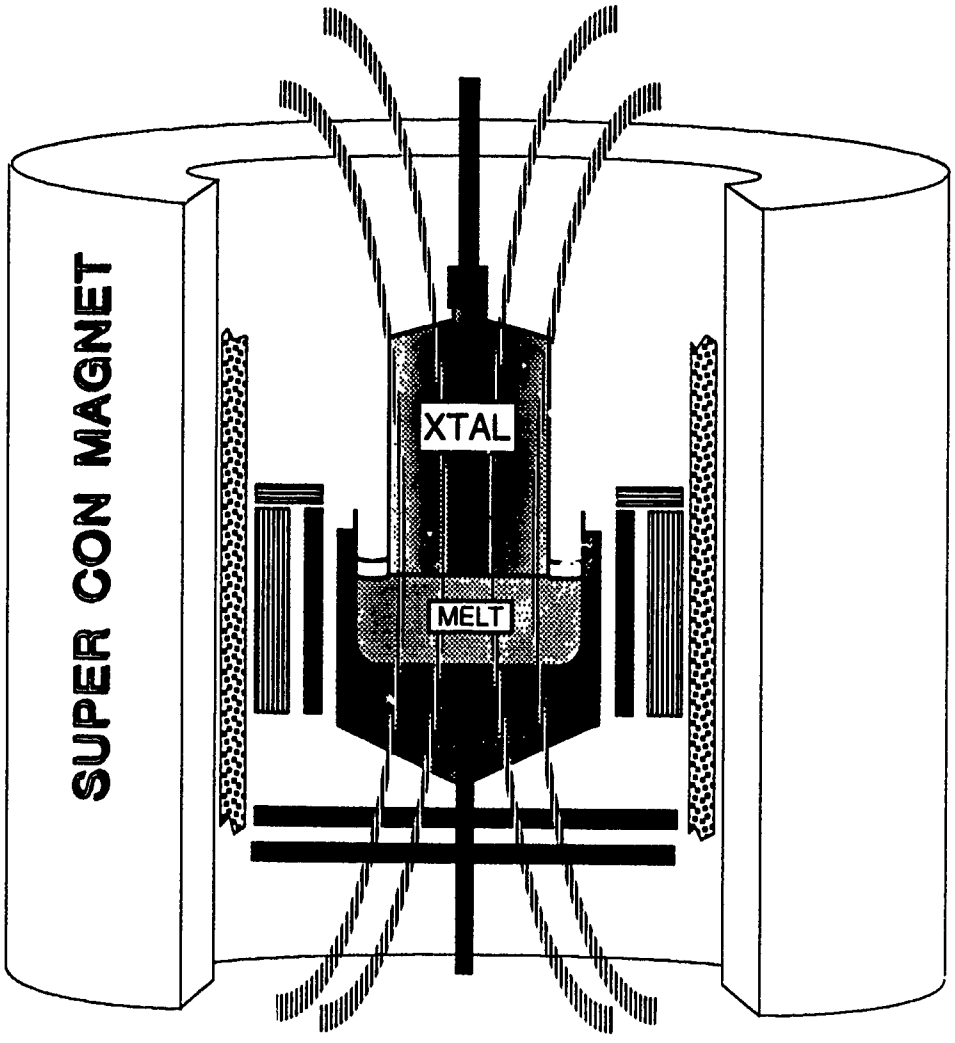

Fig. 1

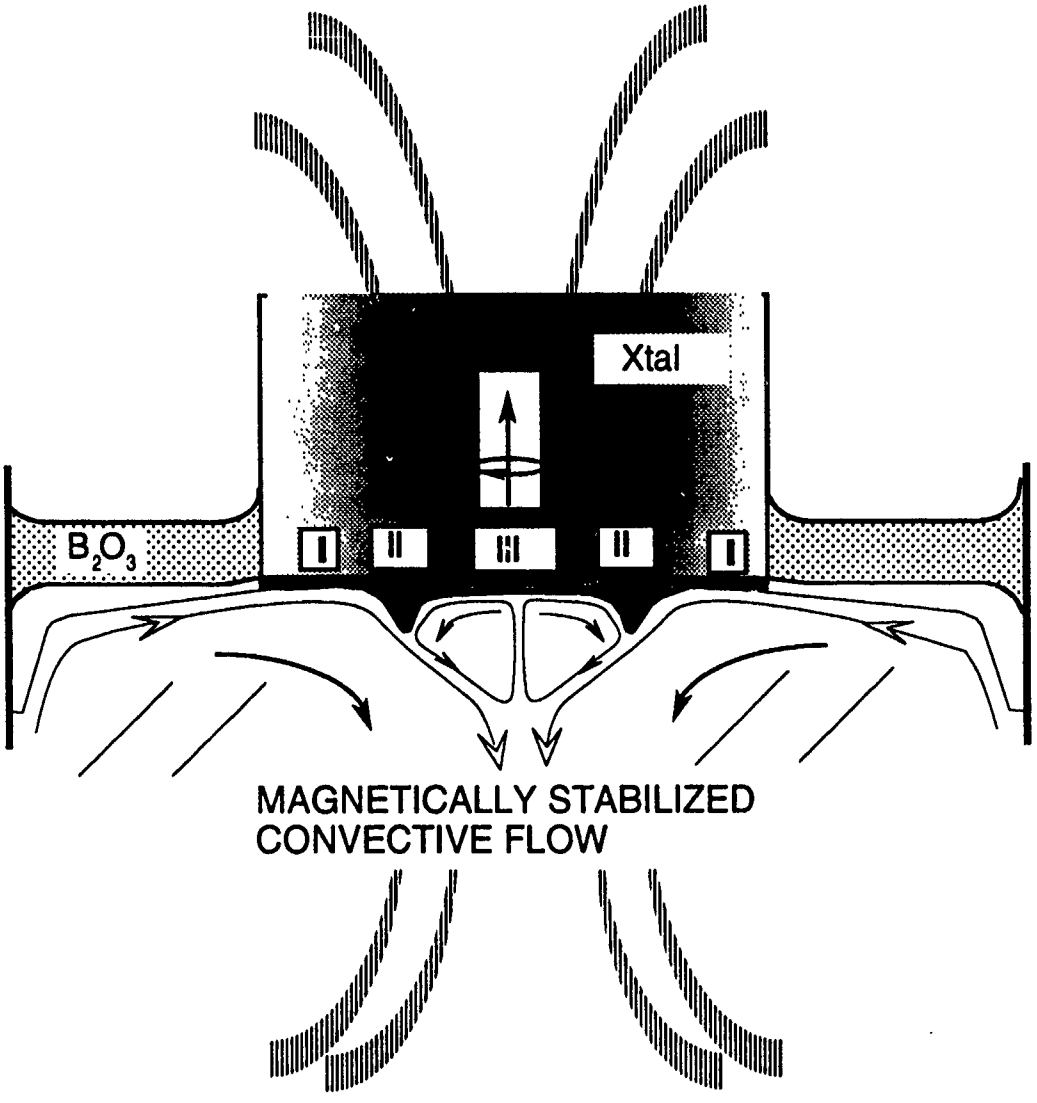
Xtal
B_2O_3
I
II
III
II
I
MAGNETICALLY STABILIZED
CONVECTIVE FLOW

Fig. 2

DECORATED DISLOCATIONS IN SI-GaAs AS REVEALED BY DARK FIELD NIR TRANSMISSION MICROSCOPY

The use of bright field NIR transmission microscopy in conventional and phase contrast mode is an effective approach to the study of growth striations [1], dislocations [2] and the quantitative determination of charge carrier distribution [3] in doped GaAs. When applied to semi-insulating GaAs wafers, however, bright field transmission microscopy fails to reveal any defect structures; the matrices appear transparent, reflecting the absence of defects within its resolving power. Detection of precipitates and decroated dislocations in semi-insulating matrices of Si, GaAs and InP [4,5] has more recently been made possible with Laser Scanning Tomography (LST) developed by Ogawa and coworkers [6]. This technique, based on light scattering, is extremely useful as it extends the applicability of NIR microscopy deep into the submicron regime. Its drawback is the complexity of hardware and the inherently destructive nature of the approach.

This note reports results on the application of dark field NIR transmission microscopy to the study of dislocations in semi-insulating GaAs. Undoped, double-sided, polished SI-GaAs wafers ranging in thickness from 300 μm to 1 mm were investigated using a Zeiss Axioplan microscope in transmission mode (fig. 1). A 10 Watt quartz iodine lamp functioned as IR light source; dark field illumination was achieved with a conventional dark field substage condensor (see insert). The radiation emanating from scattering centers in the sample is focused onto the vidicon detector plane (an extended red vidicon tube with a cut-off wavelength of 1.2 μm); gain and black level offset could be adjusted optionally with the camera control or the computational image analysis systems. The images were digitized, processed, back converted and displayed in real time on the monitor.

Figure 2 is a dark field transmission micrograph of commercial undoped <100> SI-GaAs. It reveals a high density of micro-precipitates which reflect the cellular structure of dislocation networks. The association of the scattering centers (particles of submicron dimensions below the detection limit for bright field illumination) with dislocations is evident in a wafer region of lower particle density viewed at higher magnification (fig. 3). The nature of the defects and their dependence on processing conditions is subject of an ongoing investigation.

The demonstrated approach to defect analysis, involving detection of scattering centers of submicron dimensions [7], is characterized by effectiveness, simplicity, and speed.

References

1. M.R. Brozel, in Defect Recognition and Image Processing in III-V Compounds, Ed. E.R. Weber (Elsevier, Amsterdam, 1987) p. 225.
2. S. Clark, M.R. Brozel and D.J. Stirland, in Defect Recognition and Image Processing in III-V Compounds, Ed. J.P. Fillard (Elsevier, Amsterdam, 1985) p. 201.
3. D.J. Carlson and A.F. Witt, J. Crystal Growth **91** (1988) 239.
4. Y. Otoki, M. Watanabe, T. Inada and S. Kuma, J. Crystal Growth **103** (1990) 85.
5. J.P. Fillard, P.C. Montgomery, P. Gall, M. Castagne and J. Bonnafe, J. Crystal Growth **103** (1990) 109.
6. K. Moriya and T. Ogawa, Jap. J. Appl. Phys. **22** (1983) L207.
7. J.P. Fillard, P.C. Montgomery, P. Gall, J. Bonnafe and M. Castagne, J. Crystal Growth **103** (1990) 120.

Figure Captions

Fig. 1 Schematic diagram of the computational image analysis systems. Encircled insert is the darkfield geometry used in this work. 1: objective lens. 2: specimen. 3: stage. 4: condenser lenses. 5: condenser aperture diaphragm with central stop. 6: incident beam. 7: direct transmitted beam. 8: scattered beam.

Fig. 2 Darkfield transmission IR micrograph of cellular structure with precipitates in an <100> undoped semi-insulating GaAs wafer.

Fig. 3 Darkfield transmission IR micrograph of decorated dislocations.

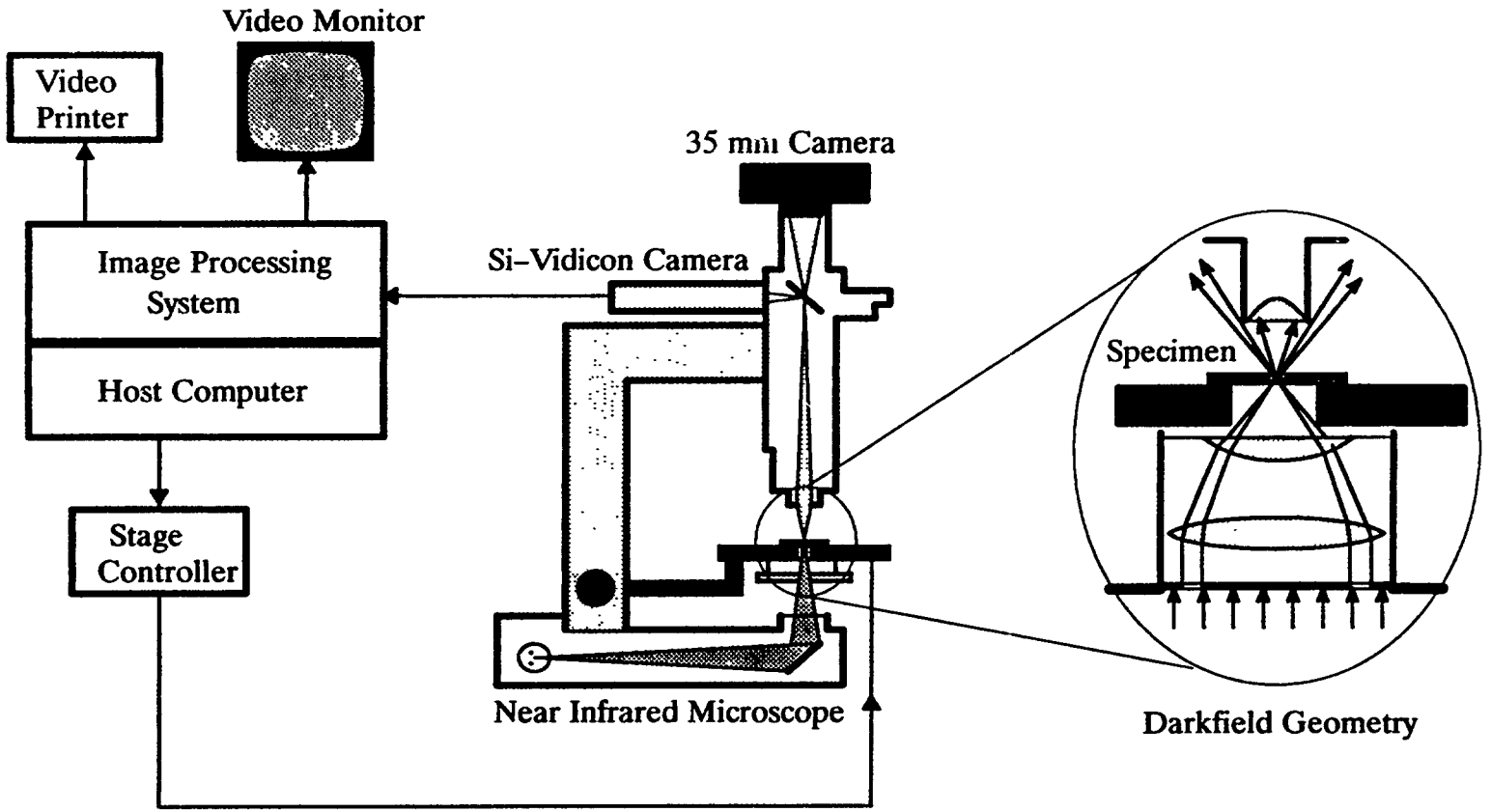
Video Monitor
Video Printer
35 mm Camera
Image Processing System
Si-Vidicon Camera
Host Computer
Stage Controller
Specimen
Near Infrared Microscope
Darkfield Geometry

Fig. 1

Fig. 2

Fig. 3

MODEL-BASED CONTROL OF THERMAL STRESSES DURING LEC GROWTH OF GaAs

Introduction

Model-based control of thermal stresses during Liquid Encapsulated Czochralski growth of GaAs is based on two elements: (a) accurate calculation of the temperature field in the crystal during growth and cool-down by a numerical model, and (b) introduction of a Heat Flux Control System (HFCS) into the growth furnace, installed co-axially around the crucible containing the charge, to provide for active control of the temperature distribution in the crystal. The accuracy of model predictions was experimentally established in ref.[1]. For example, it was shown that during advanced stages of growth, the accuracy of the calculated elastic thermal stresses was $\pm 0.2 \times$CRSS (critical resolved shear stress) of the matrix.

The present growth system provides, for the first time, for quantitative control of temperature field in the crystal during growth and cool-down. Thus, it is possible to unambiguously establish the relationship between the dislocation density of the grown crystal and its temperature and thermal stress history.

We begin by a brief discussion of the growth environment and the model-based stress control strategy. Three crystal growth experiments, the associated numerical simulation results, and the dislocation density distribution in these crystals are, then, presented.

Growth Configuration and Strategy

A schematic of the growth configuration is shown in Fig. 1, and fully described in refs. [1,2]. The crucible containing the charge is placed in a standard 20-cm diameter graphite furniture, and the HFCS (**2**) [1] is positioned co-axially around the crucible. The main heater (**6**) is used to bring the system up to growth temperature. During growth and cool-down, the heater ramp is controlled by the main control thermocouple (**7**) and monitored by a second thermocouple (**4**) placed close to the crucible graphite support (**10**). The temperature distribution along the inner wall of the HFCS is controlled by three independent heaters and four thermocouples located at various axial positions along the wall. The design details of the HFCS permit establishment of drastically different thermal environments for the growth process, ref. [1].

The thermal conditions required for maintaining stresses in the crystal at below the CRSS of the matrix are shown in ref. [1] to impose stringent conditions on the temperature distribution in the crystal. To achieve these conditions the HFCS was developed to provide for active control of the growth thermal environment. The growth trajectory of the HFCS temperature profile required for reduction of thermal stresses in the crystal is identified by accurate numerical modeling of the growth process, ref. [2,3].

There are, in principle, three ways to integrate numerical modeling and the growth

[1]The bold numbers in parentheses correspond to numbers in Fig. 1.

process, Fig. 2. The essential difference between the three is based on the approach to control the crystal diameter. In the first approach, diameter- and stress-control tasks are completely decoupled. Crystal diameter is controlled in feed-back mode using some observable attribute of the crystal geometry, such as its diameter or its weight, and controlling the power input into the main heater. If the diameter-control task can be achieved successfully, the required thermal environment conditions, associated with the desired stress distribution in the crystal, may be identified off-line and implemented during growth and cool-down (by controlling the axial thermal profile of the HFCS inner wall) in a feed-forward manner. In this configuration, the crystal diameter and pull rate are used as inputs into the numerical model, and the model and growth experiment are synchronized by a "time-clock." As the crystal geometry is a predictable function of time (because the diameter-control loop is performing satisfactorily), this synchronization of the model and the furnace ensures that, at all times, the model-based control instructions implemented in the HFCS correspond to the actual geometry of the growing crystal.

Achievement of constant diameter growth is, however, a difficult task, and some deviation of the crystal diameter from the desired shape may be expected. If this deviation is sufficiently large to perturb the thermal characteristics of the growth environment, then model predictions, based on the assumed crystal geometry, will differ from the temperature field present in the growth system. The difference between the actual and calculated temperature fields can be minimized by inputting the geometry of the growing crystal, as observed in the diameter-control loop, into the numerical model, Fig. 2(b). In this configuration, the model is used on-line, but the stress control procedure is still performed in the feed-forward manner.

The third approach involves use of numerical model to control the crystal diameter. Numerical models of the CZ and LEC processes provide, in principle, the thermal conditions necessary to achieve constant diameter growth through, for example, predicting the time-history of power input into the main heater, or that of its control thermocouple. Figure 2(c) corresponds to the situation where the numerical model is used to achieve diameter-control. Here, both diameter and stress control tasks are performed in the feed-forward mode.

Of the three approaches described above, the first is the control structure used in the present study. The long-term advantages of this approach over the other two are discussed in section 6. In the experiments reported here, diameter control was achieved by the operator through visual observation of the crystal shape.

Crystal Growth Experiments

Three crystal-growth experiments are reported. As described in ref. [1], total encapsulation of the crystals was adopted to minimize the potential error in the model predictions associated with the uncertainty in the value of emissivity of the unencapsulated portion of the crystal. The preparation details of the charge, the $< 100 >$ seeds, and the furnace, as well as the procedures for seeding and removal of the crystal from the encapsulant, were the same for all experiments and are described in detail in ref. [2]. All

three crystals were grown from a 1250-g charge using 600 g of B_2O_3 as the encapsulant. Growth was conducted at nominal pull rates of approx. 5 mm/hr, corresponding to growth rates of 8 mm/hr. The only intentional difference between the three experiments was the thermal environments (the axial temperature profiles of the HFCS) used during growth and cool-down of the crystals.

Before describing the experiments and their results, two growth-related issues are discussed: diameter control and crystal-melt separation.

Perfect diameter control was not achieved in the three grown crystals. Thus, the shape of the three crystals was not identical and differed from the assumed shapes used in the model to calculate the HFCS temperature profiles implemented during growth. The off-line calculations assumed a crystal diameter of 5.6 cm and a cone angle of 24°. The actual shapes of the crystal and the shapes used in the model calculations are shown in Fig. 3. Of the three crystals, the last shows the largest difference between the modeled and actual crystal shape. The calculations were repeated, after growth, for the third crystal with a constant diameter equal to its average diameter and actual length, Fig. 3(c). The correction to the calculated stress field in the crystal was not appreciable. It is, however, conceivable, that the diameter fluctuations in this crystal may lead to a difference between the actual and calculated temperature and stress histories in the crystal. Results presented here assume that this discrepancy is a second-order effect.

In the three experiments crystal-melt separation was achieved by increasing the power into the main heater approximately one hour before the anticipated separation. Optimum separation requires, in principle, gradual reduction of the solid-melt interface area similar to the growth of an inverted cone. Separation procedures that do not provide for this type of transition (i.e., when a finite growth interface is suddenly separated from the melt) may lead to rapid temperature changes in the crystal (thermal shock) and an associated generation of large thermal stresses. The present numerical model does not adequately capture the solid-melt separation phenomenon and cannot be used to control this process. Furthermore, visual observation of the solid-melt interface during separation is not possible, and no other experimental indicators are available to ascertain that a smooth separation has been achieved. This lack of information introduces two types of uncertainties. First, the crystal length and its position inside the crucible after separation cannot be known accurately during the experiment. Thus, establishment of the "optimal" thermal profile in the HFCS during cool-down has to be achieved within the constraints of this uncertainty. The second uncertainty regards the stress history of the crystal during the separation period, especially as related to the extent of thermal shock in the crystal. Numerous crystal growth experiments have convinced us that proper separation is a primary factor in determining quality of the grown material. In the present experiments, all three crystals were separated from the melt in nearly (to the extent possible) identical manners. The last to freeze surface of the crystals, however, was not as small as desired. The similarity in the separation procedure suggests that, perhaps, the extent of thermal shock in each of the three crystals, if any, was the same.

As discussed above, the thermal-stress-control task was implemented in a feed-forward mode using the trajectory of HFCS thermal profile which was calculated prior to growth experiments. However, in order to reduce the errors in calculated stress fields associated with the uncertainties discussed above (principally the crystal length and position after separation), the cool-down calculations were repeated after the crystal was removed from the furnace, and its actual shape was measured.

The three experiments are discussed in the following by referring to their temperature and stress histories as calculated by the numerical model. The observed dislocation densities are, then, presented. In presenting the numerical results the following conventions are used: (a) isotherms are in terms of T/T_m where T_m is the melting point temperature of the matrix, and are plotted at 30 °C intervals; the isotherm passing through the crystal-melt interface in the growth simulations is at the melting point temperature. (b) arrows indicate the direction and relative magnitude of conductive heat transfer in the system, (c) areas where the excess resolved shear stress (as defined in part-I of this study) exceeds CRSS of the matrix are shaded, and (d) the time after seeding for each simulation is shown at the top of each plot.

CRYSTAL-1– A time-series of the temperature and excess stress fields for this crystal is shown in Fig. 4. In this case the HFCS temperature profile was *intentionally* chosen to generate a stress field, during growth, which exceeded the CRSS of the matrix. The isotherms in the crystal, Fig. 4 stages 1-5, indicate that the solid experienced radial heat loss to its environment during growth. Consequently, nearly the entire area of crystal is shaded indicating that the stresses exceed CRSS of the matrix everywhere; the total resolved shear stresses were of the order of $3-4 \times$ CRSS during growth. For this crystal the post growth cool-down thermal environment was not optimized, because significant dislocation multiplication during growth was expected. Results indicate, however, that during the initial stages of cool-down (Fig. 4, stages 6 and 7), the excessive stresses were confined to small areas at the periphery of the crystal. During the final cool-down stages of 8 and 9, the dashed areas cover increasing portions of the crystal.

CRYSTAL-2– In this case, Fig. 5, the HFCS temperature profile was controlled at values which would maintain the stresses in the crystal during growth (stages 1-5) at below the CRSS of the matrix. This can be observed from the nearly horizontal isotherms in the crystal, the vertical heat flux vectors indicating axial heat transfer in the solid, and the very small shaded areas in the solid. During separation of the crystal from the melt, however, the HFCS temperature profile was left unchanged. Once the crystal separated from the melt, heat transfer from the melt into the solid was drastically reduced, and thus, the axial temperature gradient in the crystal was lowered. Leaving the HFCS temperature profile unchanged from the last growth stage set up radial heat transfer into the crystal, Fig. 5 stage 6. The crystal, therefore, experienced excessive stresses during the initial stages of cool-down. In the subsequent cool-down stages the crystal is, also, observed to experience stresses exceeding CRSS.

CRYSTAL-3- The HFCS temperature profile in this case, Fig. 6, was maintained at values that, similar to the previous case, maintain the stresses at below CRSS during growth. Special care was taken in this case to adjust the HFCS temperature profile during separation so that the crystal separates from the melt into a thermal environment which does not induce radial temperature gradients in the solid. This can be observed in the relatively shallow radial gradients at stage 6 and very small shaded areas in the crystal during this and subsequent cool-down stages.

SUMMARY OF STRESS HISTORIES- In Figs. 4-6, time-series of the temperature field in the growth system and the stress distribution in the crystal was presented. The presented information on the stress field indicates areas where the total excess resolved shear stress exceeded CRSS, and thus, is to some extent qualitative. In Figs. 7 and 8 the calculated axial profiles of the von Mises stress (in multiples of CRSS) along the crystal centerline are presented for the three crystals. The figures cover growth stages 4-6 and cool-down stages 7-10. The von Mises stress is chosen as a succinct measure of the relative magnitude of stresses in the crystals [2]. Figure 7 clearly indicates that, during growth, Crystal-1 experiences stresses which are much larger than the other two. The stresses in Crystal-2 and -3 are, as intended, low and nearly identical. Crystal-2 is observed in Fig. 8 to experience high stresses throughout the cool-down process. The post growth stresses in Crystal-1 are initially low, but rise to match those of Crystal-2 during the last two cool-down stages. In spite of efforts to minimize stresses in Crystal-3 during crystal-melt separation, it is observed to experience relatively large stresses during the initial stage of cool-down. These stresses, however, are reduced to lower values (lowest of the three) in subsequent cool-down stages.

The thermal-stress history of the three crystals are qualitatively summarized in Table 1, where the words High and Low are relative to CRSS of the matrix.

Table 1: A Qualitative Summary of the Thermal Stress History of Grown Crystals

Experiment	Stresses During Growth	Stresses During Initial Cool-down	Stresses During Advanced Cool-down
Crystal-1	High	Low	High
Crystal-2	Low	High	High
Crystal-3	Low	Moderate	Low

[2]The choice of von Mises stress as opposed to excess stress is motivated by the following consideration. Excess stresses are calculated in terms of the excess of resolved shear stresses over CRSS in each slip system, and thus, all resolved stresses less than CRSS translate into zero excess stress regardless of their absolute values. In von Mises calculations such an off-set is not introduced. As we are investigating the relationship between stresses and dislocation multiplication in the crystal, it is necessary not to assume, *a priori*, that only stresses higher than CRSS need to be considered.

Dislocation Densities of the Crystals

Wafers sliced from the shoulder of the three crystals were etched in KOH, and the etch pit densities (EPD's), as measure of the dislocation density, were radially measured for each wafer. The axial location of the sliced wafers was chosen as to be away from the last-to-freeze section of the crystal, thus minimizing the potential impact of thermal shock during crystal-melt separation. Photographs of the etched surfaces are shown in Figs. 9 - 11. The radial EPD distribution for the three crystals is plotted in Fig. 12. Results indicate that Crystal-1 has, consistent with its calculated stress history, the highest EPD of the three crystals rising from 2×10^4 at the center to 7×10^4 cm^{-2} at its periphery. The EPD at the center of Crystal-2 is a low value of 3000 cm^{-2}. However, it rises to nearly 7×10^4 cm^{-2} at the outer periphery of the crystal. In Crystal-3 which experienced low stresses during growth and cool-down, 80% of the wafer area has an EPD of about 3000 cm^{-2}. The EPD increases, in a step-wise fashion, to 3×10^4 cm^{-2} in a very narrow annular region (approx. 5-mm thick) at the crystal periphery.

The dislocation distributions in the central core of the three crystals do not exhibit slip-related patterns. At the periphery, however, the etch pits are more ordered. This can be seen, for example, in Fig. 13 which is a low magnification picture of the Crystal-2 periphery. The etch pits can be clearly seen to be aligned along well-defined directions, suggesting the occurrence of slip in this area. The ordered alignment of etch pits close to the periphery of the crystal occurs in all three cases.

The nearly random distribution of etch pits in the central regions of the crystals suggests that these dislocations were created at elevated temperatures and have climbed out of the slip system. The high EPD's at the crystal peripheries, especially for Crystal-2 and -3, suggest significant slip of the matrix in that area. The ordered alignment of etch pits, however, suggests that this plastic deformation occurred at reduced temperatures where climb was inhibited. This explanation appears to be consistent, for Crystal-2 and -3, where a steep rise in the stresses was calculated during the initial stages of cool-down.

Discussion

The materials-related implication of the present work is clear: Dislocation multiplication in GaAs can be significantly reduced by maintaining the stresses in the crystal at below the CRSS of the matrix. Up to now there have been no quantitative evidence proving that by maintaining elastic stresses, calculated from the thermal strain field in the crystal, at below the CRSS of the matrix low dislocation density materials can be obtained. This does not, however, imply that dislocation multiplication does not occur at stresses lower than CRSS. Rather, it shows that CRSS is a good engineering *measure* of the resistance of the matrix to plastic deformation and dislocation multiplication.

Recently, Volkl and Muller, ref. [5], Maroudas and Brown, ref. [6], and Motakef, refs. [7,8] have studied the application of Alexander-Haasen (AH) creep model for dislocation multiplication in compound semiconductors. In this model dislocation multiplication occurs at all stress levels, and there are no well-defined threshold stresses.

The asymptotic analysis of Maroudas and Brown suggests that even at stress levels lower than CRSS, such as the ones achieved for Crystal-3, dislocation densities of the order of 10^5 cm^{-2} are generated at the growth front. This is not supported by the present results. On the other hand, Motakef has argued in ref. [9] that dislocation multiplication in melt-grown crystals occurs, primarily, beyond the growth interface and not immediately upon solidification as ref. 6] implies. He has shown that by maintaining the thermal strain iin the crystal at values corresponding to elastic stresses below CRSS of the matrix, the AH model predicts dislocation densities of the order of 5×10^3 cm^{-2}. This is in excellent agreement with the results of the present work. The observed density and distribution of dislocations in crystals grown in this study merit a more detailed investigation which will be undertaken in the future.

In addition to the above materials-related issues, the growth approach presented here has significant potential for the design and control of melt growth processes in general. We have used for the first time a numerical model, in conjunction with the developed hardware, to actively provide a growth thermal environment which reduces stresses in the crystal to below CRSS of the matrix and avoids the unnecessary lowering of other growth-related performance indicators associated with nearly iso-thermal growth. For example, growth of low dislocation density GaAs crystals has been reported at axial temperature gradients in the solid of about 7 °C/cm, ref. [9]. In contrast, the low EPD crystals grown by our technique had axial gradients of the order of 40°C/cm. As the rate of solidification of the material is related to the rate of heat removal from the growth interface, higher axial gradients in the crystal are desirable. Furthermore, as the growth process presented here is quantitative and the role of empiricism is minimized, there are no fundamental obstacles to the speedy development of growth hardware and control to increase the size of low EPD crystals (both in diameter and weight) and reduce the thickness of encapsulant from the levels used in our experiments. An example of such a system for growth of 7.5-cm diameter crystals from 3-kg charges is given in ref. [3].

Whereas the viability of integrating numerical modeling with growth experiments appears to be well established by the present work, two areas need further development. First, modeling and experimental capabilities need to be extended to provide for a better control of growth termination. Second, we need to improve our diameter control capability. The latter is, however, a limitation related to our growth facilities and does not reflect a general process issue.

Other Control Strategies

In Fig. 2 three approaches to integration of the model into the growth process were outlined. They are evaluated in the following.

Currently, diameter controllers are empirically constructed using the information gained from several growth experiments. Therefore, at the current level of technology, the first control structure (Fig. 2(a)) which decouples the stress- and diameter-control tasks is readily achievable. This was shown, with some limitations on the adequacy of the diameter control, in our experiments. The empirical approach to diameter control, however, requires

that the growth thermal environment does not change in-between the "learning" experiments. Therefore, the first control structure is suitable for production environments, where once the growth process is defined, the HFCS temperature history is kept the same for all growth runs. In research and development work, however, the growth thermal environment (the HFCS temperature history) must be changed to explore various growth-properties issues. The resources needed to empirically develop a control algorithm for each HFCS thermal history are prohibitively large. Thus, the second control structure of Fig. 2 suggests itself. Here the actual shape of the growing crystal is inputted into the model, and the numerical calculations are performed on-line. The on-line use of the numerical model is not, in itself, a major obstacle. The turn-around time for our numerical model is sufficiently fast to provide for nearly real-time control of the process. The shortcoming of this approach stems, however, from the potential instability introduced into the process by combining a feed-forward with a feed-back control loop. To illustrate the source of this instability, consider the following. To achieve diameter control, the rate of solidification of the crystal should be maintained equal to the pull-rate; otherwise, the crystal will either cut-in or grow-out. The crystal solidification rate is determined by the difference between the rate of heat extraction and heat input at the growth surface. The diameter controller adjusts the heat input component of this balance through the main heater, and the model-based stress controller adjusts the heat extraction rate through the HFCS. Therefore, as the temperature profile of the model-driven HFCS is being changed to control the stresses in the crystal, the diameter controller attempts at controlling the heat input rate as to balance a heat extraction rate which is changing unpredictably (as viewed by the diameter controller) in time. As the time constant associated with the rate of heat input by the main heater is much larger than that associated with heat removal rate by the HFCS, it is can be seen that the overall control process may go unstable. Indeed, we have had several experimental cases where attempts at this type of control lead to irrecoverable loss of diameter uniformity.

We have also tried the third control structure of Fig. 2 which uses feed-forward control of diameter and stresses by the model. In experiments where we followed the model predictions to control the crystal diameter, the crystal diameter would either cut-in or grow-out uncontrollably during the cone-formation stage. Our overall experience indicates that to achieve model-based diameter control the accuracy of the model must be significantly improved. Two factors bear on this issue. First, the degree of accuracy required for prediction of crystal solidification rate is much higher than that required for control of stresses at below CRSS. For example, it can be readily shown that whereas the assumption of conduction-dominated heat transfer in the melt does not introduce appreciable errors in stress calculations, ref [10], it introduces large errors in the heat transfer rate into the growth surface. Therefore, the crystal growth rate cannot be predicted accurately enough for diameter control purposes. The second issue relates to the dynamics of diameter control. Kelly has shown in ref. [2] that once the crystal diameter has moved away (for some reason) from the required value, it is extremely difficult to adjust growth conditions to correct this deviation and continue the solidification process following the model-based trajectory calculated on the basis of the desired diameter.

In summary, of the three possible approaches to the integration of numerical model with the growth process, the one used in this study is the most promising, stable, and directly transportable to the production environment.

References

1. K. W. Kelly, K. Koai, and S. Motakef, J. Crystal Growth (1991) in review..
2. K. W. Kelly, Doctoral Dissertation, Dept. of Mech. Eng., M.I.T. (1990).
3. K. Koai, Doctoral Dissertation, Dept. of Mech. Eng., M.I.T. (1990).
4. A. S. Jordan, Von Neida, and R. Caruso, Bell Syst. Tech. J. **59** (1980) 593.
5. J. Volkl and G. Muller, J. Crystal Growth, **97** (1989) 136.
6. D. Maroudas and R. A. Brown, J. Crystal Growth (1990) in press.
7. S. Motakef, J. Crystal Growth **108** (1991) 33.
8. S. Motakef, J. Crystal Growth, (1990) in review.
9. A. G. Elliot, et al., J. Crystal Growth, **70** (1984) 169.
10. K. W. Kelly, K. Koai, and S. Motakef, Proc. of Intern'l. Seminar. on Advanced Heat Trans. in Mfg. and Proc. of New Materials, Tomakomai, Japan (1990).

Figure Captions

Fig. 1 Schematic of the growth configuration.

Fig. 2 Three control structures integrating the numerical model with the growth process. The first structure is the one used in this study.

Fig. 3 Geometry traces of the three crystals studied and the geometric approximation of their shapes used in the calculations.

Fig. 4 Results of numerical simulations for growth and cool-down of Crystal 1.

Fig. 5 Results of numerical simulations for growth and cool-down of Crystal 2.

Fig. 6 Results of numerical simulations for growth and cool-down of Crystal 3.

Fig. 7 Axial variation of the ratio of von Mises stress to CRSS along the centerline of the three crystals during growth. The bold numbers in the upper left corner correspond to number of stages in figs. 4–6.

Fig. 8 Axial variation of the ratio of von Mises stress to CRSS along the centerline of the three crystals during cool-down. The bold numbers in the upper left corner correspond to number of stages in figs. 4–6.

Fig. 9 Photographs of KOH-etched surfaces of a wafer sliced from below the shoulder of Crystal 1. The areas of micrographs are 12 mm^2.

Fig. 10 Photographs of KOH-etched surfaces of a wafer sliced from below the shoulder of Crystal 2. The areas of micrographs are 12 mm^2.

Fig. 11 Photographs of KOH-etched surfaces of a wafer sliced from below the shoulder of Crystal 3. The areas of micrographs are 12 mm^2.

Fig. 12 The radial distribution of the EPD in the wafers from the three crystals.

Fig. 13 A low magnification of the etch-pit distribution at close to the periphery of Crystal 2. The alignment of the etch pits suggests occurrence of slip in this area. The micrograph area is 192 mm^2.

1- Quartz Crucible
2- Heat Flux Control System (HFCS)
3- Graphite Furniture (20 cm dia.)
4- Cavity Thermocouple
5- Radiation Shield
6- Main Heater
7- Main Heater Control Thermocouple
8- Water-Cooled Shaft
9- Insulation Layer
10- Graphite Crucible Support
11- Tubing Support

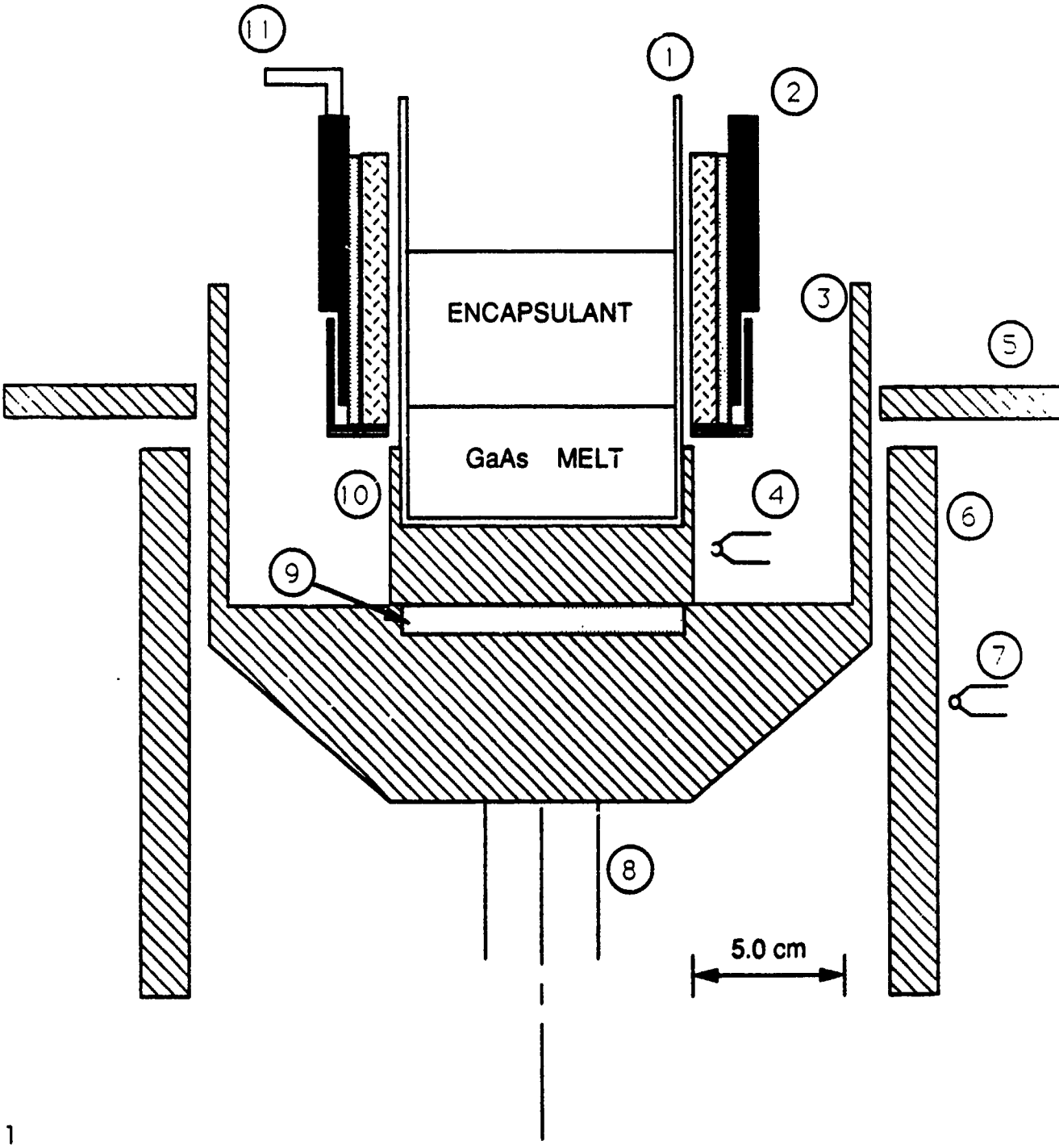

Fig. 1

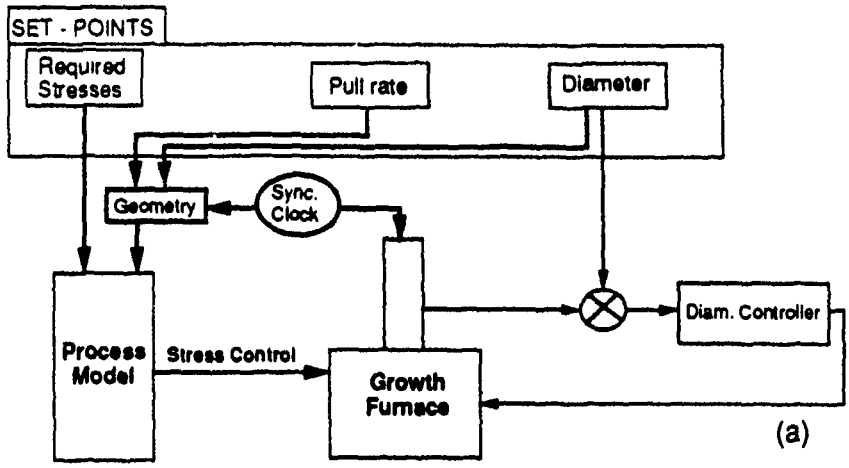
SET - POINTS
Required Stresses
Pull rate
Diameter
Geometry
Sync. Clock
Process Model
Stress Control
Growth Furnace
Diam. Controller
(a)

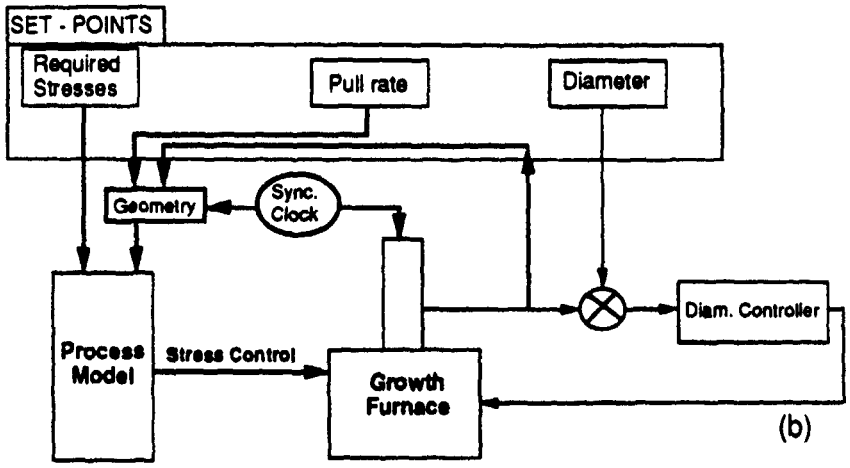
SET - POINTS
Required Stresses
Pull rate
Diameter
Geometry
Sync. Clock
Process Model
Stress Control
Growth Furnace
Diam. Controller
(b)

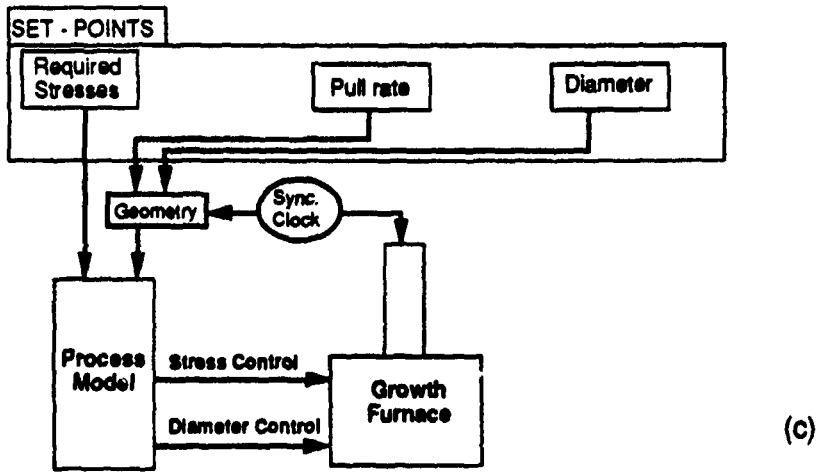
SET - POINTS
Required Stresses
Pull rate
Diameter
Geometry
Sync. Clock
Process Model
Stress Control
Diameter Control
Growth Furnace
(c)

Fig. 2

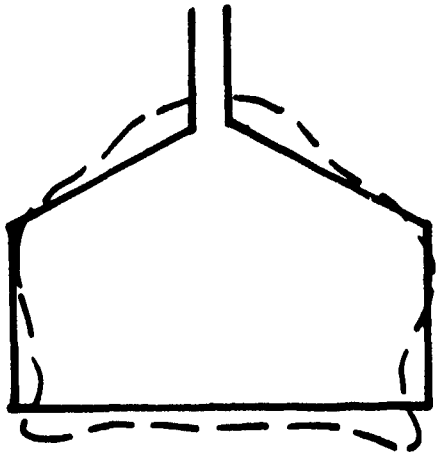

(a) Crystal-1

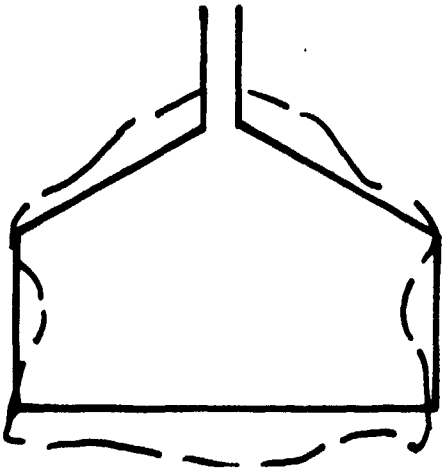

(b) Crystal-2

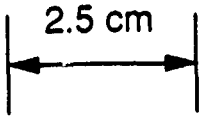

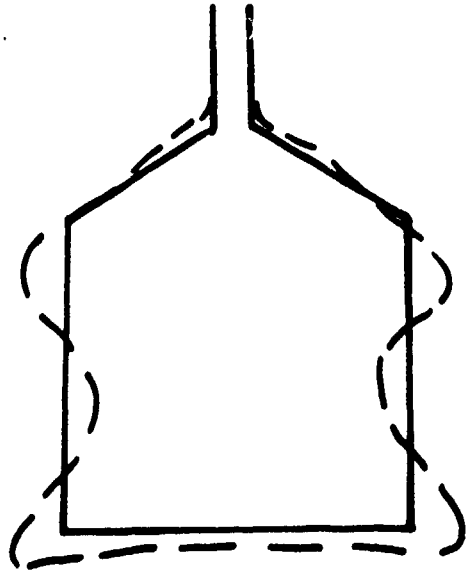

(c) Crystal-3

Fig. 3

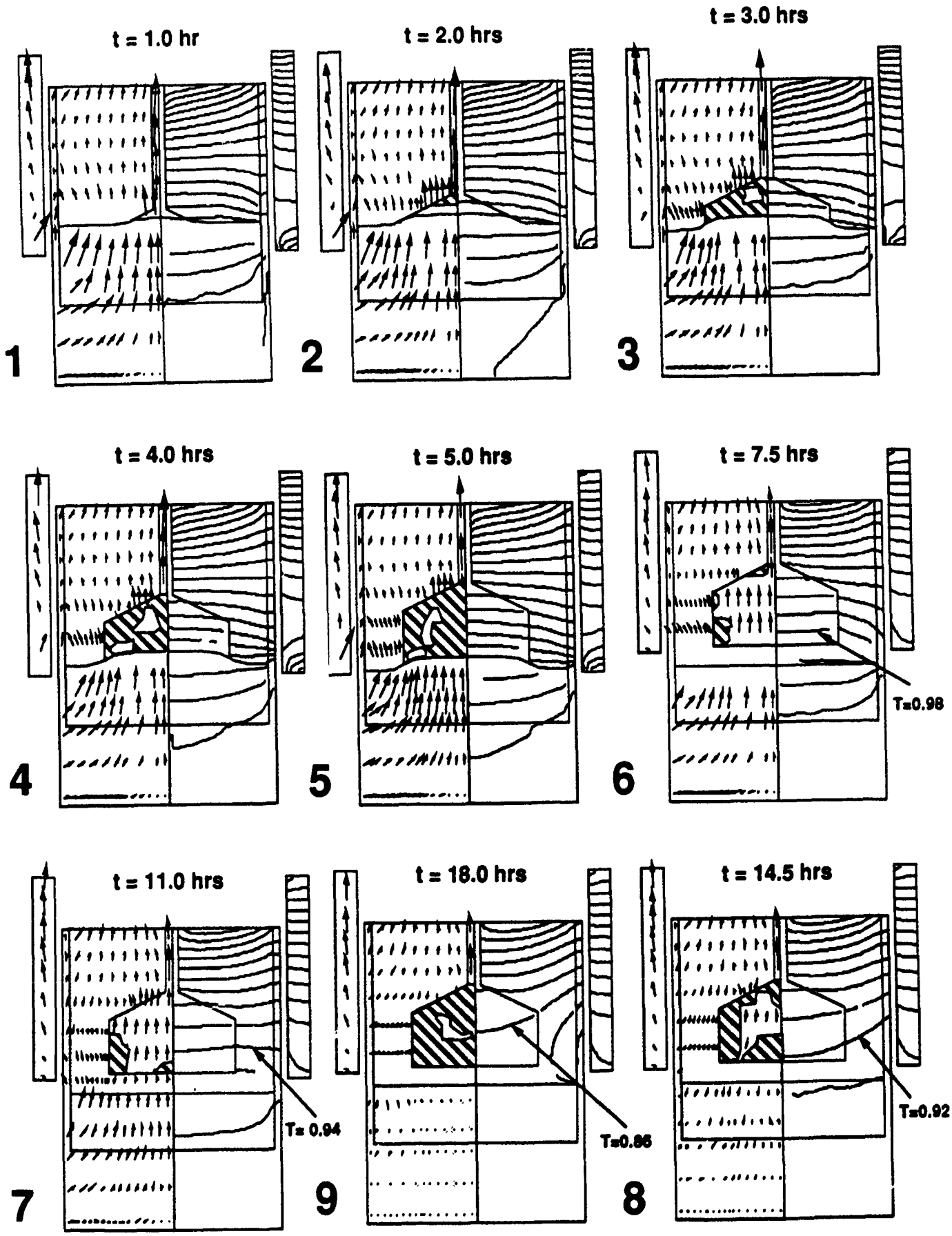
t = 1.0 hr
t = 2.0 hrs
t = 3.0 hrs
1
2
3
t = 4.0 hrs
t = 5.0 hrs
t = 7.5 hrs
T=0.98
4
5
6
t = 11.0 hrs
t = 18.0 hrs
t = 14.5 hrs
T= 0.94
T=0.86
T=0.92
7
9
8

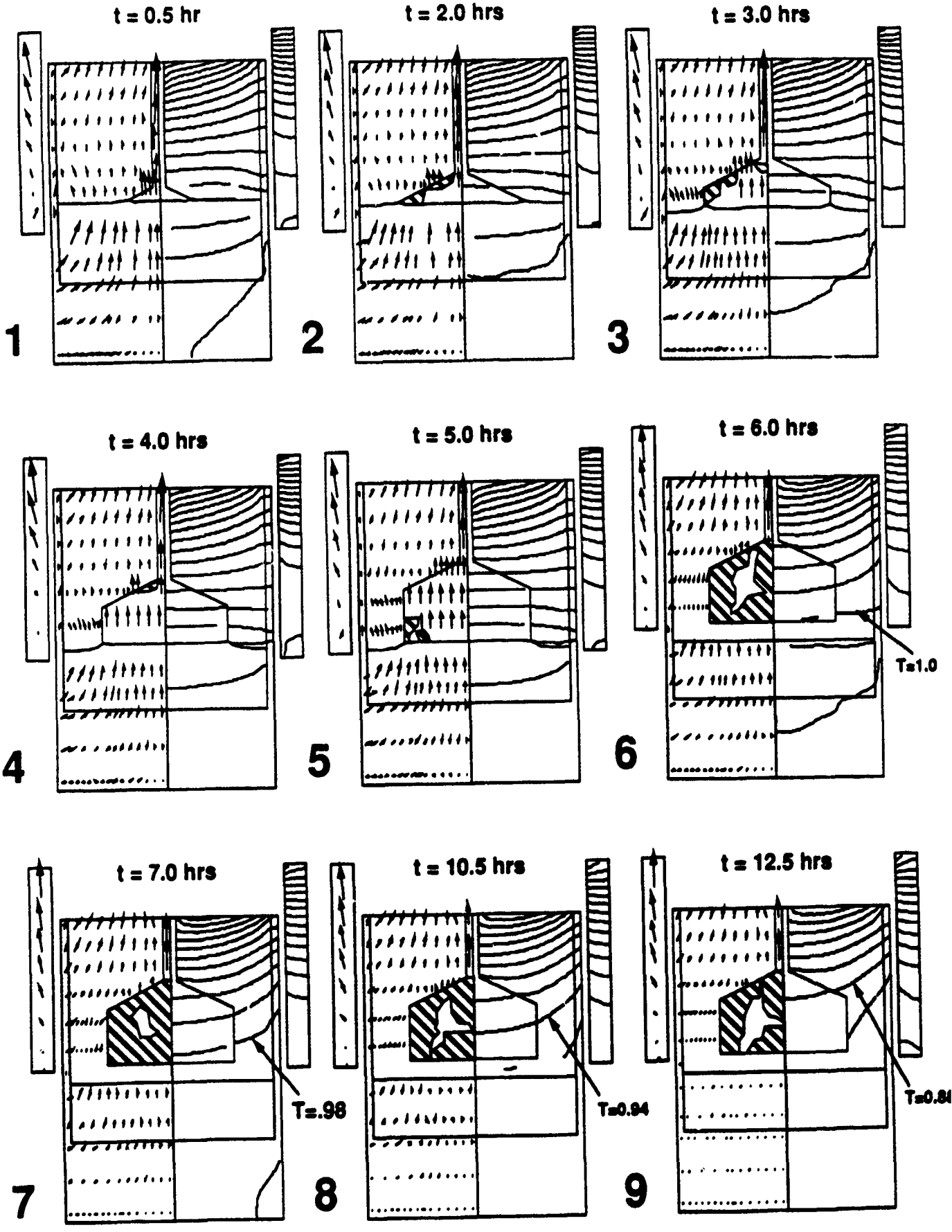
t = 0.5 hr
t = 2.0 hrs
t = 3.0 hrs
1
2
3
t = 4.0 hrs
t = 5.0 hrs
t = 6.0 hrs
T=1.0
4
5
6
t = 7.0 hrs
t = 10.5 hrs
t = 12.5 hrs
T=.98
T=0.94
T=0.84
7
8
9

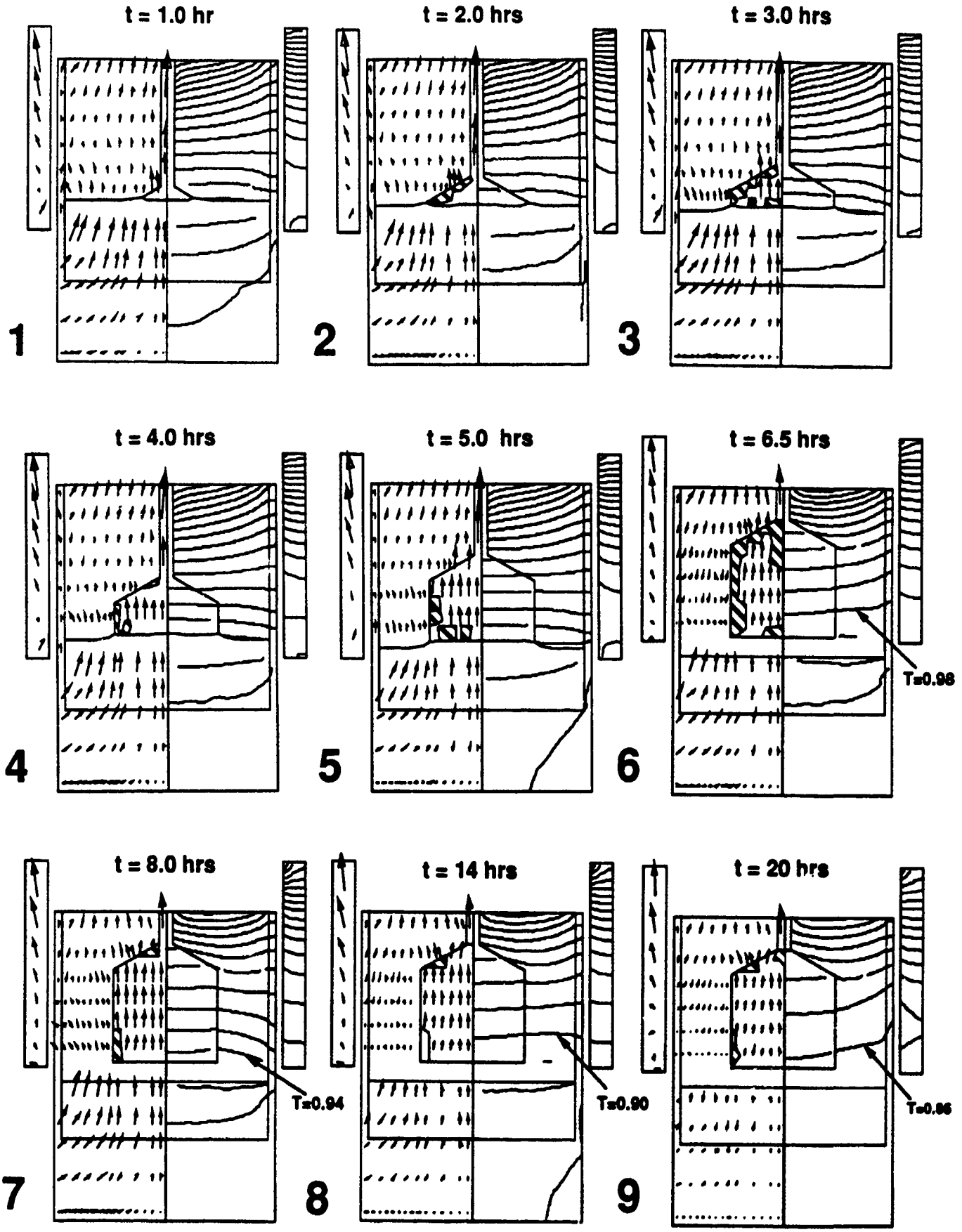
t = 1.0 hr
t = 2.0 hrs
t = 3.0 hrs
1
2
3
t = 4.0 hrs
t = 5.0 hrs
t = 6.5 hrs
T=0.98
4
5
6
t = 8.0 hrs
t = 14 hrs
t = 20 hrs
T=0.94
T=0.90
T=0.86
7
8
9

Fig. 6

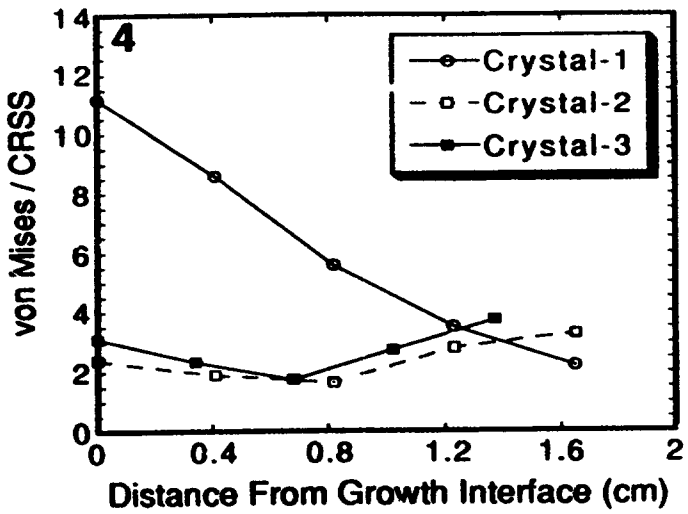
4
Crystal-1
Crystal-2
Crystal-3
von Mises / CRSS
Distance From Growth Interface (cm)
0
2
4
6
8
10
12
14
0
0.4
0.8
1.2
1.6
2

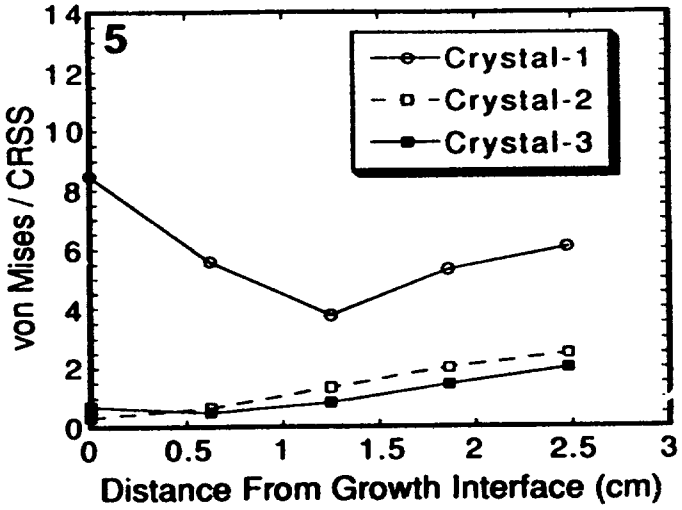
5
Crystal-1
Crystal-2
Crystal-3
von Mises / CRSS
Distance From Growth Interface (cm)
0
2
4
6
8
10
12
14
0
0.5
1
1.5
2
2.5
3

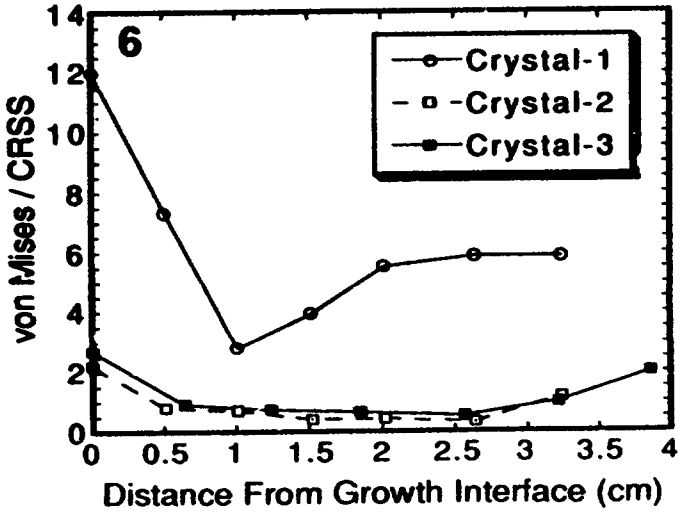
6
Crystal-1
Crystal-2
Crystal-3
von Mises / CRSS
Distance From Growth Interface (cm)
0
2
4
6
8
10
12
14
0
0.5
1
1.5
2
2.5
3
3.5
4

Fig. 7

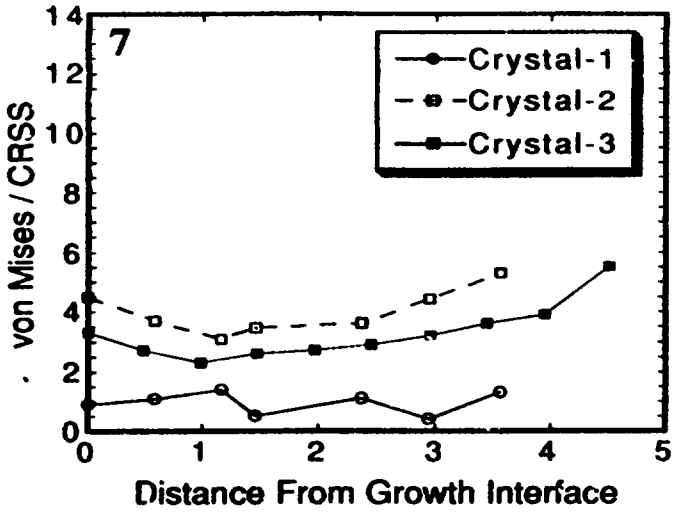
7
Crystal-1
Crystal-2
Crystal-3
von Mises / CRSS
Distance From Growth Interface

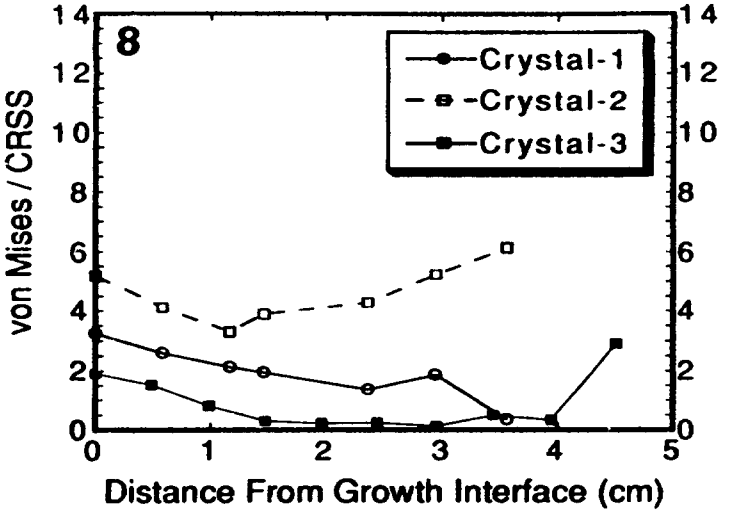
8
Crystal-1
Crystal-2
Crystal-3
von Mises / CRSS
Distance From Growth Interface (cm)

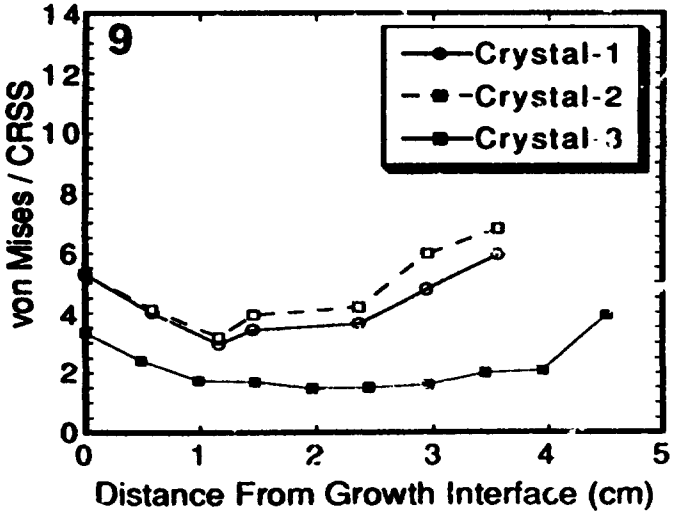
9
Crystal-1
Crystal-2
Crystal-3
von Mises / CRSS
Distance From Growth Interface (cm)

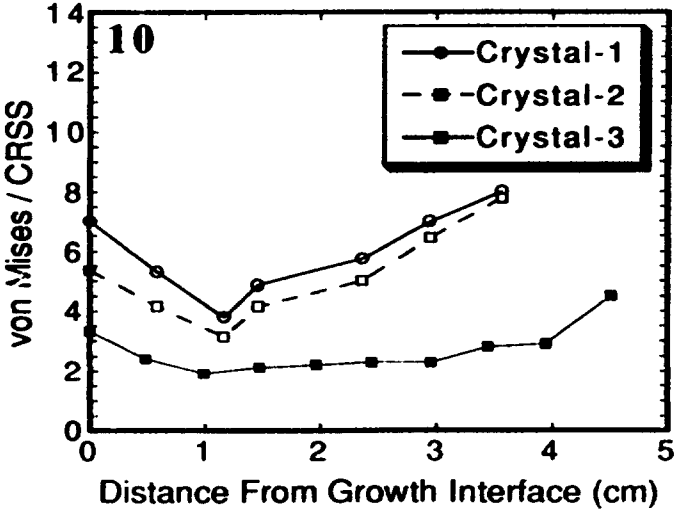
10
Crystal-1
Crystal-2
Crystal-3
von Mises / CRSS
Distance From Growth Interface (cm)

Fig. 8

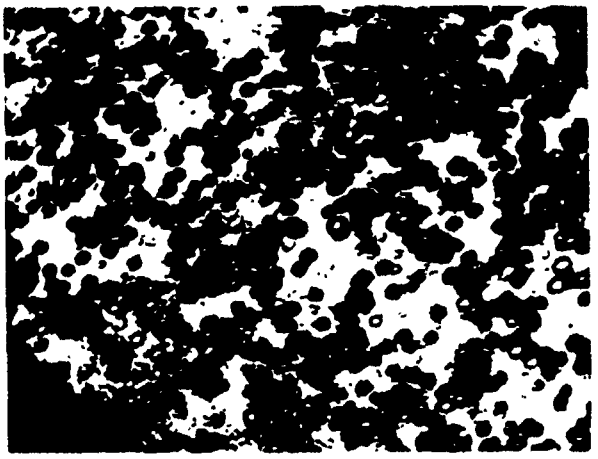

Area of Each Photo= 12 mm^2

Normalized Radius= 1.0

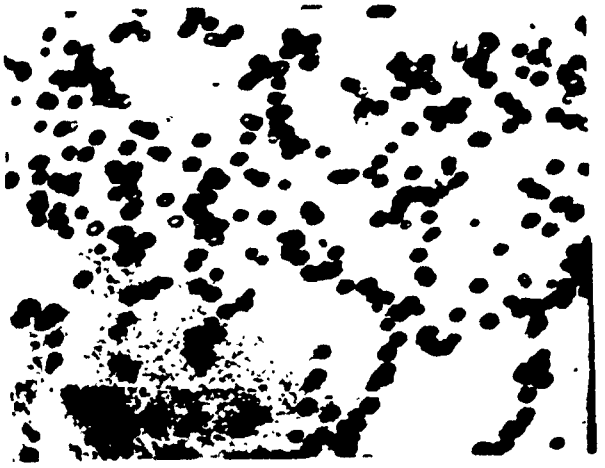

Normalized Radius= .5

Normalized Radius= 0

Fig. 9

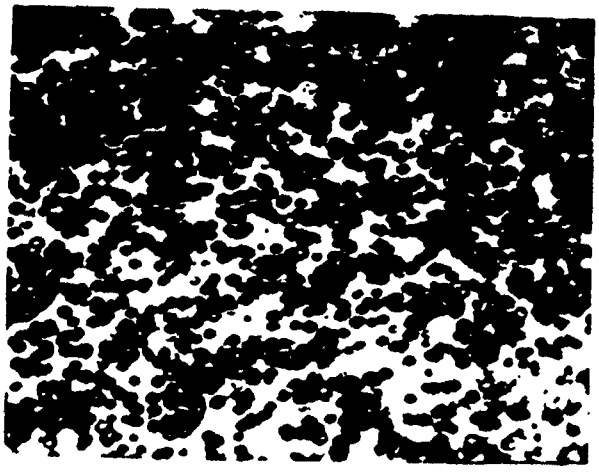

Area of Each Photo= 12 mm^2

Normalized Radius= 1.0

Normalized Radius= .5

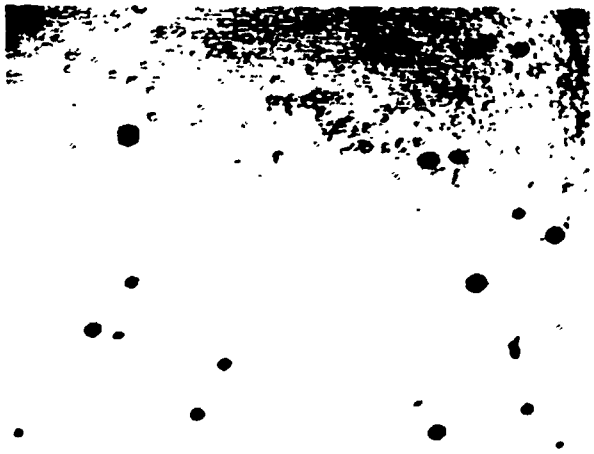

Normalized Radius= 0

Fig. 10

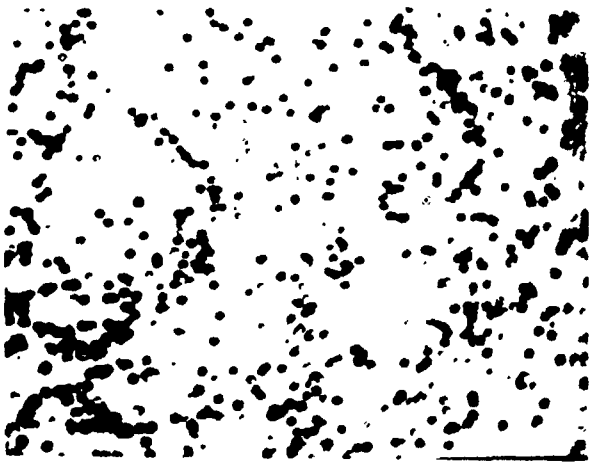

Area of Each Photo= 12 mm^2

Normalized Radius= 1.0

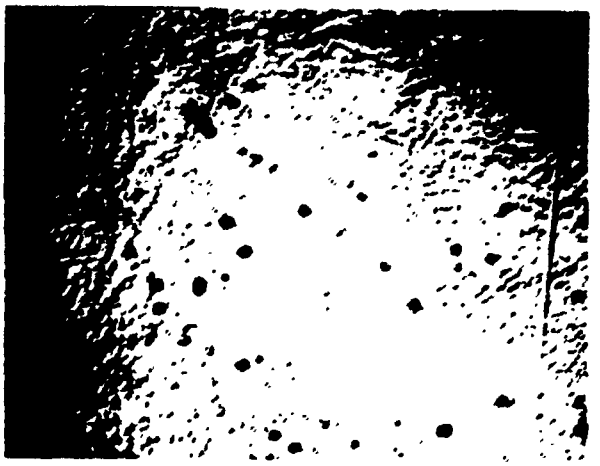

Normalized Radius= .5

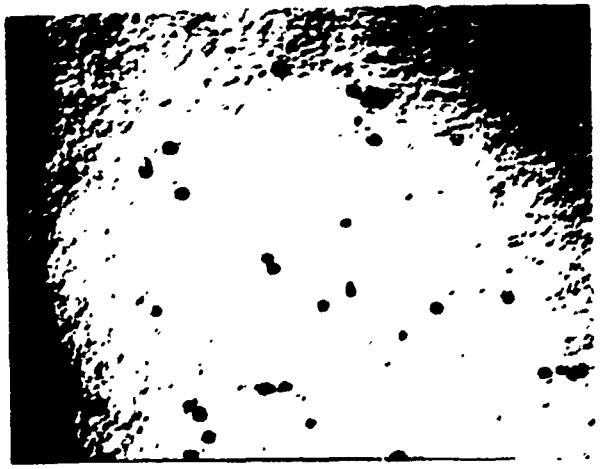

Normalized Radius= 0

Fig. 11

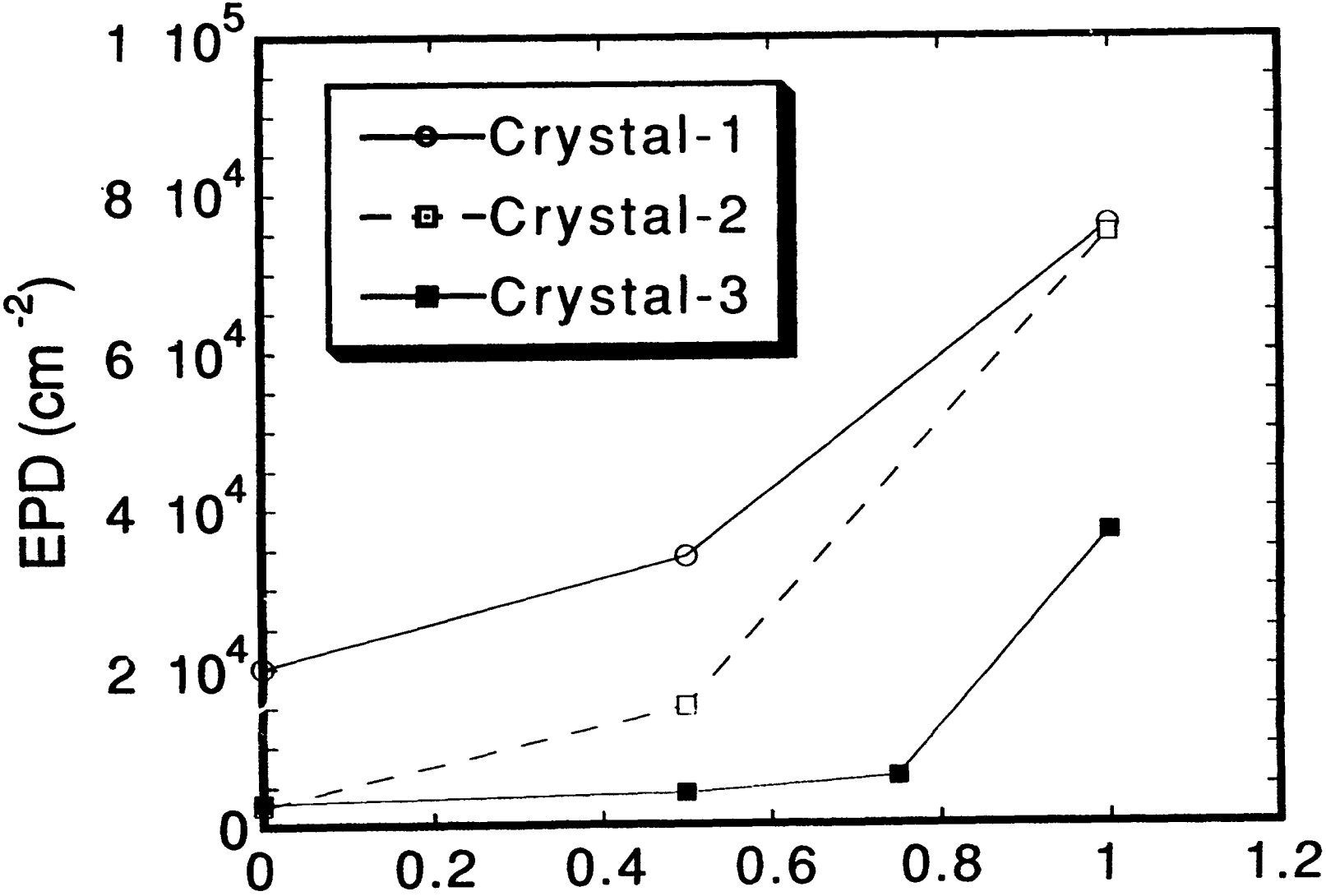
1 10^5
8 10^4
6 10^4
4 10^4
2 10^4
0
EPD (cm^-2)
Crystal-1
Crystal-2
Crystal-3
0
0.2
0.4
0.6
0.8
1
1.2

Fig. 12

Area of Photo is 192 mm^2

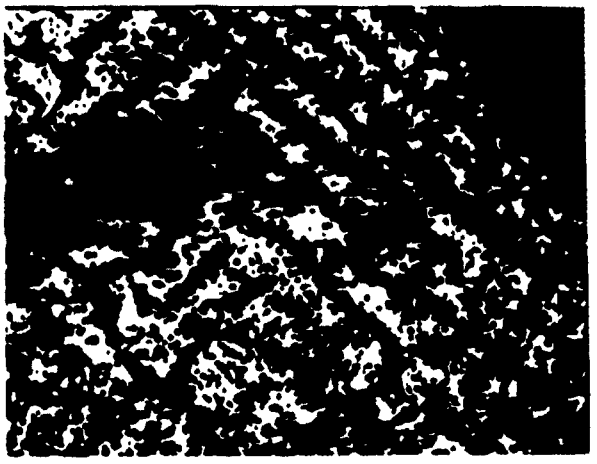

Fig. 13

COMPARISON OF CALCULATED AND MEASURED DISLOCATION DENSITY IN LEC-GROWN GaAs CRYSTALS

Introduction

The creep model presented in ref. [1] is used in this paper to analyze the observed dislocation density in several GaAs crystals. We have shown in ref [2] that the dislocation density of GaAs crystals can be reduced to low-10^3 cm^{-2} values by maintaining the thermal stresses, during all stages of growth and cool-down, in the crystal at close to or below the critical resolved shear stress (CRSS) of the matrix. The thermoelastic formulation used in the control and analysis of those experiments (Schmid's law) assumes that as the *elastic* resolved shear stresses exceed the CRSS of the matrix, significant dislocation multiplication may be expected. Although this model appears to be confirmed by our experimental results, it does not provide for quantitative prediction of the dislocation density in the grown material. At the presently attainable dislocation densities (high-10^2 to low-10^3 cm^{-2}), the ability to quantitatively distinguish between the nucleated and grown-in versus the multiplied dislocation is a pre-requisite for identifying approaches to further reduce the dislocation density in GaAs crystals.

The high temperature creep model proposed for GaAs in ref. [1] is based on the Alexander-Haasen model, ref. [3], which relates dislocation multiplication and the creep strain rate to the prevailing stresses in diamond crystals. The objective of this paper is to establish whether this model can be used to predict the dislocation density in GaAs crystals. To this end, two melt-grown crystals are considered. First, a crystal grown by the conventional Liquid Encapsulated Czochralski (LEC) process with etch pit density (EPD) values in the mid- to high-10^4 cm^{-2} range, and second, a crystal grown by the modified LEC growth process of ref. [2] where model-based control of stresses has resulted in EPD values of 3×10^3 cm^{-2} in the central portion ($r < 0.8$ of radius) of the grown material. The latter represents, in essence, the lower range of dislocation densities currently achievable. The time-history of the temperature field in the two crystals are quantified by the mathematical models of the growth process described in refs. [2,4,5].

We begin by a brief review of the creep model and the two growth experiments. The observed dislocation densities in the two crystals are, then, compared to the values predicted by the model. Results of this analysis are used to construct an emerging picture for dislocation multiplication in GaAs.

Creep Model

The Alexander-Haasen (AH) creep model starts from the following Orowan equation:

$$\frac{d\epsilon_c}{dt} = \phi N b v, \tag{1}$$

where $\dot{\epsilon_c}$ is the creep strain rate, ϕ a geometric factor relating shear and normal strains, N the density of mobile dislocation, b the burgers vector, and v velocity of the dislocations.

The dislocation velocity for elemental semiconductors was found, ref. [3], to be related to the applied stress by the following empirical relationship:

$$v = B_o e^{\frac{-Q}{kT}} (\tau - A\sqrt{N})^m \tag{2}$$

In the above Q is the activation energy, k Boltzmann constant, T temperature, A the self-stress coefficient, and B_o a constant of proportionality referred to as the mobility of dislocations. The dislocation multiplication rate was found to be proportional to the density and velocity of the mobile dislocations, and the "effective stress" $(\tau - A\sqrt{N})$ to some exponent p. Thus, the two principal equations of the model may be written as:

$$\frac{d\epsilon_c}{dt} = \phi N b B_o e^{\frac{-Q}{kT}} (\tau - A\sqrt{N})^m \tag{3}$$

and

$$\frac{dN}{dt} = K N B_o e^{\frac{-Q}{kT}} (\tau - A\sqrt{N})^{m+p} \tag{4}$$

The self-stress term $A\sqrt{N}$ in the above is typically small and can be neglected. The physical constants appearing in eqs. (3) and (4), with the exception of the dislocation multiplication factor K, were estimated from the available data on CRSS and velocity of dislocations in undoped GaAs in ref. [1], and are listed in Table 1. In this approach the dislocation mobility coefficient, B_o, of GaAs was found to be close to the experimentally obtained value for InP. As the crystalline structure and electronic properties of the two materials are similar, it was suggested in ref. [1] that the dislocation multiplication factor for GaAs may be estimated to be the same as that of InP. The value for K appearing in Table 1 is taken from ref. [6] for InP.

Plastic deformation during solidification and subsequent cool-down of a material element has been modeled to consist of two stages in ref. [7]. The first stage is associated with the transformation of the liquid to the solid phase, during which the isothermal strain-free freshly solidified element is subjected to stresses determined by the overall force balance in the bulk. The second stage covers the subsequent cool-down period during which the material experiences thermal loading. It was argued in ref. [7] that only variations in the thermal strain field subsequent to the solidification of the material (stage-II) result in plastic deformation and dislocation multiplication in the crystal. During this period the thermal strain associated with the non-uniformity of the temperature field in the crystal is reduced by the accumulating creep strain. Denoting the stress in the matrix as τ, Hooke's Law may be written as:

$$\tau = \frac{G}{\phi}(\epsilon_{th} - \epsilon_c) \tag{5}$$

In the above ϵ_{th} is the thermal strain, and G is the shear modulus.

The uni-axial model of eq. (5) may be extended to a multi-axial state by assuming isotropic plasticity. This is a simplifying assumption which neglects the preferential slip system of the crystal. However, the errors in stress calculations introduced by this approximation are no more than a factor of 2-3. In this formulation thermal stresses in the crystal may be represented by the von Mises stress, τ_{vm}. Equation (5), then, becomes:

$$\tau = \tau_{vm} - \frac{G}{\phi}\epsilon_c \tag{6}$$

Equation (3) applies to *monotonic* variation of τ in time. This can be observed from the following relationship by combining eqs. (3) and (4):

$$\frac{d\epsilon_c}{dt} \simeq (\tau_{vm} - \frac{G}{\phi}\epsilon_c)^m \tag{7}$$

To illustrate the deficiency of eq. (3) consider, for example, the following situation. The thermal strain field, and thus τ_{vm}, is constant for some time. During this period creep strain is accumulated according to eq. (7) until $d\epsilon_c/dt$ becomes equal to zero. Now, if τ_{vm} begins to decrease in time, the term in parenthesis of eq. (7) becomes negative, and $d\epsilon_c/dt$ can not be evaluated. During this period of decreasing τ_{vm}, however, the crystal does undergo creep and associated dislocation multiplication. Thus, eqs. (3) and (4) are modified to provide for dislocation multiplication with non-monotonic variations of τ_{vm}:

$$\frac{d\epsilon_c}{dt} = \phi N b B_o e^{\frac{-Q}{kT}} \mid \tau \mid^m sgn(\tau) \tag{8}$$

$$\frac{dN}{dt} = K N B_o e^{\frac{-Q}{kT}} \mid \tau \mid^{m+p} \tag{9}$$

where $sgn(\tau)$ indicates the signature of τ. The above issue appears not to have been noticed by Maroudas and Brown, ref. [8], who have erroneously assigned the inability to calculate $d\epsilon_c/dt$ from eq. (3) for $\tau_{vm} < \frac{G}{\phi}\epsilon_c$ to some "locking-in" mechanism of dislocations.

The temporal evolutions of τ_{vm} for the cases studied in this work are obtained from the solution of axisymmetric thermoelastic equations using the calculated time-history of temperature field in the crystal during growth and cool-down. The mathematical models used to calculate the temperature field in GaAs crystals grown by the LEC and modified-LEC processes are fully described in refs. [2,4,5,9]. We have shown that the model predictions agree very well with experimental data, ref. [5,10].

Crystal Growth Experiments

The wafers studied in this work are from two crystals. The chosen crystals have well-quantified growth histories, allowing for unambiguous calculation of the time-variation of stress and temperature fields in the crystal.

Two high-EPD (mid- to high-10^4 cm^{-2}) wafers, W-1 and W-2, are taken from the top part of a crystal grown by the conventional LEC technique. The crystal has a nominal diameter of 5 cm, and is 12.5-cm long. A trace of the crystal shape and the geometric approximation used in the numerical calculations are shown in Fig. 1. The location of wafers studied is also indicated. The wafers were selected from the top portion of the crystal to minimize the impact of crystal-melt separation, and the associated thermal shock in the crystal, on the dislocation density of the grown material. This crystal was grown from a 3-Kg charge in a 15-cm diameter crucible at a nominal pull rate of 1 cm/hr. The encapsulant thickness, at full diameter growth conditions, was 2 cm. The crystal was separated from the melt by increasing the pull rate. After separation, power to the main heater was turned off. The cool-down for this experiment is modeled to have taken place over three hours. The local values of temperature and von Mises elastic stress calculated to be present before crystal-melt separation are assumed to decrease monotonically to room temperature and zero stress during this period.

The second crystal is the same as Crystal-3 of ref. [2]. A detailed description of the process used for growth of this crystal is given there, and only a brief summary is presented here. The trace of this crystal shape, nominal diameter of 4.83 cm, the geometric model used in the calculations, and location of the studied wafer, W-3, are shown in Fig. 2. The numerical model was used, during growth and cool-down of this crystal, to control the growth thermal environment such that the resolved shear stresses in the crystal remain below the CRSS of the matrix. The crystal, however, did experience a transient increase in the thermal stresses during the initial cool-down stages. As fully discussed in ref. [2], our numerical model does not adequately capture the crystal-melt separation period. Thus, the temperature and stress fields are assumed to vary uniformly from the calculated values at the last growth stage to those of the first cool-down stage. Of the three crystals reported in ref. [2], the present one is considered to have been least influenced by (unquantified) thermal shock effects during crystal-melt separation.

Results

HIGH-EPD CRYSTAL– The calculated time-history of τ_{vm} (in multiples of CRSS of the matrix evaluated at its melting point temperature) and the dislocation density at four radial positions for wafers W-1 and W-2 are shown in Figs. 3 and 4, respectively. The measured EPD at each radial position, the time at which the crystal is calculated to emerge from the encapsulant, and the time corresponding to growth termination are shown on the figures.

In calculations presented here the initial dislocation density is taken to be 10^3 cm^{-2}. As dislocation multiplication for this crystal is substantial, the assumed initial dislocation density has a minimal influence on the final value, ref. [7].

The outstanding features of the present results are:

1. The thermal stress profiles exhibit complex non-monotonic variations with time. The stresses, generally, decrease from the crystal axis, towards the mid-annular region

beyond which they increase towards the crystal periphery.

2. Substantial dislocation multiplication is observed to occur, in both W-1 and W-2, while they are encapsulated by the boric oxide.

3. Dislocation multiplication during the cool-down period is minimal for W-1 (with the exception of crystal periphery). The dislocation density of W-2 is calculated to increase by a factor of nearly 2 during this period.

4. The calculated dislocation densities agree reasonably well with the measured EPD values in the central regions of the crystal. The calculated and measured values deviate significantly towards the crystal edge.

LOW-EPD CRYSTAL– The calculated time variations of τ_{vm} and the dislocation density at four radial locations of W-3, as well as the measured EPD values, are shown in Fig. 5. The two vertical lines in Fig. 5 bracket the period between last growth simulation and first cool-down simulation. This period represents the uncertainty in modelling prediction associated with crystal-melt separation.

As the calculated final dislocation densities are of the order of 10^3 cm^{-2}, the initial dislocation density in these calculations is taken to be 10^2 cm^{-2}. Insofar as this assumed value is less than 10^3 cm^{-2}, it has a negligible influence on the final calculated dislocation density.

The obtained results may be summarized as:

1. The stresses are much smaller than those calculated to be present in W-1 and W-2.

2. The stresses exhibit a spike-type increase during the period of crystal-melt separation.

3. The dislocation multiplication process (from the assumed value of 100 cm^{-2}) occurs rapidly during the initial stages of growth. The dislocation density stabilizes after this initial rise until the last growth stage and crystal-melt separation period.

4. Appreciable dislocation multiplication occurs during the crystal-melt separation. Subsequent multiplications during cool-down are relatively negligible.

5. The measured EPD values and calculated dislocation densities agree very well in a large central portion of the crystal. At the crystal periphery the agreement is not good.

SUMMARY OF RESULTS– The measured EPD and the calculated dislocation density in the three wafers are cross-plotted in Fig. 6. Results indicate an extremely good agreement for a large fraction of the data. The points that fall outside the $\pm 100\%$ band are *all* from radial locations close to the crystal periphery.

Considering that the assumed isotropic plasticity model is an approximation to the slip-mechanism in single crystals and that the data cover a more than one-decade variation, the agreement between the measured and calculated data is extremely good.

Discussion

The agreement between the calculated values of dislocation density and measured EPD's clearly indicates that the creep model proposed in ref. [1] and the arguments set forth in ref. [7] apply to multiplication of dislocations in GaAs crystals. The only anomaly is the disagreement close to the crystal periphery. In this context it is important to note that the dislocations at the crystal periphery always reflect an ordered alignment, suggesting presence of slip. Therefore, any explanation of this anomaly must include, to some extent, a slip-based dislocation multiplication mechanism.

The following is a partial list of possible causes for the significant difference between the predicted and measured dislocation densities close to the periphery of the crystals.

1. Cyclical stressing of the crystal periphery associated with the rotation of the solid in a non-axisymmetric thermal environment.
2. Deviation of the solid stoichiometry associated with Arsenic loss from the matrix leading to:
   (i) local generation of stresses by Ga precipitates, and/or
   (ii) reduction of the matrix resistance to plastic deformation and dislocation multiplication.
3. Presence of a significantly high density of immobile dislocations in that region
4. Surface damage associated with the differential thermal expansion of an adhered layer of boric oxide and the crystal during cool-down.

The first possibility is suggested by the localization of the high-EPD region at the outer 5-mm annular region of W-3. A simple thermal diffusion thickness calculation of $\delta \simeq \sqrt{\alpha t}$ yields a characteristic time scale of about 20-30 seconds for GaAs. This corresponds to a differential rotation between the crystal and crucible of rate of 2-3 rpm, which is close to the experimental values. These calculations suggest that as the crystal is rotated in an unavoidably asymmetric thermal environment, a thin peripheral layer of the crystal is subjected to cyclical thermal variations which may set up sufficiently large thermal strains in the crystal to promote dislocation multiplication. Considering the sensitivity of the dislocation multiplication process (in the AH model) to stresses in the crystal, it is readily conceivable that a 2-3°C radial asymmetry of the thermal environment may lead to significant generation of dislocations close to the crystal periphery.

With regards to the second issue identified in the above list, it must be noted that high dislocation densities at the crystal periphery are reported for crystals which have been

grown by total encapsulation, refs. [2,11], as well as the ones grown by conventional LEC. Thus, if As loss is the operative mechanism, As dissolution into the boric oxide as well as its evaporation from the unencapsulated portion of the crystal must be occurring. Whereas As loss from the exposed crystal is well-established, the rate of its dissolution in boric oxide is not presently known. The associated factors promoting dislocation multiplication at the crystal periphery are also not well understood. First, the degree to which Ga precipitates create localized stresses (i.e., the size distribution of Ga precipitates) is not well documented. Second, the influence of deviations from the solid-state stoichiometry on the plastic deformation behavior of the crystal has not been investigated. In short, although fundamental considerations suggest that As loss may lead to enhanced plastic deformation at the crystal periphery, it is not presently possible to quantify this phenomenon.

The third entry in the above list is related to the mobility of dislocations in GaAs. The creep model used in the present study deals, naturally, with multiplication of mobile dislocations. However, not all dislocations present in the crystal are mobile, for to expand a nucleated loop, its radius has to be larger than a critical value. Alexander gives a value of 1 μm for this critical dimension in Si, ref. [12]. It may be assumed that a similar value is also applicable for GaAs. Thus, it is possible that an appreciably larger number of dislocations close to the crystal periphery, produced perhaps by the deterioration of solid-phase stoichiometry, is immobile. The density of these dislocations would not, then, be captured by the creep model.

Stress-induced deformation and cracking of the crystal surface by the differential thermal expansion of the crystal and an adhered encapsulant layer are observed in many instances. It was not, however, observed for W-1 and W-2.

We believe that of the three possible causes identified for the disagreement between the measured and calculated dislocation densities towards the crystal periphery, the first three are equally likely to be dominant, and the last one least likely to be operative.

The present results appear to establish clearly that dislocation densities as low as 3×10^3 cm^{-2} can be related to plastic deformation of the crystal. This implies that reduction of dislocation density in GaAs crystals to, say, 10^1 - 10^2 cm^{-2} values requires lowering of thermal gradients in the crystal to values substantially lower than the ones yielding thermoelastic stresses equal to one CRSS. This may not be possible in current growth configurations. For example, our model-based strategy for control of stresses during LEC growth of GaAs is limited by the predictive accuracy of the model. To illustrate the required degree of model accuracy, consider the following hypothetical situation. Let us assume that the crystal associated with W-3 was grown such that it did not experience excessive stresses during crystal-melt separation. This would yield a calculated dislocation density of 2.7×10^3 cm^{-2} at the centerline. To reduce the dislocation density by a factor of 10, the thermoelastic stresses at all stages of growth have to be decreased to approximately $0.1 \times$CRSS. This corresponds to controlling the temperature change from the center of the crystal to its periphery at less than 0.3-0.5°C. This is more than the present accuracy level of our model. Reduction of stresses to similar levels in crystals grown by the Vertical

Gradient Freeze (VGF) and its derivatives also appear to be difficult. It has been shown in ref. [13] that the maximum stresses in crystals grown by this technique reflect the morphology of the solid-liquid interface. Growth rates of the order of 0.1-0.2 cm/hr, and furnace gradients of the order of 5-10 °C/cm result in resolved shear stresses marginally lower than the CRSS of the crystal. In light of the present findings, the observed dislocation densities of the order of low-10^3 cm^{-2} in VGF-grown crystals appear to confirm results of ref. [13]. Thus, reduction of stresses during VGF growth to, say, $0.1 \times$CRSS requires significant lowering of both growth rate and axial gradients in the crystal. Achievement of single-crystal growth under these conditions may not be possible.

There are two other alternatives to reduction of temperature gradients in the crystal. First, reduction of the mobility of the dislocations. Second, reduction of the number of nucleated and grown-in dislocations which serve as multiplication sites under applied stresses. The former appears to have been achieved by iso-electronic (e.g., In) doping. However, introduction of impurities in the matrix as a means for retardation of dislocation motion has significant deleterious effects on the behavior of substrates during device-processing. Thus, at present this approach is nearly abandoned. Regarding the second approach, the AH creep model indicates that the dislocation multiplication rate in GaAs is very fast. Therefore, even if a limited number of *mobile* dislocations are present in the crystal, rapid and extensive dislocation multiplication, consistent with the prevailing strain field, will occur. The present model suggests that if dislocation multiplication in the crystal is to be eliminated, nucleation of mobile dislocation should be completely inhibited.

This study appears to well establish the mechanism of dislocation multiplication, at least in the core region, in GaAs crystals. Reduction of the dislocation density in melt-grown GaAs crystals to less than the currently achievable values appears to require further advances in two areas. First, a better understanding of the mechanism of nucleation and incorporation of growth-related (at solid-liquid interface) dislocation is necessary. Second, controllability of the growth processes to reduce the thermal strains in the growing solid needs to be enhanced. There is, definitely, an upper limit to the degree of control that can be reproducibly achieved during melt-growth processes. Fundamental considerations suggest, however, that improvements in this area are still possible. For example, the growth process of ref. [2] should provide for growth of crystals experiencing stresses lower by a factor 2-3 than the ones calculated to be present in W-3.

Table 1. Material Properties for the Creep Model in SI Units

Property	GaAs
m	1.7
$Q(eV)$	1.5
b (m)	4.0×10^{-10}
B_o	1.8×10^{-8}
K (m/N)	–
G (N/m^2)	4×10^{10}
$CRSS(T_m)$ (N/m^2)	0.5×10^{6}
α (K^{-1})	1.0×10^{-5}

References

1. S. Motakef, J. Crystal Growth 108 (1991) 33.
2. K. W. Kelly, K. Koai and S. Motakef, J. Crystal Growth (1991) in review
3. H. Alexander and P. Haasen, Solid State Phys., 22 (1968) 27.
4. K. W. Kelly, Doctoral Dissertation, Mechanical Eng. Dept., M.I.T. (1991).
5. K. Koai, Doctoral Dissertation, Mechanical Eng. Dept., M.I.T. (1990).
6. J. Volkl and G. Muller, J. Crystal Growth, 97 (1989) 136.
7. S. Motakef, J. Crystal Growth (1990) in review
8. P. Maroudas and R. A. Brown, J. Crystal Growth (1990) in press.
9. A. M. Cazin-Bourguignon and S. Motakef, J. Crystal Growth (1989) 390.
10. K. W. Kelly, K. Koai, and S. Motakef, J. Crystal Growth (1991) in review.
11. G. Elliot, et al., J. Crystal Growth, 70 (1984) 189.
12. H. Alexander, in Radiation Effects and Crystal Defects, (1990) in press.
13. S. Motakef, J. Crystal Growth, 98 (1989) 711.

Figure Captions

Fig. 1 Trace of the crystal geometry grown by the LEC technique (dashed line) and the model shape (solid line) used in the calculation.

Fig. 2 Trace of the crystal geometry grown by the method of ref. [2] (dashed line) and the model geometry (solid line) used in the calculation.

Fig. 3 The history of τ_{vm} and dislocation density in W–1 at four radial locations. The measured EPD's are also shown.

Fig. 4 The history of τ_{vm} and dislocation density in W–2 at four radial locations. The measured EPD's are also shown.

Fig. 5 The history of τ_{vm} and dislocation density in W–3 at four radial locations. The measured EPD's are also shown.

Fig. 6 Comparison of calculated dislocation density with the measured EPD at four radial positions for W–1, W–2, and W–3. The points lying outside the $\pm 100\%$ band are all close to the outer periphery of the wafers.

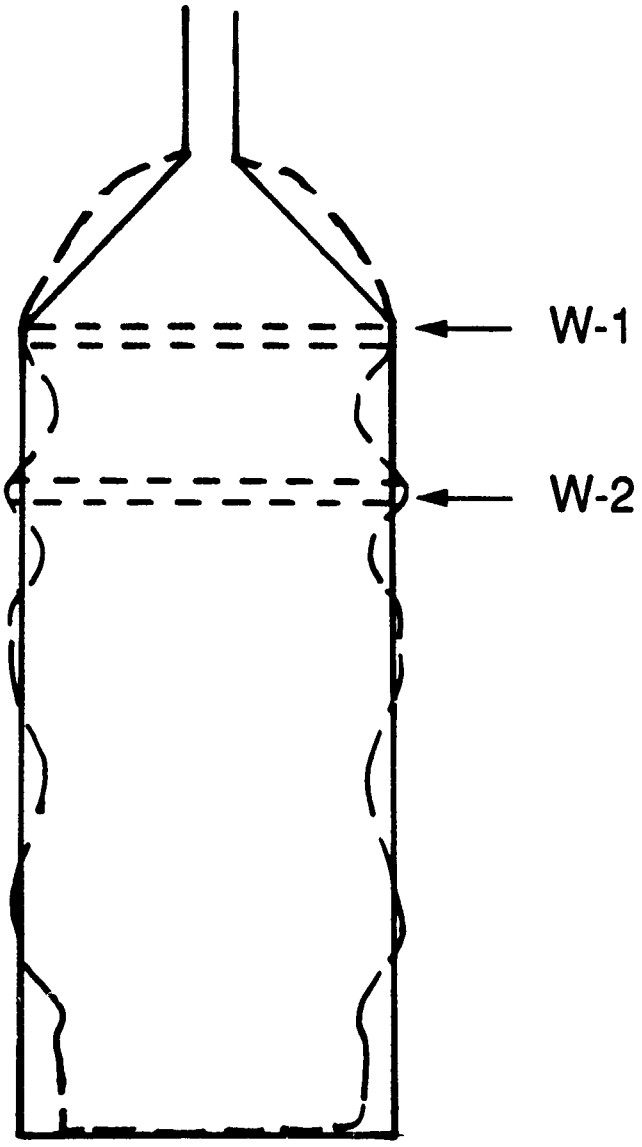

Fig. 1

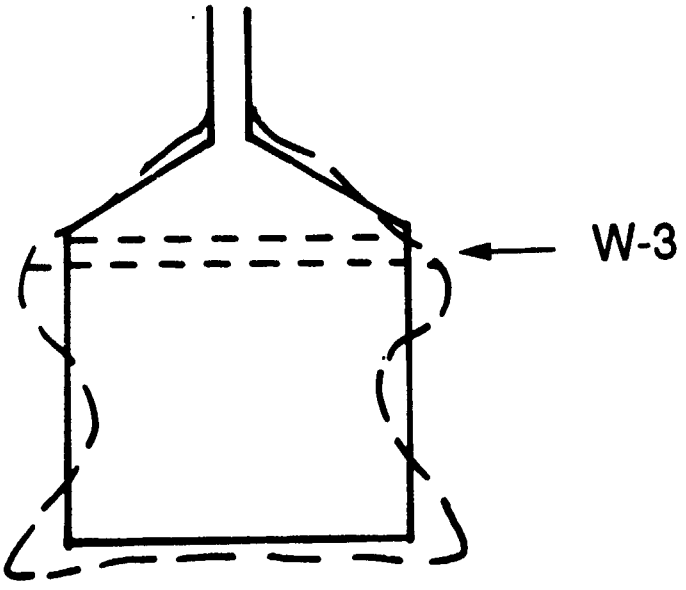
W-3

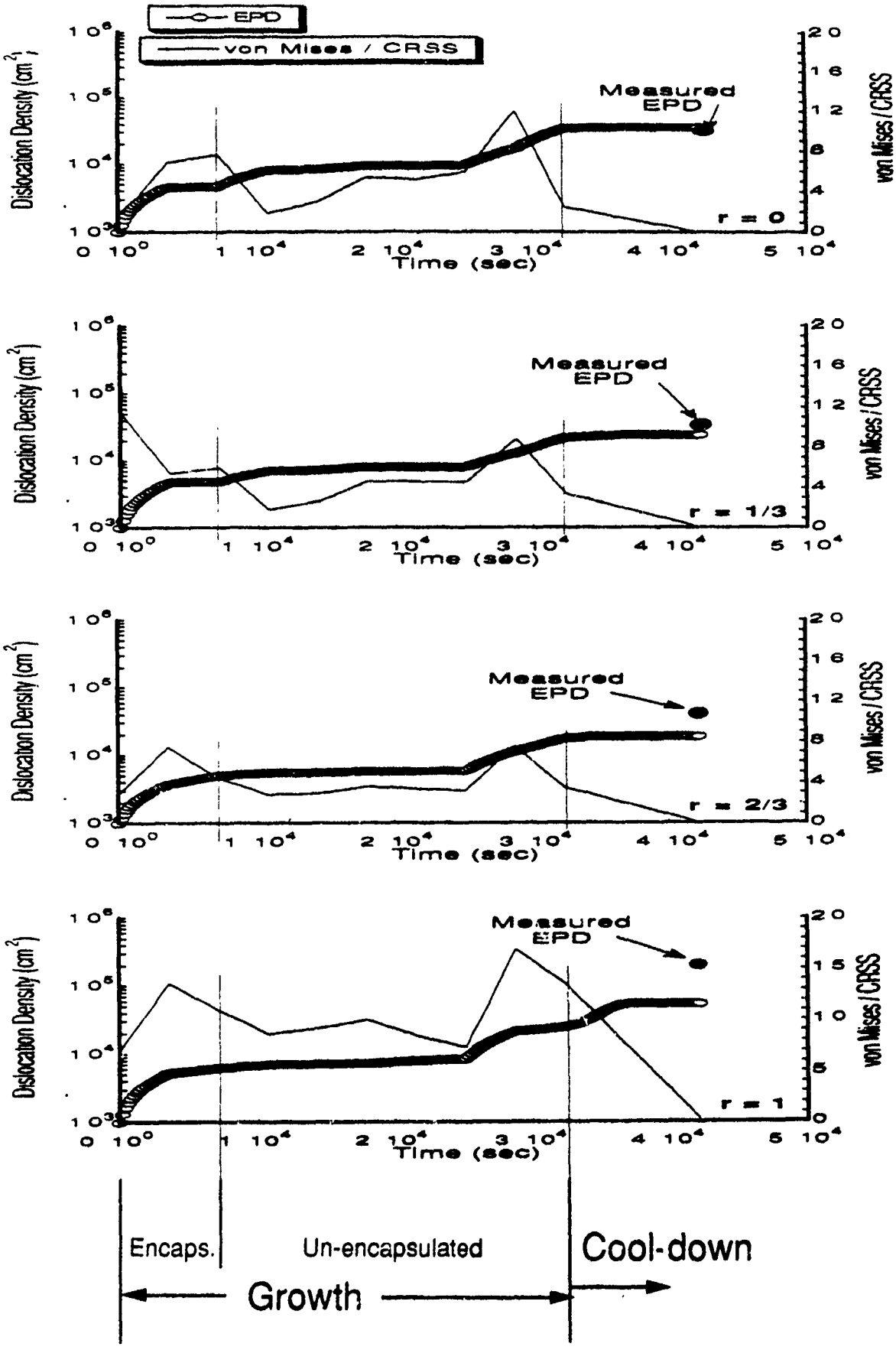
EPD
von Mises / CRSS
Measured EPD
r = 0
r = 1/3
r = 2/3
r = 1
Dislocation Density (cm^{-2})
von Mises / CRSS
Time (sec)
Encaps.
Un-encapsulated
Cool-down
Growth

Fig. 3

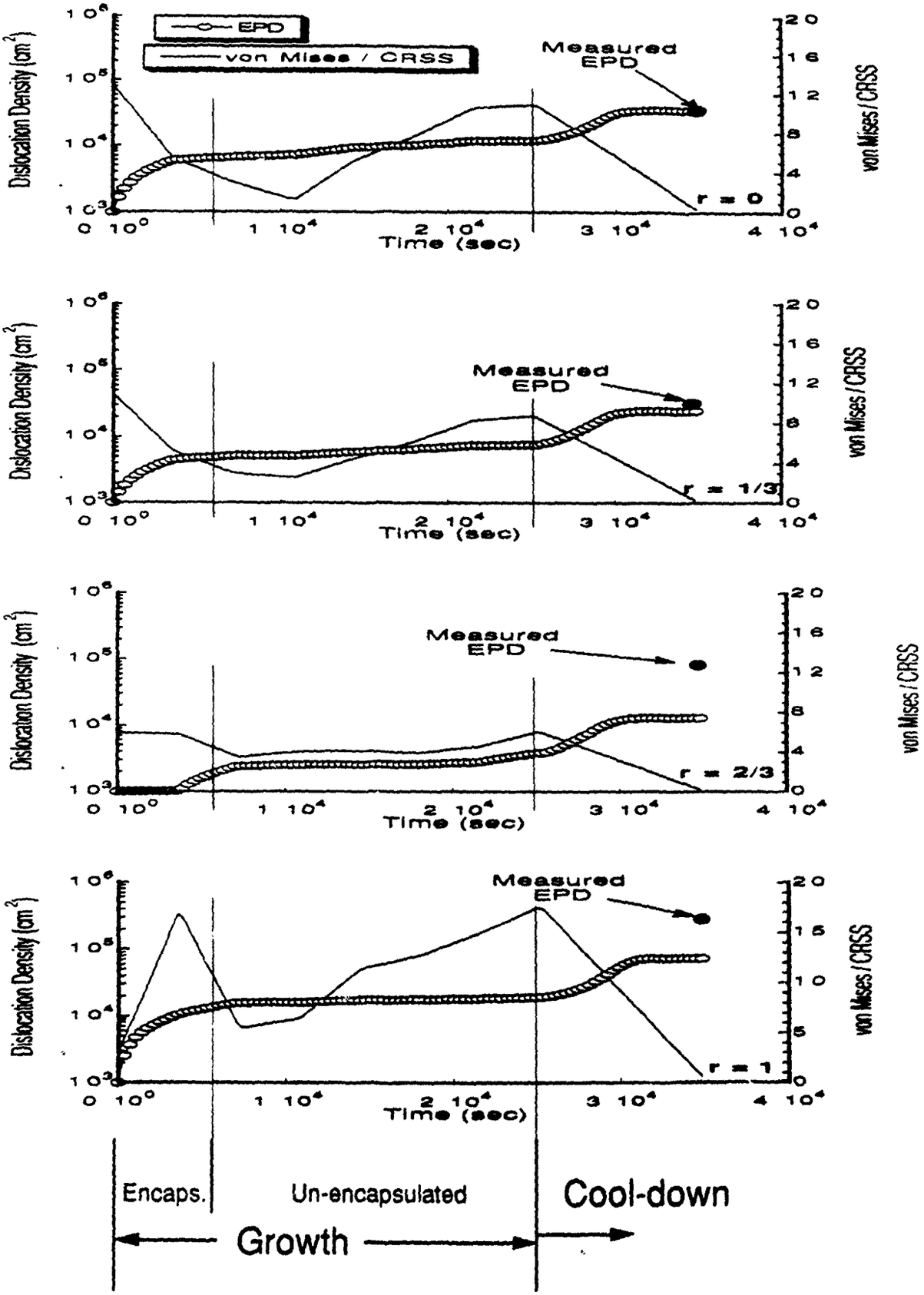
EPD
von Mises / CRSS
Measured EPD
r = 0
r = 1/3
r = 2/3
r = 1
Dislocation Density (cm^{-2})
von Mises / CRSS
Time (sec)
Encaps.
Un-encapsulated
Cool-down
Growth

Fig. 4

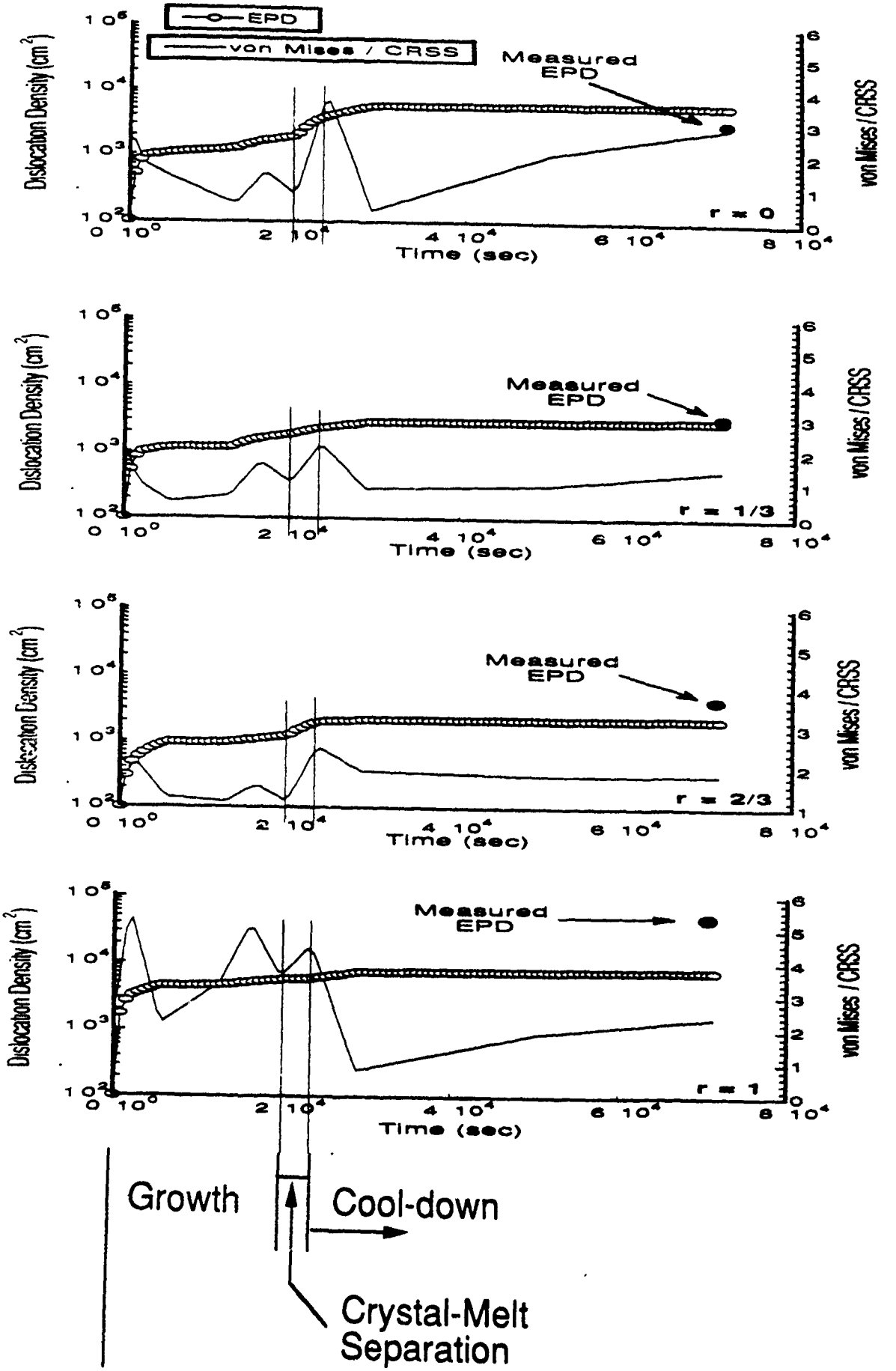
EPD
von Mises / CRSS
Measured EPD
Dislocation Density (cm^{-2})
von Mises / CRSS
Time (sec)
r = 0
r = 1/3
r = 2/3
r = 1
Growth
Cool-down
Crystal-Melt Separation

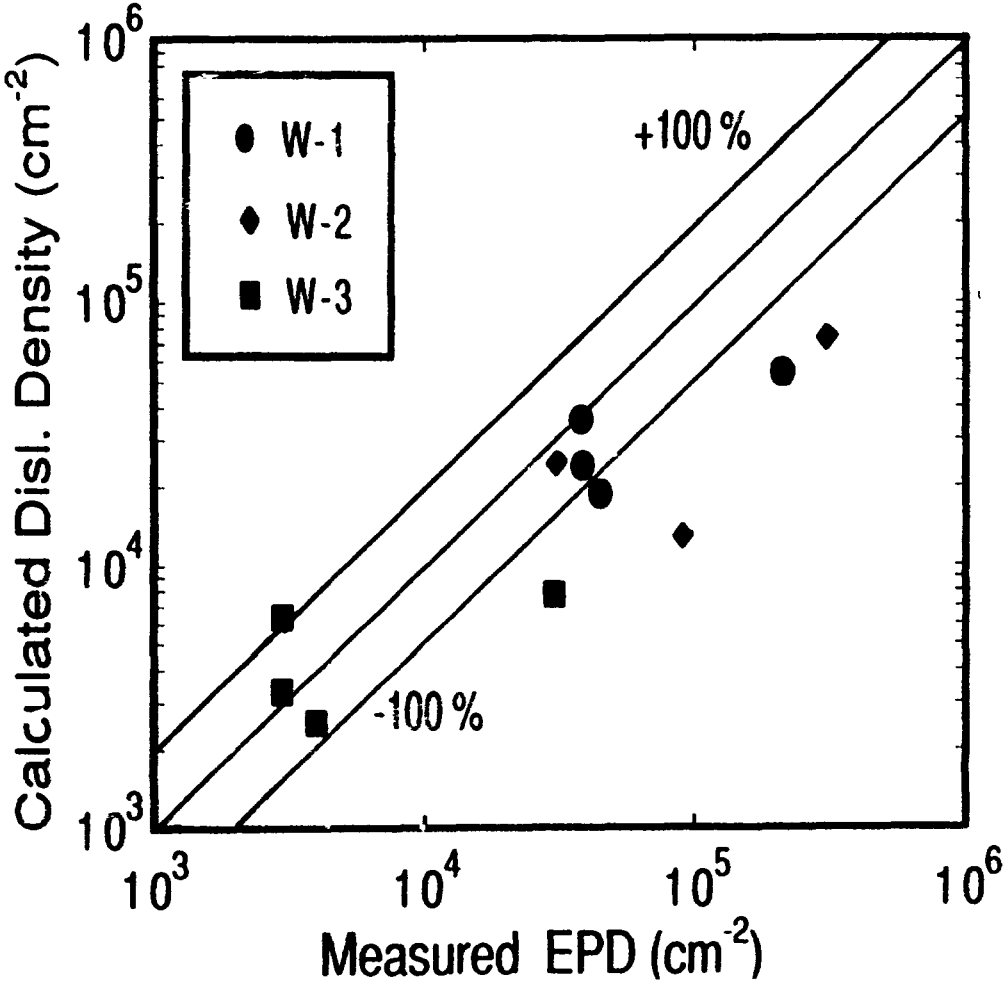
W-1
W-2
W-3
+100 %
-100 %
Calculated Disl. Density (cm^{-2})
Measured EPD (cm^{-2})
10^3
10^4
10^5
10^6

Fig. 6